Evaluating Soil Loss from Ephemeral Gullies with Photogrammetry

by

Chinthaka Bandara Weerasekara

B.Sc., University of Peradeniya, Sri Lanka 2010

A THESIS

submitted in partial fulfillment of the requirements for the degree

MASTER OF SCIENCE

Department of Biological and Agricultural Engineering
College of Engineering

KANSAS STATE UNIVERSITY
Manhattan, Kansas

2019

Approved by:

Major Professor
Dr. Aleksey Y. Sheshukov

Copyright

© Chinthaka Weerasekara 2019.

Abstract

Sedimentation is a significant threat to water reservoirs and streams in Kansas, the Central Great Plains in the United States, and worldwide. Soil erosion in agricultural fields is one of the primary environmental concerns and a major contributor to sedimentation. Ephemeral gullies (EG) are localized areas of soil erosion that form from concentrated water flow in upland areas. Soil erosion from EGs in agricultural fields contributes a substantial fraction of annual upland sediment and does so disproportionally (relative to other sources) during higher-flow events. Limited evidence exists of documented EG development during a crop growing season, thus there is a need for field experiments with frequent EG surveying. Close-range photogrammetry is a method of creating digital elevation maps from a set of photographs that can be used for EG erosion assessment. Main objectives of this study were to develop an EG monitoring method based on photogrammetry technique, apply it to ephemeral channels in a no-till field in northeast Kansas, and evaluate the factors related to EG development. A close-range photogrammetry method was first designed and conducted in the lab experiment in order to evaluate the produced model accuracy, ground control point density, and their spatial distribution. For most accurate results, it was determined that optimal ground control point density was 3 to 4 points per 1 m^2, 60% or more of photograph image overlap, and a camera tilting angle between 0^0 and 30^0. Twelve repetitive photogrammetry surveys were conducted for field surveying of three EGs over a two-year period from 2016 to 2018. The produced 3-D digital surface models were analyzed to identify specific EG topographic features, evaluate the changes in EG surface area, width, depth, rates of growth, and seasonal soil loss estimates. Unique patterns of soil erosion during crop growing season and sediment accumulation within the gullies were observed for all EGs.

Table of Contents

List of Figures

List of Tables

Acknowledgments

I would like to express my sincere gratitude and appreciation to my major professor, Dr. Aleksey Sheshukov. His mentorship, encouragement and valuable suggestions greatly helped me to advance my research training. I would also like to thank my committee members Dr. Stacy Hutchinson, Dr. Arnaud Temme for their willingness to serve in my committee and for their time, interest, and helpful comments on my research work.

I would like to thank Will Boyer, Jonathan Zeller, Kari Bigham and Vladimir Karimov for their help and support for the field experiments related to this project.

I would also like to thank my parents, my wife and my friends for their support and belief in my success.

Dedication

To my beloved late mother:

for all the sacrifices she made to let me achieve my goals.

1 Introduction

World population has been doubled in 40 years from 1953 to 1999 and is projected to increase by another 50% in the next 40 years (UN, 2017). With the population growth, global food and water demand has been intensified and ensuring food security is the most prominent challenge scientists facing today (Sims et al., 1997; Pimentel, 2006). Humans obtain more than 99.7% of their calorie requirement from the land, and each year about 10 million ha of cropland are lost due to soil erosion that reduced cropland available for food production (Pimentel, 2006). Topsoil is the most valuable part of the soil for agricultural production, and it is the most vulnerable to soil erosion (Keesstra et al., 2016).

Soil erosion due to surface runoff causes soil degradation and reservoir sedimentation. Reservoir sedimentation is a significant threat to water reservoirs and streams specifically in Kansas and the Central Great Plains in the United States. The Kansas State Research and Extension (KWO, 2008) reported that all federal reservoirs in Kansas lost 33% of the original capacity due to sediment deposition.

Water erosion is a main type of soil erosion and is defined as the detachment and transport of soil from the land by runoff. Water erosion occurs when the combined power of rainfall energy and overland flow exceeds the resistance of soil to detachment (Bernard et al., 2010). Water erosion can be categorized into raindrop erosion, sheet erosion, rill erosion, gully erosion and streambank erosion (National Research Council, 1986). Raindrop erosion is the soil detachment due to the impact of raindrop and soil surface. Amount of raindrop erosion is highly correlated with the rainfall momentum, rain direction and slope of the land (Valentin et al., 2005). Sheet erosion is a uniform removal of soil in thin layers from a sloping land due to overland flow. Rills are small channels that can be removed by tillage operations. Rill erosion is the detachment and transport of soil by the concentrated flow of water. Gullies are channels larger than rills caused by concentrated flows. According to obliteration effort, gullies can be categorized into two categories; classical gullies and ephemeral gullies (EG). EGs can be obliterated by tillage operations while classical gullies require additional effort (Bernard et al., 2010). However, normal tillage operation obliterates the EGs, and they will appear in the same locations in next year (Davis et al., 1983). The streambank erosion is caused by the concentrated water flow of streams. Streambank erosion leads to stream meandering and recanalization (National Research Council, 1986).

EGs are localized areas of soil erosion that form from concentrated water flow in upland areas (Soil Science Society of America, 2008). EGs erode topsoil, but tillage fills them in, often with less-productive subsoil. If not corrected, EGs may grow into permanent gullies. Erosion from EGs in agricultural fields contributes a substantial fraction of annual upland sediment and does so disproportionally (relative to other sources) during higher-flow events. However, the contribution of EG erosion can range from 30% to as much as 100% of the total soil loss (Daggupati, Sheshukov, and Douglas-Mankin 2014; National research council 1986), thus, exceeding the contribution of sheet and rill erosion. The contribution of EG erosion varies geographically (Valentin et al., 2005). In general, precipitation, topography, soil and land use/land management practices affect the formation and development of EGs (Valentin et al., 2005).

Length, width, and depth of the EGs are small in size. The irregular shape of gullies makes the data collection difficult (Schmid et al., 2004). The features of the gullies are easily reshaped within a small period by farming operations and weather conditions (Gao, 2013). The data collection method should have adequate spatial and temporal resolution to capture the dynamic changes of EGs (Gessesse et al., 2010).

EG erosion has been quantified using pin measurements, runoff-monitoring samples, sediment surrogates, total station survey, airborne, terrestrial light detection, ranging sensors (LiDAR) and photogrammetry (Thomas and Welch, 1988; Gómez-Gutiérrez et al., 2014; Marzolff and Poesen, 2009). However, it is essential to use an accurate and efficient survey method which has a minimal impact on the EG and the field. Several studies (Brasington and Smart, 2003; Gessesse et al., 2010; Castillo et al., 2012) proved that photogrammetry technique could be used to monitor EGs accurately and efficiently. Photogrammetry technique provides adequate spatial and temporal resolution to monitor small changes within a short period.

Soil conservation practices substantially reduce sheet and rill erosion, but the impact on EG erosion is unclear. Studies have shown that EG erosion is a major contributor of sediment in streams and requires serious attention (Daggupati and Sheshukov, 2013; National research council, 1986). However, mechanisms related to EG formation, location, geomorphological properties related to storm characteristics, and the amount of soil loss are not understood well enough, either to quantify the importance of EGs relative to other sediment sources in a watershed or to guide EG-effective best management practices (BMP). More field measurements, lab experiments, and computer modeling studies are needed to gain a better insight into the physical processes that are important for the development of EG erosion.

1.1 Goals and Objectives

Main objectives of this study are: (1) to assess EG-driven soil erosion by monitoring the elevation within EGs on a no-till field near Manhattan, Kansas, U.S.A and (2) to evaluate factors that affect soil loss along concentrated flow paths of each gully. Simultaneously, the following objectives are achieved.

I. Evaluating the accuracy of the photogrammetry method to use for field measurements of EGs.
II. Monitoring and assessing the development of EGs in a cropland field in North-East Kansas using sub-annual photogrammetry surveys.

2 Literature Review

2.1 Ephemeral gully erosion

In the early 1980s, soil conservationists noted the specific type of channels which are important sources of erosional sediment within the field and named them as ephemeral gullies (Foster, 1982a). EGs are defined as small channels eroded by concentrated flow that can be easily filled by normal tillage, only to reform again in the same location by additional runoff events (Soil Science Society of America, 2008). Channels larger than the rills and smaller than the classical gullies are considered as EGs. Figure 2-1 shows the main components of an EG. Typically, EGs have an average cross-sectional area of around 0.1 m^2 and a depth of 0.2 m (Bernard et al., 2010). EGs form at the hillslope or lower part of a cultivated field. Table 2-1 shows the characteristics of rill erosion, EG erosion, and classical gully erosion (National Research Council, 1986).

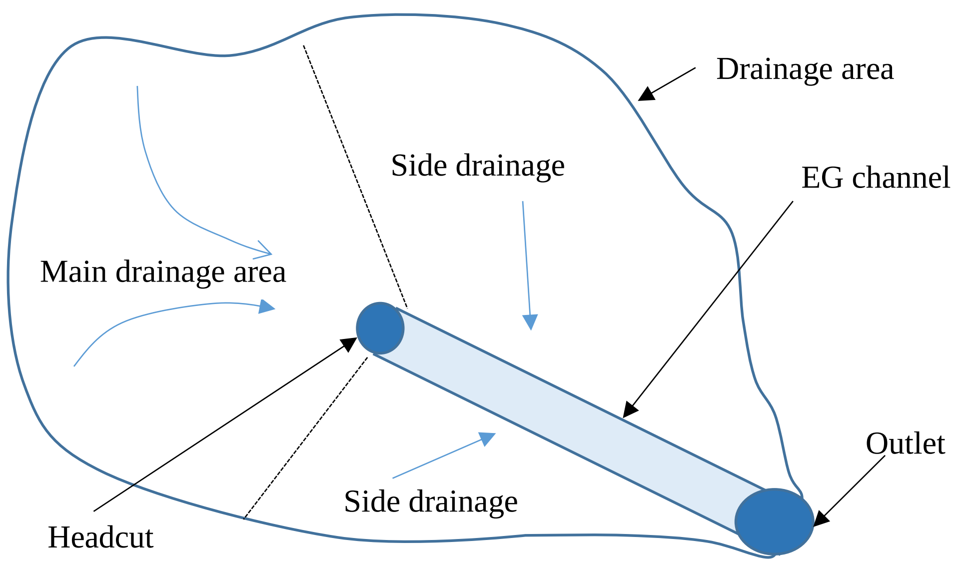

Figure 2-1: The main components of an ephemeral gully channel

Table 2-1: Comparison of rill erosion, EG erosion and classical gully erosion (National Research Council, 1986)

Rill erosion	**EG erosion**	**Classical gully erosion**
Rills are normally erased by tillage, and they do not reoccur in the same location.	EGs are short-term features, normally covered by tillage and reoccur in the same location.	Gullies are not covered by normal tillage operations.
Rills are usually smaller than EGs.	EGs are larger than rills but smaller than classical gullies.	Gullies are larger than EGs.
Cross sections of the rills tend to be narrower compared to the depth.	Cross sections of EGs tend to be wider relative to the depth; side walls are not frequently well defined; head cuts are usually invisible and are not prominent due to tillage.	Cross sections of Gullies tend to be narrower relative to the depth, with steep side walls and prominent head cut.
Rills occur on smooth die slopes above drainage paths.	EGs appear along shallow drainage ways upstream from incised channels.	Gullies usually occur in well-defined drainage ways.
Rill flow patterns develop due to small disconnected parallel channels merging to an EG or terrace or points of deposition. Rills are generally spaced and sized.	EGs usually form a dendritic flow pattern along water causes, beginning from areas of overland flow including rills and areas of convergence. The flow patterns may be influenced by tillage, crop rows, and terraces.	Gullies tend to form a dendritic flow pattern along natural water pathways and a non-dendritic flow pattern along roads, ditches, terraces, and channel diversions.

Table 2-2: Assessment of ephemeral gully erosion rates in selected areas in the United States (NRCS, 1997).

Location	Estimated Annual Sheet and Rill Erosion (kg m^{-2} y^{-1})	Measured Ephemeral Gully Erosion (kg m^{-2} y^{-1})	Ephemeral Gully Erosion as a Percentage of Sheet and Rill Erosion (%)
Alabama	0.573	0.342	60
Delaware	0.038	0.093	245
Illinois	0.261	0.191	73
Iowa	0.353	0.110	31
Kansas	0.807	0.294	36
Louisiana	0.654	0.222	34
Maine	0.412	0.189	46
Maryland	0.195	0.147	75
Michigan	0.172	0.045	26
Mississippi	0.646	0.275	43
New Jersey	0.246	0.191	78
New York	0.873	0.185	21
North Dakota	0.277	0.130	47
Pennsylvania	0.093	0.065	70
Rhode Island	0.331	0.136	41
Vermont	0.165	0.224	136
Virginia	0.477	0.470	98
Washington	0.025	0.069	274
Wisconsin	0.289	0.154	53

Several studies were conducted all over the world to quantify the EG erosion and assess the overall impact of EGs. The contribution of gully erosion to the total soil loss from water erosion ranges from 10% to 94% worldwide (Valentin et al., 2005). The contribution of EG erosion to total soil loss varies from 30% to 100% in actively eroding areas (Daggupati and Sheshukov, 2013). In New York state in the United States, EG erosion has a 17% contribution to total soil loss and 73% in Washington State (Bennett et al., 2000b). In the Loess Plateau of China, EG erosion ranges from 41% to 91% of soil loss (Zheng and Gao, 2000). Table 2-1 shows the quantity of soil loss attributed by both sheet and EG erosion in the United States

Soil properties, rainfall characteristics, topographic features, land cover, and land management practices affect the formation and EG development (Gao, 2013). Soil properties also play a major role in the water erosion process. To detach soil particles from the soil, shearing forces of water should exceed the critical shear stress value of the soil. If the critical shear stress value of soil is greater than the shear stress value of water, the soil stays attached, and no soil detachment occurs. Critical shear stress values are related to the variety of soil properties including the topsoil texture, density and the moisture content (Govers et al., 1990). Soil detachment rates can be calculated by the excess shear stress equation (2-1):

$$D_{rc} = K_r(\tau - \tau_c)^{\beta} \tag{2-1}$$

where D_{rc} is the erosion rate in (kg/s/m^2), K_r is the soil erodibility (s/m), τ is the shear stress acting at the point along the rill boundary (Pa), τ_c is the soils critical shear stress (Pa) and β is a constant which is often considered as 1.

EG erosion process is a combination of soil detachment from the channel surface and transportation of those sediments to downstream. Therefore, the EG process is controlled by either the critical shear stress or the sediment transport capacity. The excess shear stress equation (2-1) determines the maximum possible soil detachment rate, but if the sediment load is greater than the sediment transport capacity, runoff cannot carry more sediments and will deposit the excess sediments. The governing equation of EG erosion is given by,

$$D_f = D_{rc}\left(1 - \frac{G}{T_c}\right) \tag{2-2}$$

where D_f is the detachment rate along the channel boundary [mass/(area • time)], D_{rc} is the detachment capacity of the flow defined in equation (1) [mass (area • time)], G is the sediment load in the flow (mass/time) and T_c is the transport capacity of the flow (mass/time) (Foster and Meyer, 1972).

Most EGs have concave channel profiles. The gradient of the channel decreases along with the length. Although the transport capacity (maximum load of sediment that a given flow rate can carry) tends to increase as the discharge increases along the gully, the decrease in gradient tends to lower the transport capacity (National Research Council, 1986). However, the sediment load increases along the gully and at some point, sediment capacity exceeds the transport capacity and deposition will occur. Backwater from a restricted channel outlet can also reduce the transport capacity which results in a deposition. When deposition occurs, sediment yield from the channel is mainly controlled by the transport capacity of the flow close to the outlet of the channel (Foster, 1982). Figure 2-2 shows the variation of the sediment load and transport capacity of a typical EG having a concave profile (National Research Council, 1986).

Grass, crop residue, and clods elements significantly reduce flow shear stress acting on the soil and decrease the erosion (Foster, 1982). The no-till management practice makes unfavorable conditions to EG erosion. It has a minimum disturbance to the soil surface and does not reduce the critical shear stress value of the soil. Also, this management practice keeps crop residue on the soil surface which helps to minimize the impacting power of water and increase the infiltration capacity. However, conventional tillage practice works vice versa. It disrupts the soil structure and weakens the soil. Also, conventional tillage supports to create paw-pan which decrease the infiltration capacity of the soil.

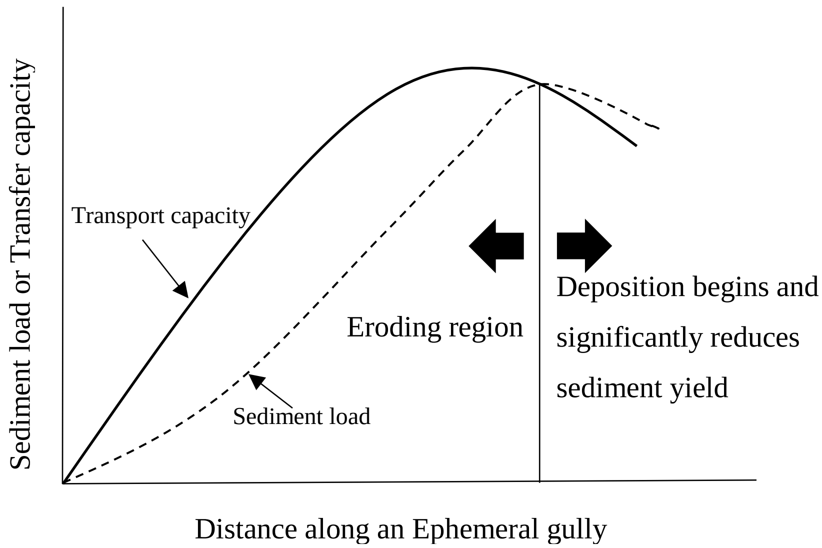

Figure 2-2: Variation of the sediment load and transport capacity along an ephemeral gully

2.2 Field measurements of gully erosion

EG erosion is a major sediment source, and many studies have been conducted to understand EG formation, location and model development. Measuring the eroded amount is very important for the soil erosion assessment. Techniques ranging from simple methods of approximating the gully cross-sectional to complex approaches such as photogrammetry techniques can be used to assess the EG erosion in the field. Stereoscopic photogrammetry, high accuracy GPS, and laser scanners are used to measure EGs. However, the irregular shape of the gully causes difficulties for the measuring process, and these methods are costly and time-consuming.

- In 1982, Zheng introduced a method that measures the eroded volume by refilling eroded gully with soil. The method generated high measurement errors because of the mismatching refilled soil density with actual soil density (Zheng, 1989). Later this method is modified and applied by using Styrofoam to refill the gully instead of soil (Dong et al., 2015). The modified method was able to estimate the total soil loss within the gully, and the volumes were tally with the values obtained from the sampling method. However, in practice, it is difficult to use this method to evaluate soil losses.
- Tape and ruler are the straightforward instruments used on the volume measurements of the EGs. This method gives a rough estimation of cross section width and depth of the channel. Ludwig, Boiffin, et al. (1995) used this method to analyze the variability between rills in different catchments. Smith (1993) also used this method to quantify soil losses in Mississippi. Instead of directly using a ruler to measure EGs, he used Gulliometer to copy the gully profile to a paper and later extracted gully information from the drawing. This method required time-intensive field work.
- Microtopographic profiler is another conventional technique widely used to evaluate gully erosion. Karimov and Sheshukov (2017), Casalí et al. (2006), Bennett et al. (2000a) used profiler meter to monitor the EGs. It is essential to hold pinframe in the same vertical and horizontal position in every survey to make an accurate time series of gully development. Microtopographic profiler can accurately record cross-sectional information at a lower cost. However, the extent of this method is limited and requires some labor and intensive field work to get accurate data.
- Standard surveying technology such as a total station can provide high temporal resolution through multiple revisit cycles, but the data are collected discretely. It requires time-intensive fieldwork by a couple of people onsite, and large uncertainties are associated with data

interpolation procedures to convert at-a-point information (discrete data) into continuous data for topographic and hydrologic analysis (Wells et al., 2016).

- Multi-temporal aerial photographs and multi-temporal digital elevation models are successfully used to quantify gully erosion. This technique is suitable for large-scale, long-term projects (Castillo et al. 2012; Campo-Bescos et al. 2013). Lack of temporal resolution and the spatial resolution limit the application of this technique to small scalar short-term projects.
- Perry and Bookhagen (2010) used ground-based light detection and ranging (LiDAR) and airborne based LiDAR to measure gully erosion, and they compared both results with total station surveys. The results showed that both airborne and ground-based LiDAR often overestimate the surface elevation. The overestimation of the elevations underestimates the erosion volumes and cross-sectional areas. However, they suggested these errors can be minimized by using higher resolution airborne data and manual optimization using the field data. However, both systems can discriminate and measure gully features that are effectively invisible at existing coaster resolution DEM data sets.
- Vinci (2015) used Terrestrial laser scanner (TLS) to measure the gully erosion, and he compared laser scanner results with the surveys done with the Profilometer and metric ruler. The comparison showed that both have a good match in terms of the shape and the dimension size.
- With the improvement of UAV technology, digital cameras, and photogrammetric software packages, 3-D photo construction methods (photogrammetry) became dominant survey methods for the gully assessment. Since 1984 photogrammetry techniques have been used to derive quantitative measurements of soil erosion. Gillan et al. (2017) compared erosion measurements obtained from photogrammetry technique with the traditional ground-based erosion measurements. The study found that both measurement techniques strongly agree with

each other, and root mean square errors (RMSE) between the two methods were 2.9 cm and 3.2 cm for two different surveys. Pineux et al. (2017) applied photogrammetry technique to produce DEM time series over two years to quantify diffuse erosion in an agricultural watershed and identified erosion/deposition pattern, the tendency along the slope from erosion to deposition. Spomer and Mahurin (1984) used the stereoscopy based photogrammetry technique to quantify rill and sheet erosion. Nachtergaele and Poesen (1999) also used the stereoscopy based photogrammetry technique to assess the soil loss in EGs. The accuracy of the method was 0.05ft and was able to calculate annual soil loss in the watershed. Daba, Rieger, and Strauss (2003) assessed gully dynamics and volume changes over 40 years using photogrammetry. The photogrammetry models were built using historical aerial photographs taken in 1966 and 1996. Marzolff and Poesen (2009) studied how non-metric digital photogrammetry can be used to monitor the gullies and found that non-metric digital photogrammetry can achieve the accuracy up to 0.1 cm. Smith, Chandler, and Rose (2009) analyzed factors influencing riverbank changes on a seasonal scale using the photogrammetry model. Wells et al. (2016) introduced a low-cost, high-resolution close-range photogrammetry method to monitor the EG erosion. Brasington and Smart (2003) used close-range digital photogrammetry to evaluate sedimentation pattern and sediment rate over a simulated landscape. The comparison of sediment budget over the simulation and the total soil loss calculated using the photogrammetry method had a small 6.2% difference. Gessesse et al. (2010) applied close-range photogrammetry to assess soil loss/gain happened in irregular soil surfaces and obtained 2.8-5.3mm horizontal accuracy. Campo-Bescos et al. (2013) used photogrammetry model to understand gully headcut growth processes and calibrated gully headcut retreat models. Castillo et al. (2012) and Wells et al. (2016) evaluated accuracy and advantages and disadvantages of the photogrammetry method and concluded, that close-range photogrammetry gives a high spatial resolution dataset under minimal environmental impact to field and farming operations and with extremely less field labor. This method also satisfies temporal resolution which is required to identify frequent changes of EGs.

Practicability, accuracy, and cost are the main concerns in selecting a gully monitoring method. Compared to the other methods described above close-range photogrammetry is a simple, reliable and robust method to track evolutionary changes over a long period. Castillo et al. (2012) compared the accuracy of LiDAR, photogrammetry, laser profile meter, total station, and tape-pole. They compared measured value with the value given by the mathematical model and calculated a relative error. For each method a calculated relative cross-sectional error is presented in Table 2-3, and relative volume error is shown in Table 2-4.

Table 2-3: Relative cross-sectional error in percentages (Castillo et al., 2012)

	Photo reconstruction	Profile meter	Total station	Pole
Profile1	3.6	-14.9	2.7	-7.8
Profile2	2	-5.9	-1.1	0.7
Profile3	-0.1	-9	2.2	-23.5

Table 2-4: Relative volume errors (Castillo et al., 2012)

Method	***V***	***EV***
	m^3	**%**
LiDAR	13.29	–
Photo-reconstruction	12.88	–3.1
Laser profilometer	11.52	–13.3
Total station	14.14	6.4
Pole simplified	11.25	–15.3

Assessing gullies using ground-based laser equipment and software usually costs more than \$100,000 while with photogrammetry it may cost less than \$9,000 for the initial setup (Wells et al., 2016). In terms of the labor and time, photogrammetry requires a similar amount of time and labor compared to the ground-based laser system which has minimal requirements compared to any other methods described earlier. The photogrammetric technique is a robust and straightforward technique to track evolutionary changes in concentrated flow paths within agricultural fields, drainage ditches, and roadways (Wells et al., 2016).

2.3 Simulation of EG Erosion

WEPP model

Water Erosion Prediction Project (WEPP) model is a physically based spatially distributed watershed model. The model is based on stochastic weather generation, infiltration theory, hydrology, soil physics, plant science, hydraulics, and erosion mechanics. The WEPP erosion model computes soil loss along the slope and sediment yield at the end of a hillslope.

Main components of the WEPP model are weather generation, frozen soils, snow accumulation and melt, irrigation, infiltration, overland flow hydraulics, water balance, plant growth, residue decomposition, soil disturbance by tillage, consolidation, erosion and deposition sediment. Inter-rill and rill erosion processors are used to calculate total sediment yield coming from the watershed. It is assumed that inter-rill sediment delivery rate is proportional to the product of rainfall intensity, and the rill detachment which is controlled by the access shear stress equation (Equation 2-1) and the sediment transport capacity (Equation 2-2).

Overland flow processes are assumed as a mixture of broadsheet flow and channel flow. Broadsheet flow on an idealized surface is assumed for overland flow routing and hydrograph development. Overland flow routing procedures use both analytical solutions of the kinematic wave equations and regression equations derived from the kinematic approximation (Suzanne, 2013). At the end of the routing step, the runoff duration is calculated using the conservation of the mass theory.

Foster and Lane approach

Foster and Lane (Foster and Lane, 1983) developed a physically based channel development model to describe the channel development due to concentrated flow. The Foster and Lane model assumes a steady state flow rate and two distinct stages of channel development. During the initial state, channel bottom erodes at a constant rate until it reaches the non-erodible layer. The width of the channel depends on the flow rate and soil properties.

The rate of potential detachment is based on the excess shear stress equation (Equation 2-1)(Foster and Lane, 1983). Particle detachment occurs if the acting shear stress is greater than the critical shear stress. Thus, the critical shear stress defines the critical condition of the particles on the soil surface when they lose the ability to overcome the acting shear stress of the moving water. Critical shear stress controls both the moment of the start of the erosion and the erosion rate while soil erodibility coefficient K_r corresponds to the rate of the soil detachment. Both parameters, critical shear stress and soil erodibility coefficient are hard to define and they may have the dependence on various parameters such as vegetation, soil moisture, management practices, etc. (National Research Council, 1986). Equilibrium rill geometry for stage one rill development is shown in Figure 2-3(a).

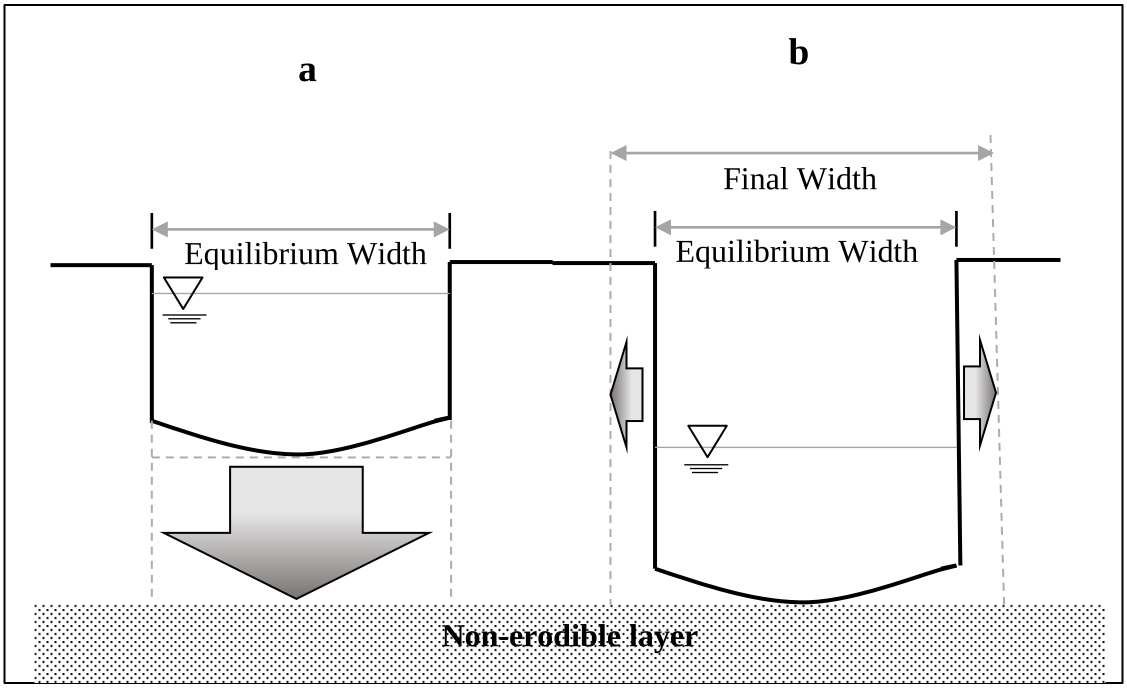

Figure 2-3: Two stages of the rill development process

After the channel bottom reaches the non-erodible layer, the second stage of the channel development starts. In the second stage, channel expands laterally causing sidewall sloughing Figure 2-3(b). This lateral expansion continues at an exponentially decreasing rate until a final width is reached. Due to the parabolic shape of the rill bottom, rill center reaches the non-erodible layer before rill corner reaches the non-erodible layer. The area contained between parabolic and rectangular rill bottom is negligible. However, the actual channel erosion depends on soil critical shear stress as well as the transport capacity of the runoff. Therefore, to find actual detachment, potential detachment is needed to translate using the Equation 2-2.

Modified Foster and Lane Model

Foster and Lane's model assumes a constant flow during the runoff event for determining the shape of the channel cross-section. Modified Foster and Lane model was introduced to use Foster and Lane approach for dynamically changing flow rates (Karimov, 2017). The channel shape re-configuration scheme shows the process of potential computing erosion with the modified approach of Foster and Lane model to allow channel erosion driven by hydrograph with a variable erosion rate. The differences are noticeable in the adjustment of the initial width and depth compared to the previous time step, and the channel reshaping after the current time step if the two-tier channel shape was used. For the case when the equilibrium width is smaller than the current width of the channel from the previous step, a two-tier channel is used for the application of the classical Foster and Lane approach.

In this case, if the channel reaches the non-erodible layer, the depth of the bank is lower for the widening stage until it reaches the width from the previous time stage. The current depth is adjusted when the current width is smaller than the width at the beginning of the current time step. The increase of the equilibrium width occurs on the rising part of the hydrograph. On the declining part, the equilibrium width is lower than the width from the previous time step. In this case, the erosion rate is computed for the equilibrium width, but the final width is adopted from the previous time step. However, the eroded depth is reduced to ensure the same eroded volume. Also, for any time step, it is possible that the channel reaches a non-erodible layer; in any case, both the final depth and the width are considered in computing the eroded volume.

2.4 Photogrammetry for EGs

Overview

Remote sensing technology has been used in a wide range of environmental studies (Luhmann et al., 2006). The remote sensing systems such as unmanned aerial vehicles (UAV), ground-based photogrammetry, terrestrial laser scanning, terrestrial LiDAR, and close-range photogrammetry are major remote sensing methods which are used to evaluate the geomorphological changes (Evans and Lindsay, 2010; Collins, Brown, and Fairley, 2007). Among these methods, photogrammetry is being widely used because of its low cost and abundance of digital cameras and computers (Castillo et al., 2012).

As defined by the American Society for Photogrammetry and Remote Sensing, photogrammetry is an art, science, and technology of obtaining reliable information about physical objects and the environment through processes of recording, measuring and interpreting photographic images and patterns of recorded radiant electromagnetic energy and other phenomena. Photogrammetry can be classified into two categories based on the location of a camera during the image collection: (i) aerial photogrammetry and (ii) terrestrial (or close-range) photogrammetry. In aerial photogrammetry, the camera is mounted in airborne platforms; aircraft or drone, and pointed vertically downward towards the ground. In close-range photogrammetry, the camera is mounted into the ground-based platform like tripod, frame, or handheld.

From 1850 to the present there were four major evolutions in the photogrammetry technique (Duerer, 1977).

- From 1850 to 1900s, plane table photogrammetry was used. This technique was used to record the topography of terrain and create maps using photographs.

- After 1900 and until the 1960s, the table photogrammetry gradually moved to the analog photogrammetry. This approach focused on identifying terrain morphology using aerial photographs. In this era, all photogrammetry techniques were based on Stereoscopy.
- After the 1960s, analog photogrammetry was replaced by analytical photogrammetry. This technique used analytical solutions to determine terrain morphology.
- In the 2010s, with the development of new technological devices and software, digital photogrammetry became wide-spread. Digital photogrammetry uses analytical methods and stereoscopic measurements. With the availability of computers and digital cameras, digital photogrammetry has become one of the cheapest surveying methods.

Photogrammetry technique

Modern photogrammetry uses structure-from-motion (SFM) algorithm and multi-viewpoint stereo (MVS) algorithms to recover a three-dimensional (3-D) structure from the projected two-dimensional (2D) moving object or scene. (Fonstad et al. 2013; Quiñones-Rozo et al., 2008). The SFM algorithm does three things in the 3D model building process.

- Calibrate the camera and optical system.
- Determine the relative position and orientation of the camera for each photo corresponding to the imaging subject.
- Generate a sparse point cloud of 3-D points from finding and matching locations in two or more photographs that depict the same feature on the imaging subject.

During image processing, the algorithm identifies camera parameters and improves the accuracy of the camera parameters and orientation iteratively. Therefore, it is not necessary to use a calibrated camera/lens combination to take photographs. Also, the SFM algorithm can identify the camera's position and orientation, relative to the imaging subject. SFM algorithms use a set of matched point correspondences to identify camera parameters and orientation. These matched points are found in the photographs captured from different positions and orientations relative to the imaging subject (Quiñones-Rozo et al., 2008; Schindler, 2015).

The SFM creates points in a sparse cloud using the matches of similar pixel neighborhoods identified in multiple photos. If matching pixel neighborhoods are found in two, or more photos, the areas occupied by the pixel neighborhoods in the respective photos are projected into the virtual 3-D scene and represented as points in the sparse cloud (Mikhail et al., 2004). The precision of points can be increased by increasing the angle between two photographs which include the same object (camera intersection angle).

The precision of the camera parameters, orientation, and precision of the points are interrelated, and precision improvement in any one of these three components will improve the precision of the other two. During the model building process, the SFM algorithm enhances the precision of the model up to the fraction of a pixel, and then multi-viewpoint stereo (MVS) algorithm further improves the precision of the 3D model. Then surfacing algorithm is used to create the texture of the object. It is required to introduce real-world measurements to the model to get the measurement from the developed 3D model. The 3D model can be rescaled to the real-world measurement by providing coordinates of known three points or providing distance between two points. Main steps of the photogrammetry process are shown in Figure 2-4. SFM algorithm is applied in the second and third steps. Then the MVS algorithm is used to process from the fourth step to the sixth step. Scaling and geo-referencing the model is a manual process which will be done in the next step.

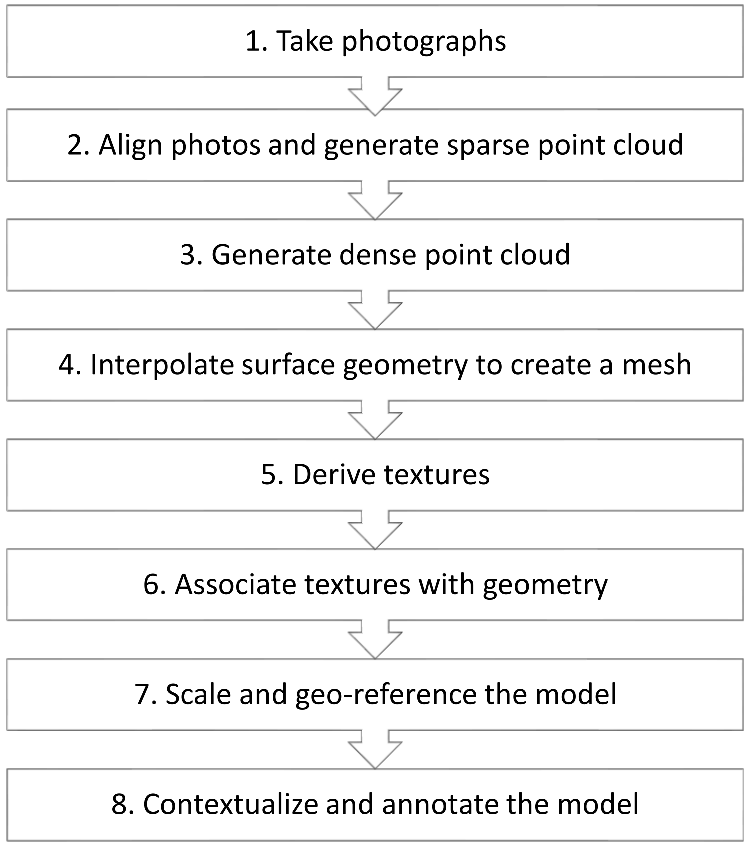

Figure 2-4: Main steps of the photogrammetry process

Image processing software

Several photogrammetry software packages exist on the market; Photomodeler, Agisoft PhotoScan, 3-DF Zephyr, Photosynth, Reality capture, Socket Set, Autodesk 123D Catch, Visual SFM are the popular photogrammetry software among them. Photomodeler Scanner is used for the present study.

- **Photomodeler**

Photomodeler Scanner, version 2017.1.2, was developed by Eos Systems Canada (Eos Systems Inc., 2013). Photomodeler Scanner was designed to create 3-D models and accurate 3D measurements from standard images taken by digital cameras. It is capable of creating accurate, high-quality 3-D models from photographs. Photomodeler uses structure-from-motion (SFM) algorithms and multi-viewpoint stereo (MVS) algorithms to build 3-D models.

According to the Photomodeler user guide, accuracy of the 3-D model developed using the Photomodeler depends on the resolution of the camera, a method which used to calibrate the camera, and photo redundancy. Photomodeler can read images in well-known image formats such as JPEG (.jpg), Tiff (.tif), Windows bitmap (.bmp) and can export 3-D models in Rhino 3-DM, DXF file formats. Table 2-5 shows how the accuracy scale varies with those factors.

Table 2-5: Accuracy scale of the Photomodeler (PhotoModeler Technologies 2008)

Accuracy Level	Lowest accuracy	Average accuracy	Highest accuracy
Camera resolution	640 X 840	5-6 mega pixel	11 mega pixels
Camera calibration method	No calibration	Camera calibrator	Field calibration
Photo redundancy	Points mostly on only 2 photos	All points on 3+ photos	Most points on 8 or more photos
Accuracy	1 part in 100	1 part in 5000	1 part in 30000+

The accuracy figures “1 part in NNN” are the one sigma standard deviation accuracies. At 1 part in 30,000 on a 3m object, point positions would be accurate to 0.1mm at 68% probability (one sigma) (PhotoModeler Technologies, 2008). Nikon D750 and Sony A7R are the two digital cameras that can provide the highest level of accuracy according to Table 2-5. Compared to the other photogrammetry software available in the market, Photomodeler offers automated feature detection and matching of photos and additional tools to improve the quality of the 3-D model.

Image collection

- **Digital camera**

Digital photogrammetry technique requires digital images taken by a digital camera or scanned copy of printed photographs. A higher resolution image contains more details of the object surface, and the resolution of the image is one of the factors which determines the resolution of the final 3-D model (Schindler, 2015). In these studies, two digital cameras were used, and both cameras satisfy the recommendations of the performance of photogrammetric systems study by Gales-Jorge (González-Jorge, 2011).

Figure 2-5: Nikon D750 With Nikon 50mm AF-S f/1.8G Nikkor lens

Nikon D750 is a digital single lens reflection camera developed by the Nikon Corporation, Japan. It has a full-frame (35.9 x 24 mm) CMOS sensor with 24.3-megapixels (Figure 2-5). Native ISO sensitivity of the camera sensor is 100 to 12800 ISO. Therefore, the camera is capable of capturing low noise images even in the low light situations at higher shutter speed. Nikon D750 is capable of operating through the Wi-Fi network remotely.

DXOMARK is an online application which provides results of lab experiments conducted to assesses image quality of smartphones, lenses, and cameras using industry-grade lab tools (http://www.dxomark.org). According to the DXOMARK, the combination of Nikon 50mm AF-S f/1.8G Nikkor full frame prime lens and Nikon D750 camera has a distortion of +0.4% (Table 2-6).

Figure 2-6: Sony A7R with Sony 50mm f/1.8 lens

Sony A7R is a mirrorless digital camera introduced in 2013 by Sony Corporation, Japan (Table 2-6). The weight of the camera is low and suitable to mount in the frame or UAV. It has 36.4-megapixel full-frame (35.8 x 23.9 mm) CMOS sensor. The camera is capable of taking low noise sharp photographs under low light conditions, native sensitivity of the camera sensor is 100-51200 ISO. This camera comes with a Wi-Fi capability and capable of operating remotely using a Wi-Fi network. Sony f/1.8 prime lens has 50mm focal distance. Combined lens camera setup is capable of producing sharp low distorted images with 16-megapixel sharpness and 0.1% distortion (Table 2-7). Also, these lens-camera combinations are more convenient to use in the field.

Table 2-6: Test values of Nikon D750 with Nikon 50mm f/1.8 lens

Sharpness	17 P-Mpix
Transmission	2 TStop
Distortion	0.4 %
Vignetting	-1.7 EV
Chromatic aberration	8 µm

Table 2-7: Test values of Sony A7R with Sony 50mm f/1.8 lens

Sharpness	16 P-Mpix
Transmission	1.8 TStop
Distortion	0.1 %
Vignetting	-1.9 EV
Chromatic aberration	4 µm

Focus adjustment

In terrestrial photogrammetry, the camera is placed above the soil surface at the height of approximately 2m above the soil surface. The coverage area of one photo frame (field of view) is a function of the distance between the camera and the object, and the angle of view of the lens. Equation 2-3 shows the relationship between the field of view (f_v), the horizontal angle of view (α), the vertical angle of view (β) and the distance between the camera and the object (u).

$$f_v = 4u^2 \left(Tan\left(\frac{\alpha}{2}\right) Tan\left(\frac{\beta}{2}\right) \right) \tag{2-3}$$

For the proposed camera setup, distance between camera and the object is 2m, α is 39.6 degrees and β is 27 degrees. According to the Equation 2-3, proposed camera setup covers 1.5 m by 0.94m of the surface area. The depth-of-field (D_f) is given by the Equation 2-4.

$$D_f = 2u^2NC/f^2 \tag{2-4}$$

Here, u is the distance between the object and the camera, N is the aperture of the lens, C is the circle of confusion, and f is the focal length of the lens. For Nikon 50mm lens circle of confusion is 0.26mm. Figure 2-7 presents a chart of focus distance versus lens aperture for Nikon D750 + 50 mm lens setup. It shows that for the range of aperture from f/8 to f/18, the minimum to maximum focus distance is within 1.5 m to 3.5 m. When the aperture number gets higher, the shutter speed of the camera becomes lower. Therefore, to avoid blurry images due to possible camera vibrations, the shutter speed is recommended to set below 1/200s.

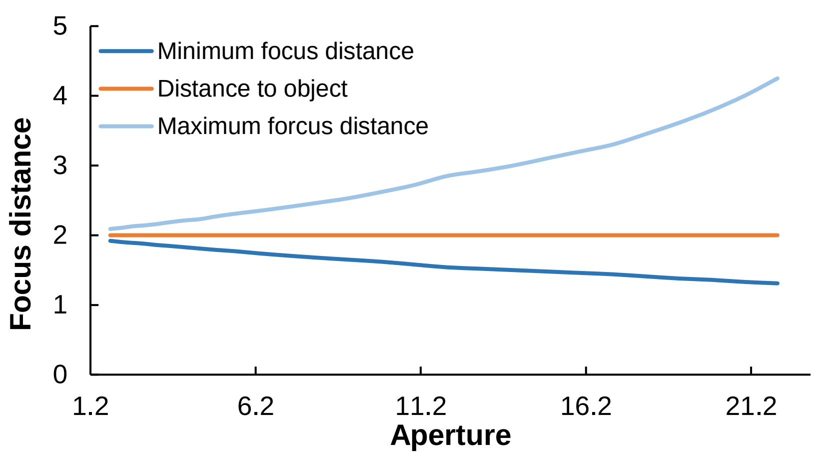

Figure 2-7: Variation of minimum and maximum focus distance with the aperture

- **Camera calibration**

The process of camera calibration provides a set of parameters characterizing the mechanical arrangement of the elements of a camera and a lens. Camera's focal length, lens distortion, format aspect ratio, and principal point are the parameters recover from the calibration process. Photomodeler offers two types of camera calibration options. Calibrate camera using printed objects provided by the Photomodeler software and calibrate the camera using field data. Both approaches were used for camera calibration in this study.

Photomodeler algorithm is capable of identifying camera parameters without calibration. However, the user guide recommends calibrating the camera to improve the accuracy of the 3-D model. After the calibration process, the identified camera parameters: camera's focal length, lens distortion, format aspect ratio and principal point, are shown in Figure 2-8 for two camera setups.

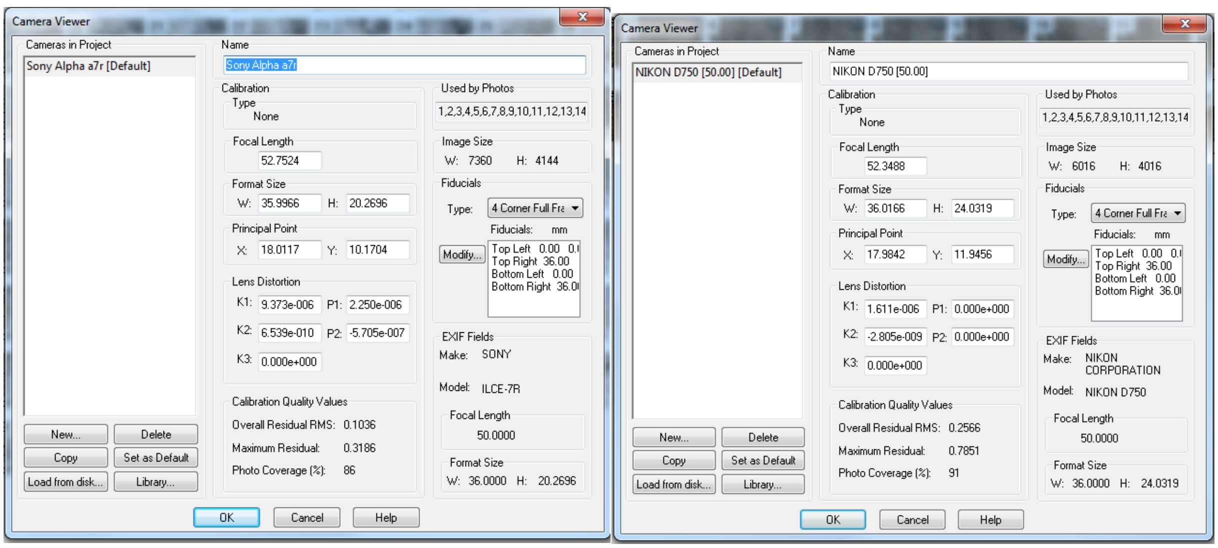

Figure 2-8: Camera parameters after the camera calibration process

Photomodeler calibrator

The camera calibration process requires 15 calibration sheets printed from within the software (Figure 2-9). The printed sheets are firmly attached to the flat surface and required taking 10 to 15 photographs in different angles in such a way that a camera frame covered more than 70% of the calibration sheets. Within the photoshoot, the camera was in manual focus mode to ensure the constant focal length. In the calibration process, the distance was maintained between the camera and the calibration sheet same as the actual distance between the camera and the object. In the case of EG terrestrial surveying, that distance was selected as 2m. Then the photographs were fed to Photomodeler software and ran through the automated calibration process. At the end of the calibration process, the application estimated the camera parameters presented in Figure 2-8.

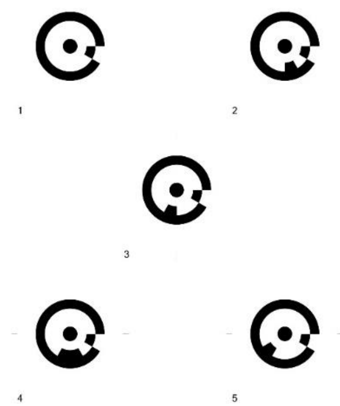

Figure 2-9: Calibration sheet

Field calibrator

Another calibration approach, field calibrator, is a manual process. To run the field calibrator, initially, we built a 3-D model using the Photomodeler. Then the software allowed to mark points on the 3-D surface and provide the actual distance between the marked points. Using the provided data, the software calculated the camera parameters shown in Figure 2-8.

Build the 3-D model

After the camera calibration process is completed, images from the camera can be used to build 3-D models of actual objects. In the Photomodeler, the user can use an automated point cloud generation option. In the model building process, first, Photomodeler orients the photographs and identifies the camera locations using the SFM algorithm. Then using MVS algorithm, Photomodeler detects points in the object surface which are common to several photographs. In the Photomodeler environment, those points are called ‘smart points’. A collection of those points is called a ‘point cloud’. The scale of this initial model is different from the actual object. To rescale this model user must introduce the real scale. This process will be discussed under the topic geo-referencing the 3-D model.

Geo-referencing the 3-D model

It is required to import the actual coordinate system to the 3-D model to get measurements from the 3-D model. This process is called georeferencing. First, it is required to identify the relative locations of the geo-reference points on the point cloud. For this process, the user can use photographs which were used to build the 3-D model. When the user mark points on the photograph, the software identifies the corresponding location of that point on the 3-D model. To accurately identify the relative location on the point cloud, the particular marked point must be included in at least three photographs. After locating all the reference points, the user can import coordinates of those reference points and model re-projects according to the new coordinate system.

Adjust the model to improve the accuracy

The Photomodeler project report provides all the information about the project. The project report is attached in Appendix-A. If the project had issues, it provides suggestions to avoid those issues. The project report also includes the maximum, minimum and overall error occurred in the reference points marked by the user. The residue error in the reference point marking must be below 1 pixel. The summary of the photographs shows how each photograph affects the total error of the model. By removing bad photographs and re-running the model, improves the accuracy of the model. Point quality table also provides how accurately the location of each point is predicted.

Adding new photographs, removing high residue points, an increasing number of iterations will improve the quality of the project. After all those model building procedures, users can export the 3-D model in any file type described earlier in the Photomodeler section. A portion of a point cloud which is exported as a text file is attached in Appendix-B.

Accuracy factors

Several factors affect the accuracy of the 3-D Digital Surface Model (DSM) (Luhmann et al. 2006). The factors can be summarized as properties of the selected digital camera (camera resolution and camera calibration method), the way the photographs are taken (camera angle, surface coverage, photograph overlap), image overlap percentage and the number of GRP. Agüera, Carvaja, and Martínez (2017) conducted an experiment to examine how the number of geo-referenced points and density of geo-referenced points/ground reference points (GRP) affected the accuracy of the photogrammetry survey and found that GRP density affects the accuracy of the photogrammetry model. The Minimum error occurred at the 15 GRPs setting, and the minimum RMSE values were 4.5 cm along the horizontal direction and 4.6 cm along the vertical direction.

- **Image resolution**

Resolution of the image is defined by the sensor size of the digital camera which is used to take photographs. The higher the resolution of the sensor, the smaller the smallest grid-cell (pixel) with uniform color. Higher resolution sensors can locate subjected targets more precisely compared to the lower resolution sensor, and a high-resolution image contains more spatial information compared to the lower resolution sensor (González-Jorge, 2011).

- **Orientation**

Location and the angle of the camera are called the orientation. Maintaining the same angle with the camera sensor and the soil surface increases the accuracy of the photogrammetry model (Dai, Fei Lu, 2012).

- **Photo redundancy**

If a point appears in many photographs, then the position of that point can be computed more accurately. This phenomenon is called photo redundancy, and photo redundancy can be increased by increasing the photo overlap percentage (Schindler, 2015).

- **Camera intersection angle**

Points and objects that appear on photographs with shallow subtended angles (for example, a point appears in only two photographs that were taken very close to each other) have much lower accuracy than objects on photos that are closer to 90 degrees apart (Mikhail et al., 2004). For a small intersection angle, the AB, AC lines(Figure 2-10) are nearly parallel, and small calculation error of the intersection angle push the intersection point of AB, AC lines further compared to the small angle error occur at the large intersection angle.

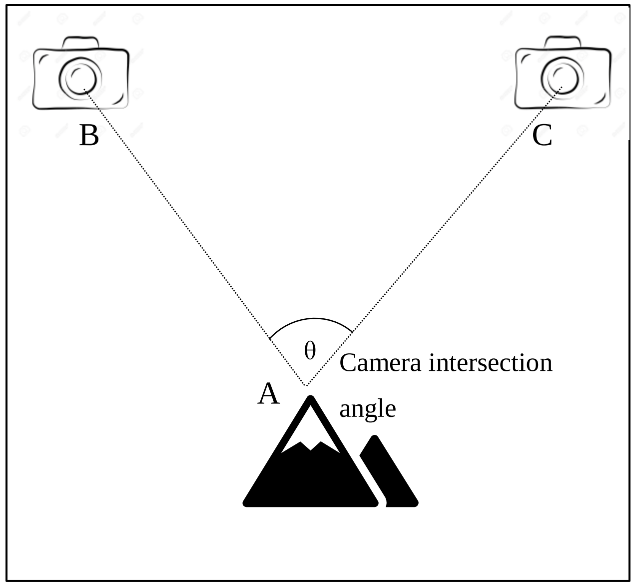

Figure 2-10: Angle between two photographs

The accuracy can be affected by the morphological features of the channels in agricultural fields. The suitability of aerial photographs for stereoscopic analysis can be obstructed by shadows cast over the inner surface of the gullies to some extent. These undesirable shadows will depend on the sunrays, and the length of the shadows is a function of the width-to-depth ratio of the channel. Consequently, there are suitable and unsuitable hours during the day and months throughout the year to successfully carry out photogrammetric analysis of gullies of different typology (Rose et al., 2009).

3 Mapping Accuracy of the Photogrammetric Approach for Environmental Applications

3.1 Introduction

This chapter describes the laboratory test conducted to check the adequacy of the proposed photogrammetry method to survey the ephemeral gullies (EG) in agricultural fields. In this study, the number of the ground reference points (GRP), the spatial distribution of GRPs, camera angle, and overlap percentage of two consecutive images were evaluated. The root mean squared error (RMSE) was used to compare 3-D models with the actual measurements. The optimal number of GRPs and optimal spatial distribution of GRPs were determined using the error statistics such as RMSE. Analysis of variance (ANOVA) method was used to check whether any significant difference between 3-D models built using different camera angles and overlap percentages. The optimal number of GRPs obtained from this experiment were used to design the field study.

The accuracy of the photogrammetry model depends on the following factors related to image collection and processing (Luhmann et al., 2006);

- camera resolution
- camera calibration method
- angles between photographs of the same object
- photo orientation quality
- photo redundancy
- number of GRPs
- morphological features

A photogrammetry accuracy study was conducted by Vega, Ramírez, and Carricondo (2017) to identify the impact of the number of GRPs on the accuracy of the photogrammetry model. For this test, the study area was 17.64 ha, and 120 m altitude airborne platform was used to take photographs. Error analysis was conducted to identify the accuracy improvement with an increase of the number of GRPs. In Vega's study, the error analysis was done by considering 4, 5, 6, 7, 8, 9, 10, 15, and 20 GRPs and five replications under each number of GRPs. Each time GRPs were identified and surveyed for X, Y, Z coordinates. The final 3-D maps of DEM were obtained with 3.3 ± 0.346 cm horizontal accuracy and 4.7 ± 0.860 cm vertical accuracy. This experiment used airborne platform 120m above the soil surface. In contrast to the Vega's experiment, the photogrammetry survey method proposed in this study uses 2m altitude platform to hold the camera and take photographs. Therefore, it is essential to determine an optimum number of GRPs corresponds to the proposed photogrammetry method.

Dai, Feng, and Hough (2014) found that the accuracy of the photogrammetry model varies with the overlap percentage. From 90% to 50% overlap, the standard error decreases as the overlap percentage decreases. From 50% to 20% overlap, the standard error increases with the overlap percentage decreases. They obtained the minimum standard error (0.001) at 50% overlap. However, the influence of each factor varied with the scale and the type of the photogrammetry project. Therefore, the main goal of this study was to conduct a lab experiment to evaluate the adequacy of the photogrammetric mapping approach for surveying EGs on agricultural fields with exposed soil. The specific objectives were to:

- Evaluate the optimal number of ground-reference points
- Assess optimal spatial distribution of the ground-reference points
- Compare the effect of camera angle on the accuracy of the model
- Compare the effect of photograph overlap percentage on the accuracy of the model

3.2 Materials and Methods

The summarized lab experiment process is shown in Figure 3-1.

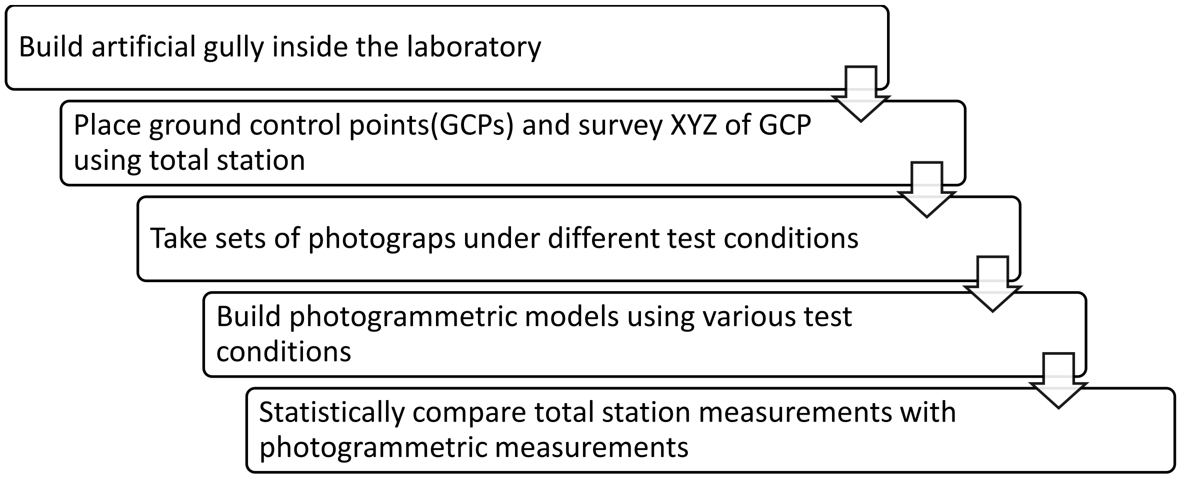

Figure 3-1: Main steps followed in the experimental process

Experimental setup

The experiment was conducted in the workshop of the Department of Biological & Agricultural Engineering, Kansas State University. A soil bed of 4m in length, 1m in width, and 0.4m in depth were built to represent a surface terrain of the agricultural field. The soil bed was filled with topsoil purchased from the local home improvement store (Home Depot; item #100355705) and analyzed for texture and organic matter in the soil testing lab at Kansas State University (http://www.agronomy.k-state.edu/services/soiltesting/). The soil was spread over and distributed within the soil bed to create a uniform soil layer of 40 cm. The characteristics of the soil are presented in Table 3-1

Table 3-1: Composition of the soil used to build artificial gully inside the laboratory

Sand	18%
Silt	50%
Clay	32%
Organic matter	10.3%

A channel of about 30 cm depth and from 15 cm to 40 cm in width was shoveled inside the soil bed. The width and depth of the artificial channel were close to observed actual gullies on agricultural fields in the northeast and central Kansas region (Karimov and Sheshukov, 2017; Karimov, 2017). During the experiments, room temperature ranged from 25^{0}C to 30^{0}C, and average soil moisture content was estimated at ~25% by soil sampling.

Sixty survey plastic stakes (or ground control points - GCPs) of 12 cm length were inserted into the soil surface and formed a 4 by 15 element grid, each apart from each stake by roughly 25 cm (Figure 3-2, Figure 3-3(b)). Five subsets of stakes each with sample sizes (4, 8, 12, 16, 20) were selected as ground-reference points (GRP) in each treatment. A small drill bit was used to mark a survey point on top of each stake's head. The drill mark was colored white, which made a high contrast between the survey point (drill mark) and the dark surrounding platform (stake head). This contrasted mark helped to identify the survey points on the photographs.

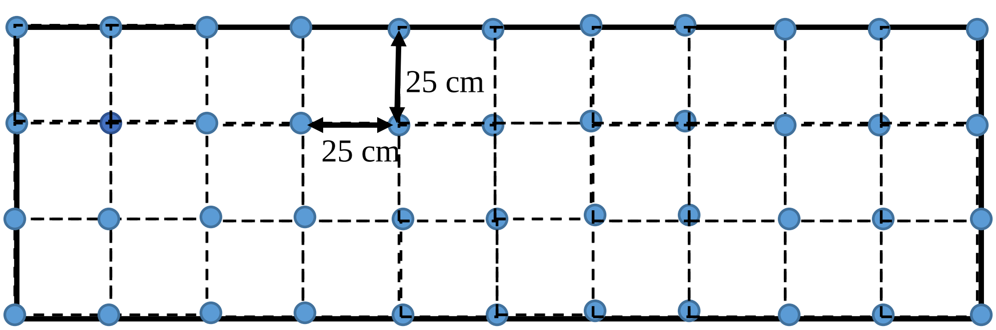

Figure 3-2: A diagram of reference points

Coordinates X (along the Northern), Y (along the Eastern) and elevation Z of all survey points were surveyed with a total station. The accuracy of the total station along the vertical and horizontal planes are < 1.5 mm when the laser is located less than 50 m from the object ("Zoom40 Series | GeoMax"). Each of 60 GCPs was surveyed with the total station three times. For each stake, an average of the three surveyed X, Y, and Z coordinates were calculated and assumed as "true." The possible error was assumed negligible because the distance between the location of the total station and any stake was less than 15 m ("Zoom40 Series | GeoMax").

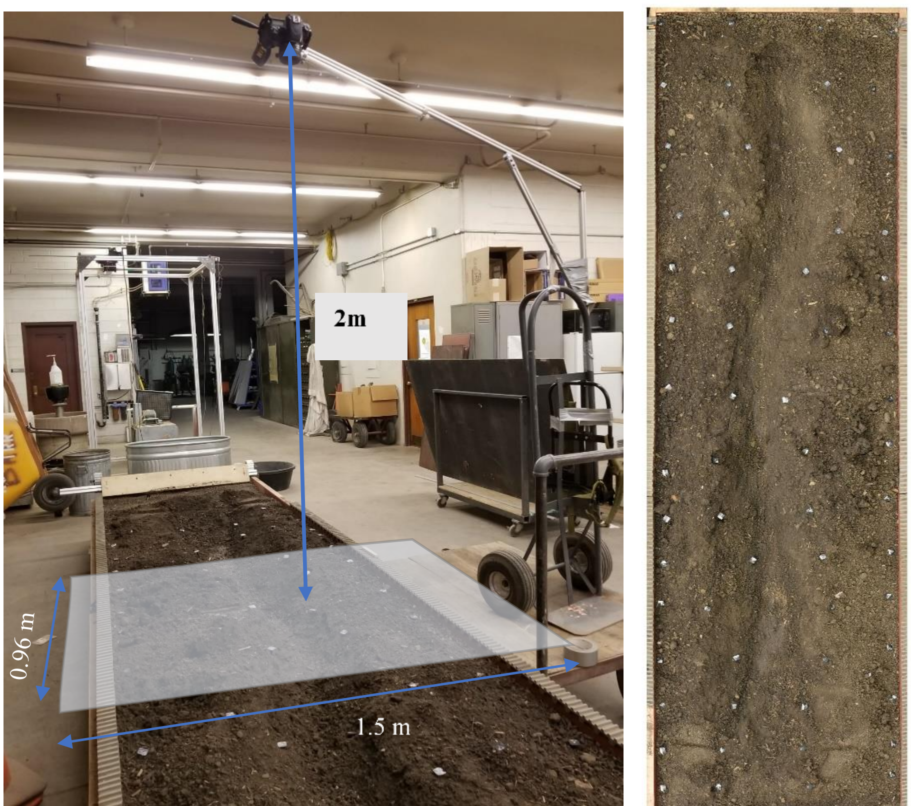

a **b**

Figure 3-3: The experiment set-up and GCP distribution on the soil bed

Image collection and processing

For this study, a high-resolution full-frame digital camera, Nikon D750 was used to take photographs. The camera has a 24.4 megapixels full-frame CMOS sensor and a full frame 50 mm Nikon AF-S f/1.8G Nikkor prime lens. The camera was attached to a platform of a truck using a metal frame. The camera was mounted on an arm of the aluminum frame, 2m above the soil surface to match to the real-world conditions. With this setup, one photo frame covered a surface area of 1.5 m by 0.94 m (Equation 2-3). The distance between the camera and surface of the soil bed varied between 1.5 m to 2.5 m. According to Figure 2-7, lens aperture was set to f/14 and shutter speed was set to 1/200 s to assure that the image was in focus. The camera was connected to the tablet wirelessly by a Wi-Fi signal; thus, the camera operator was able to activate the camera shutter and see the live view through the tablet screen.

Nine collections of photographs of the study area in the soil bed were taken using three different tilted camera angles, and three images overlap percentages: angles of 0^0, 20^0, and 30^0 and overlap percentages of 30%, 60%, and 90% respectively. Table 3-2 shows the number of photographs taken under each setting.

Table 3-2: Number of photographs of each scenario by the image overlap percentage and the camera angle.

		Camera angle (degrees)		
		0	20	30
Image overlap	70%	15	15	15
	80%	25	25	25
	90%	30	30	30

To maintain a 90% overlap between two consecutive photographs camera was moved 9cm parallel to the length of the soil bed. The camera was moved by 18cm and 27cm to get 80% and 70% overlap percentages, respectively.

The camera angle was changed using the camera mount. Before taking the photographs, the camera was calibrated using Photogrammetry software, and the camera calibration process was described in Section 2.4.

Photogrammetry software

Model building process, algorithms, and steps were described in section 2.4. The 3-D model building process is summarized as follows;

- Calibrate the camera using specially created calibration sheets.
- Feed photographs to software and create a 3-D model.
- Manually identify the locations of the referencing points and mark them on the photographs.
- Define the coordinate system and assign surveyed coordinates to previously marked locations.
- Check the project status report and adjust the model according to the report to increase the accuracy.

Evaluating the number of ground reference points

The known locations of the soil surface are called the ground control points (GCP), and all of those points or portion of those points can be used to geospatially reference the 3-D model. The points which were used to geospatially reference the 3-D model called the georeference points (GRP). The number of geo-referenced points (GRP) can affect the quality of the photogrammetry model (Agüera et al., 2017). Initially, 60 stakes were surveyed by the total station, and from these 60 GCPs, five subsets (replicates) with different number of GCPs (treatment) were selected for geo-referencing each treatment. For this experiment 4, 8, 12, 16, 20 GRPs (treatments) were used, and each treatment with five replicates. Those replicates were randomly chosen with the same amount of GRPs. Initially, all plastic stakes were numbered from 1-60. Then Microsoft Excel was used to generate 4 random numbers in interval 1-60. Stakes name corresponded to random numbers were selected to geo-reference the 3-D model and rest of the 56 stakes were used to calculate the errors. Likewise, for each treatment, five 3-D models were built using the selected five replicates. Photographs taken with 70% overlap and 0 camera angle were used in this assessment. The locations of the used points are shown in Figure 3-4.

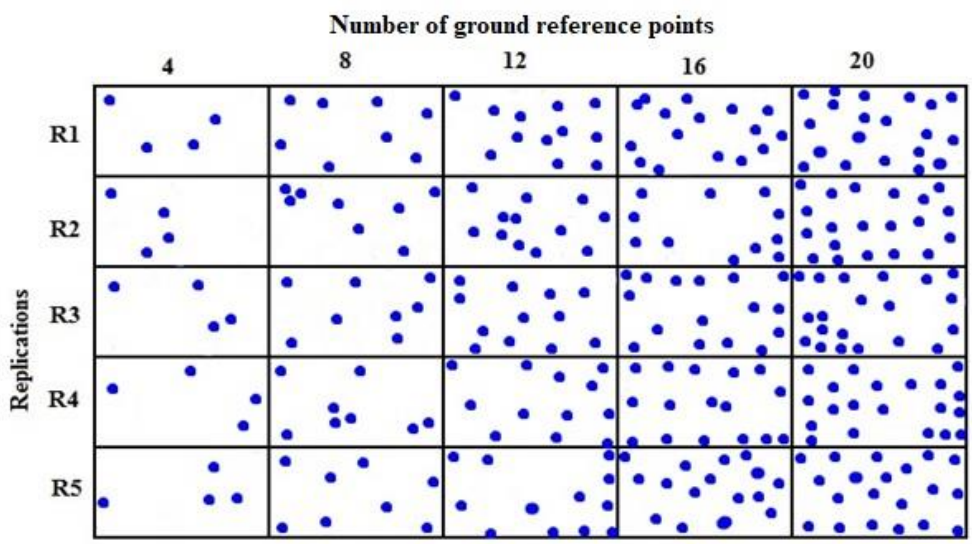

Figure 3-4: Location of the ground reference points

The accuracy was tested by comparing predicted coordinates of the GCPs with the "true" coordinates surveyed with the total station.

Evaluating GRP spatial distribution

Spatial distribution of the GRP affects the accuracy of the photogrammetry model. Five different spatial distributions of GRPs were considered, and the optimum number of GRPs were used for five models. The accuracy was tested by comparing the X, Y, Z coordinates of the GCP with their "true" coordinates collected by surveying with the use of the total station. Root square mean error (RSME) and the variance were used to compare each model. This study also used photographs taken with 70% overlap and 0 camera angle.

Statistical evaluation of GCP coordinates

Errors

Error based analysis was conducted to find the impact of GRPs quantity on the accuracy of the photogrammetry model. In this study, the difference between the total station survey and the value obtained from the 3-D model was considered.

For each photogrammetry project, RMSE along Easting (X), Northing (Y), vertical (Z) directions were calculated by comparing coordinates given by the photogrammetry model and the surveyed points which have not been used for geo-referencing. The number of stakes used to calculate RMSE ranged from 40 to 56 depending on the number of stakes used in the photogrammetric project.

$$Error_x = |x_{oi} - x_{TSi}| \tag{3.1}$$

$$Error_y = |y_{oi} - y_{TSi}| \tag{3.2}$$

$$Error_z = |z_{oi} - z_{TSi}| \tag{3.3}$$

$$Error_{xy} = \sqrt{(x_{oi} - x_{TSi})^2 + (y_{oi} - y_{TSi})^2} \tag{3.4}$$

$$Error_{xyz} = \sqrt{(x_{oi} - x_{TSi})^2 + (y_{oi} - y_{TSi})^2 + (z_{oi} - z_{TSi})^2} \tag{3.5}$$

$$RMSE_x = \sqrt{\sum_{i=1}^{n} \frac{(x_{oi} - x_{TSi})^2}{n}} \tag{3.6}$$

$$RMSE_y = \sqrt{\sum_{i=1}^{n} \frac{(y_{oi} - y_{TSi})^2}{n}} \tag{3.7}$$

$$RMSE_Z = \sqrt{\sum_{i=1}^{n} \frac{(z - z_{TSi})^2}{n}} \tag{3.8}$$

$$RMSE_{XYZ} = \sqrt{\sum_{i=1}^{n} \frac{(x_{oi} - x_{TSi})^2 + (y_{oi} - y_{TSi})^2 + (z_{oi} - z_{TSi})^2}{n}} \tag{3.9}$$

Where n is the number of GRPs used for the photogrammetry process, X_{oi}, Y_{oi} and Z_{oi} are the X, Y, Z coordinates obtained from the photogrammetry process, and X_{TSi}, $Y_{TSi,}$ and Z_{TSi} are X, Y, Z coordinates obtained from the total station survey.

One-way ANOVA test

Analysis of variance (ANOVA) is a statistical procedure for testing the hypothesis that two or more-population means are equal or not (Rutherford, 2011). It compares the means of the samples or groups to make inferences about the population means.

The null hypothesis (H_0) is: all the population means (μ) of k populations are equal,

H_0: $\mu_1 = \mu_2 = \ldots = \mu_K$

and the alternative hypothesis (H_1) is: at least one population mean significantly differs from the other population means.

H_1: $\mu_i \neq \mu_k$

for some i^{th} population and k^{th} population

The One-way ANOVA procedure assumes that data in each treatment group follows a normal distribution and the variability within the group is roughly constant across the treatment groups. In ANOVA, a number of treatment groups are called factor levels (camera angle, overlap percentage) and observations under each factor (treatment) level are called replicates. If the number of replicates under each factor are the same, then it is called a balanced ANOVA. The j^{th} observation of the i^{th} factor is denoted by y_{ij}. Variability between treatment groups captures by the sum of squares of treatment (SSF) and variability within groups captures by the sum of squares error (SSE), and total variability captures by the sum of the square total (SST). For an experiment which has n number of treatments and m number of replicates SSF, SSE, SST can be defined as follows,

$$SSF = m\sum_{i=1}^{n}\left(\overline{y}_{i.} - \overline{y}_{..}\right)^2 \tag{3.10}$$

$$SSE = \sum_{i=1}^{n}\sum_{j=1}^{m}\left(y_{ij} - \overline{y}_{i.}\right)^2 \tag{3.11}$$

$$SST = SSF + SSE \tag{3.12}$$

where,

$\overline{y}_{i.} = \frac{1}{m}\sum_{j=1}^{m}\left(\overline{y}_{ij}\right)$ and $\overline{y}_{..} = \frac{1}{mn}\sum_{i=1}^{n}\sum_{j=1}^{m}\left(y_{ij}\right)$, $MSF = \frac{SSF}{m-1} and\ MSE = \frac{\mathrm{SSE}}{\mathrm{n-m}}$

The ANOVA table is presented in Table 3-3. MSF/MSE follows an F-distribution and probability value (P-value) corresponds to this ratio can be obtained from the F-distribution table. If the P-value is small to the significance level (α), the null hypothesis is rejected, providing more evidence to support that at least one population mean significantly differs from the other population means.

Table 3-3: Structure of the ANOVA table

Source	Sum of squares	DF	Mean Square	F
Treatment	SSF	m-1	SSF/(m-1)	MSF/MSE
Error	SSE	n-m	SSE/(n-m)	
Total	SST	n-1	SST/(n-1)	

Wald–Wolfowitz runs test

A runs-test is a statistical procedure which is used to decide the randomness of the data (Bradley, 1968). Runs test analyzes the occurrence of similar events that are separated by events that are different. The number of incidents of similar events called the number of the runs. For the numeric data, runs can be computed using reference values like mean, median and runs can define as a series of consecutive values above (positive) the reference value and below the reference value (negative).The first step in the runs test is to count the number of runs in the data sequence. Using the number of runs the following test statistic is calculated.

$$Z = \frac{R-\bar{R}}{S_R} \tag{3.13}$$

Where R is the observed number of runs, $\bar{R}$ is the expected number of runs, and S_R is the standard deviation of the number of runs. The values of $\bar{R}$, and S_R are computed as follows:

$$\bar{R} = \frac{2n_1n_2}{n_1+n_2} + 1 \tag{3.14}$$

$$S_R^2 = \frac{2n_1n_2(2n_1n_2-n_1-n_2)}{(n_1+n_2)^2(n_1+n_2-1)} + 1 \tag{3.15}$$

Where n_1 and n_2 denote the number of positive and negative values in the series. In the runs test, the following hypotheses are tested using the above test statistic. Runs test rejects the null hypothesis if $|Z| > Z_{1-\alpha/2;}$ where α is the significance level.

Null hypothesis (H_0): The sequence was produced in a random manner.

Alternative hypothesis (H_1): The sequence was not produced in a random manner.

3.3 Results and discussion

Evaluating the GRP quantity

As discussed in section 3.2 error-based experiment was conducted to evaluate the impact of GRP quantity on the accuracy of the photogrammetry model. For this experiment 4, 8, 12, 16, 20 GRPs (treatment) were used, and each treatment had five replicates. Mean value of mean RMSEs of each treatment and standard deviations of mean RMSE were used to evaluate the performance of the models (Figure 3-5).

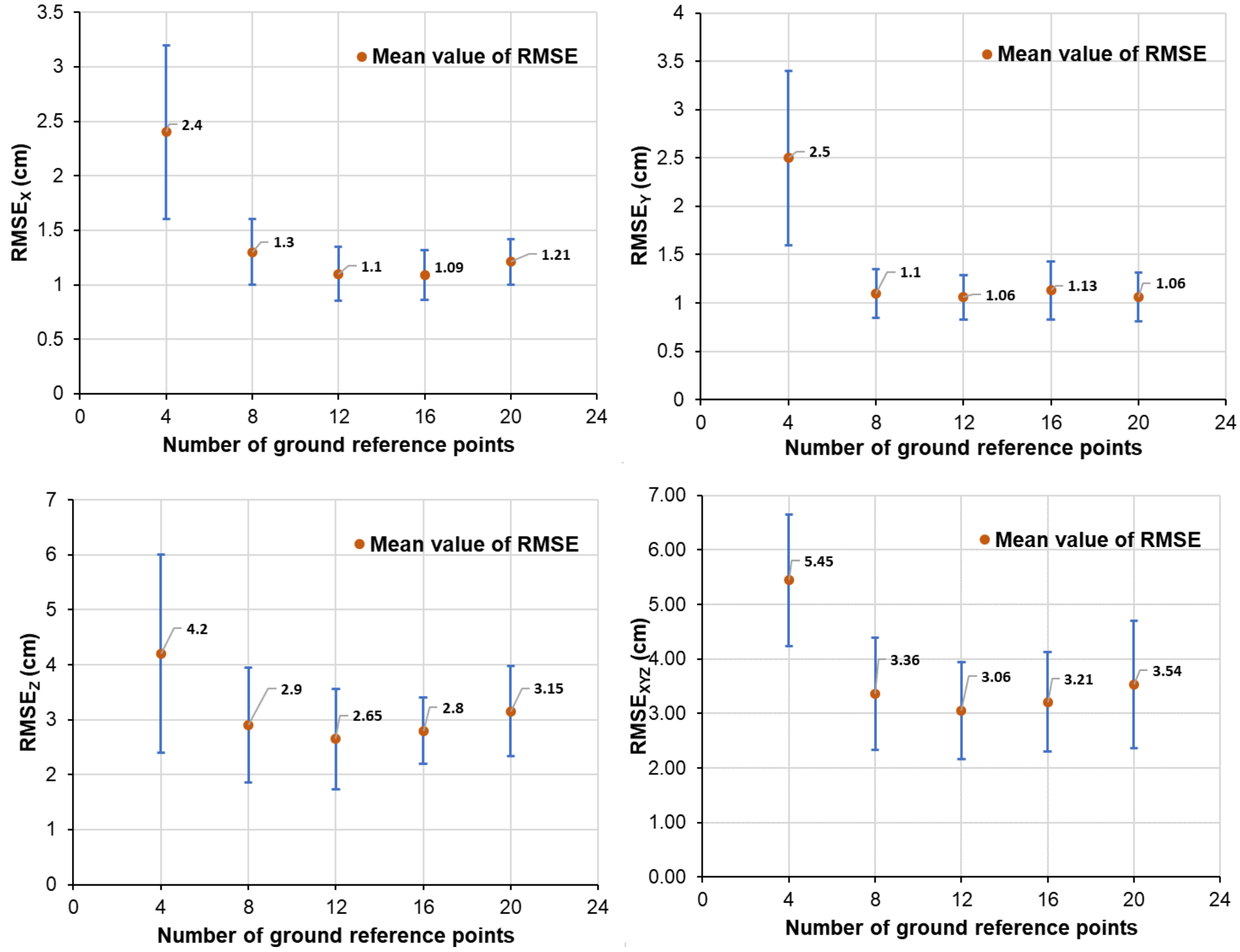

Figure 3-5: Mean value and standard deviation (SD) of the RMSEs under different number of GRPs. Bars indicate the interval of mean+/-SD

Figure 3-5 shows the mean RMSE and mean RMSE ± standard deviation for each treatment along the X, Y, Z axes and the total. There is a dramatical improvement in the accuracy (RMSE value for X, Y, Z combined axis, decrease from 5.45 to 3.36 when the number of GRPs increase from 4 to 8. After that, from 8 to 20 GRPs there is no significant improvement (changing of RMSE is below 0.3cm) in the accuracy with the increase in the number of GRPs. 12 GRPs gave the lowest RMSE value (3.06 cm) along the Y axis and Z axis (2.65 cm). RMSE value for X, Y, Z combined axis reaches the lowest value (3.06 cm) when photogrammetry model uses 12 GRPs. For 12 GRPs RMSE of the X-axis is 1.1 cm and it close to its minimum 1.09 cm. Based on the RMSE and standard error 8, 12, 16 are the optimum number of GRPs. Among them, 12 GRP setting is the best which gives the minimum error. With this setup 12 ground control points result in 1.1±0.25 cm error along the X-axis, 1.06 ± 0.23 cm error along Y-axis and 2.65 ±0.91 cm error along the Z axis.

Evaluating GRP spatial distribution

Based on the optimal GRP evaluation, 12 GRPs setting was the best. Therefore, further studies are conducted using 12 GRPs to analyze the other factors that could affect the accuracy of the photogrammetry. Photographs taken with 70% overlap and 0 camera angle were used to analyze the impact of the distribution of the ground control points. Five photogrammetry models were build using 12 ground control points. Rest of 48 GCPs were used to calculate the RMSE values along the three axes as described in the previous section. Each model had a different spatial distribution of GRPs. The locations of the selected GRPs are shown in Figure 3-6. Ground-referenced points along the edge of the soil bed were used in the first model. The second model used ground-reference points along the edge of the soil bed and middle of the soil bed. The third model used GRPs all over the soil surface. Compared to the other four models these reference points were more randomly distributed along the soil surface. The fourth model used reference points located in the middle of the soil bed, and the fifth model used reference points biased to the one edge.

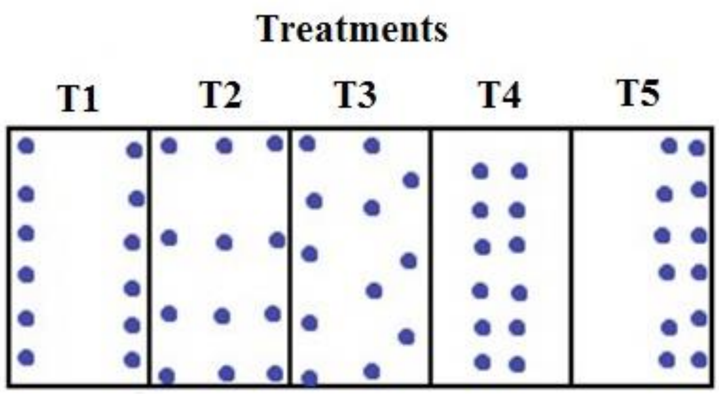

Figure 3-6: Spatial distribution of the ground reference points used to georeference the 3-D model

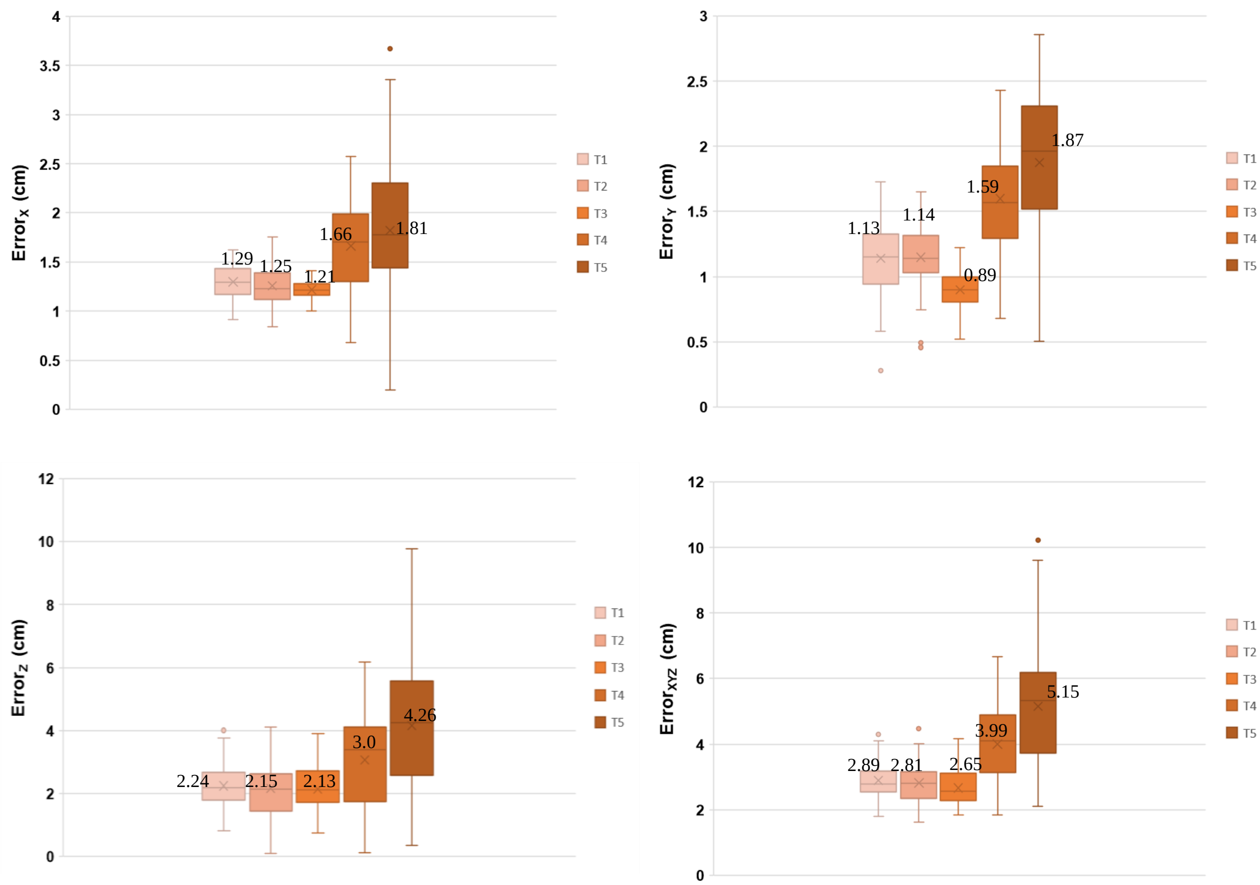

Figure 3-7: Error under each GRP distribution

Distribution of Error for each model is shown in Figure 3-7. Model corresponds to 3rd GRP distribution (R3) gave the minimum error value along all three axes. The minimum error values are 1.22+0.15, 0.86+0.11, 2.07+0.87 along X, Y, Z axis respectively (Figure 3-7). Photogrammetry models which have GRPs R4 and R5 tend to have a rolling effect. Therefore, the accuracy dramatically decreases for this kind of GRP configurations. More distributed GRPs give accurate results.

Based on spatial distribution of GRPs and GRPs quantity tests, randomly distributed 12 GRPs generated more accurate (combined error value is 2.65cm compared to 2.81, 2.89, 3.99, 5.15 cm) results. Therefore, this combination will be used to analyze the effect of the camera angle and the image overlap percentage.

Evaluating image overlap

Error – ANOVA test

Three sets of photographs were used to analyze the effect of the overlap percentage on the accuracy of the model. Photographs were taken with the 0-degree angle, and the overlap percentages of 70%, 80%, and 90%. Three photogrammetry models were built using these three sets. All three photogrammetry models were geo-referenced using pre-defined 12 GRPs. Selected GRPs are shown in Figure 3-8.

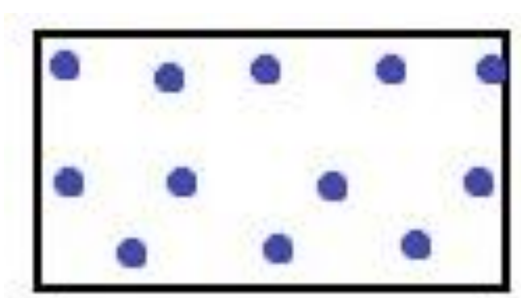

Figure 3-8: Spatial distribution of the selected GRPs

Remaining 48 points were used to calculate the error along the X, Y, Z axes. Then the One-way ANOVA method was used to check whether there is any significant error difference between the three models. Along the X, Y, Z axes three separate ANOVA tests were conducted, and the summary of the ANOVA tests is shown in Table 3-4.

Table 3-4: ANOVA results for image overlap

	Source	Sum of squares	DF	Mean Square	F	P
Along the X axis	Treatment	2.42	2	0.000042	1.61	0.203
	Error	112.80	141	0.000026		
	Total	115.22	143			
Along the Y axis	Treatment	2.64	2	0.000023	0.99	0.375
	Error	98.72	141	0.000024		
	Total	101.36	143			
Along the Z axis	Treatment	3.96	2	0.000193	3.03	0.052
	Error	90.24	141	0.000064		
	Total	94.2	143			

Along the x-axis p-value is 0.203(>0.05), along the y-axis p-value is 0.375(>0.05) and along the z-axis p-value is 0.052(>0.05). All three p values are greater than the significance level (α=0.05). Therefore, there is no evidence to reject the null hypothesis for all three axes. The test provides more evidence to support that there is no significant difference between mean error values generated by three different 3-D models obtained using 70%, 80%, 90% overlap percentages.

Evaluating randomness of the error generated under each overlap percentages.

Wald–Wolfowitz runs test was conducted to evaluate the randomness of errors generated from three 3-D models created using 70%, 80%, 90% overlap percentages. Here the magnitude of the error and direction of the error evaluate separately. The errors and error direction ordered according to the geo-location of the GCP. Table 3-5 shows the results of the runs test. Since all the probability values (P-value) are greater than the significance level (α=0.05). Therefore, there is not enough evidence to reject the null hypothesis. It indicates that the error distribution does not follow any pattern. Figure 3-9 shows the error distribution.

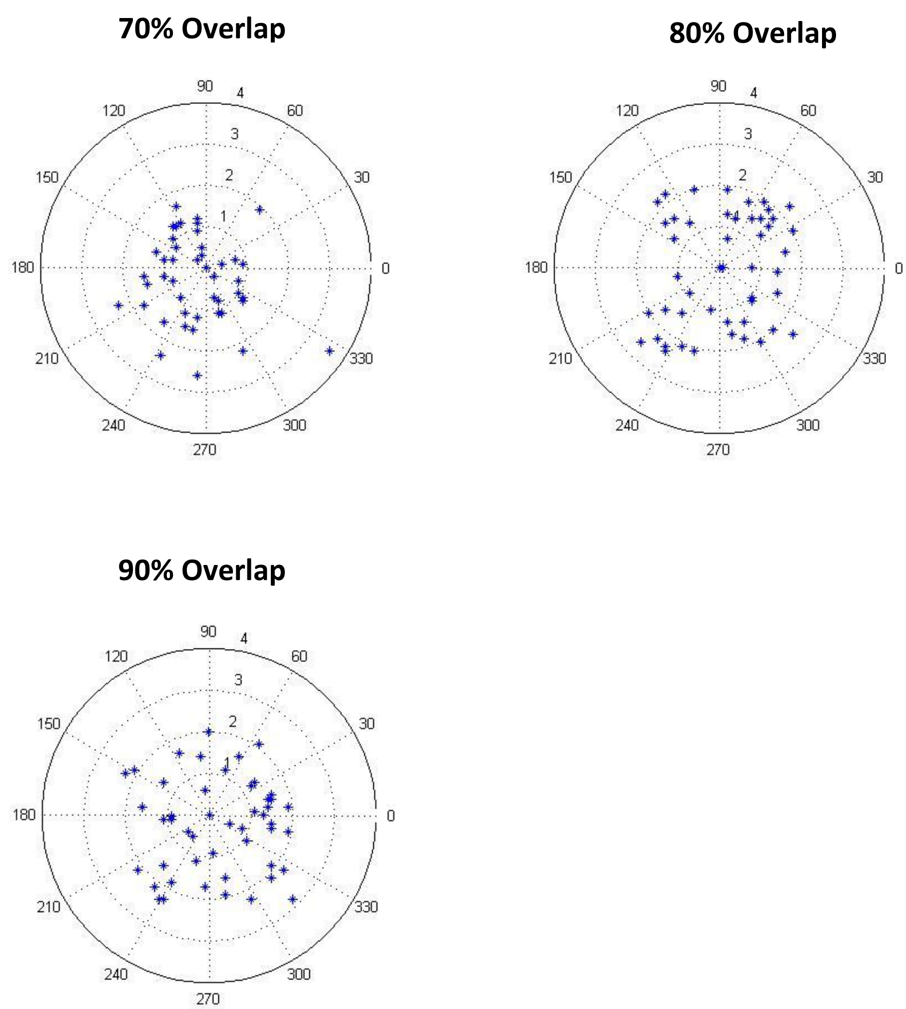

Figure 3-9: Error distribution under 70%, 80%, 90% image overlap percentages

Table 3-5: Runs test results by overlap percentage

		Residual	Direction
70% overlap	Runs above and below	1.24319	-0.321334
	The observed number of runs	24	25
	The expected number of runs	22.9583	23.9583
	observations above	17	19
	observations below	31	29
	P-value	0.739	0.75
80% overlap	Runs above and below	1.70058	-0.217660
	The observed number of runs	18	25
	The expected number of runs	24	24
	observations above	23	23
	observations below	23	23
	P-value	0.074	0.766
90% overlap	Runs above and below	1.55473	-0.243110
	The observed number of runs	18	26
	The expected number of runs	24.4894	24.4894
	observations above	23	23
	observations below	24	24
	P-value	0.055	0.656

According to Figure 3-9 error distribution does not follow any pattern and does not affect the overlap percentage.

Evaluating the camera angle

ANOVA test

Three sets of photographs with 70% overlap percentage and 0^0, 20^0, 30^0 camera angles were used to analyze the effect of the angle of the Camera. Then three photogrammetry models were built, and similar georeferencing procedure described in the previous section (Figure 3-8) was used to georeference the models. Then for each model, the measurement error along X, Y, Z axis were calculated, and the ANOVA method was used to check whether any difference among mean errors generated by three models.

Table 3-6: ANOVA results by the camera angle

	Source	Sum of squares	DF	Mean Square	F	P
Along the X axis	Treatment	2.02	2	0.000022	0.77	0.463
	Error	60.63	141	0.00028		
	Total	62.65	143			
Along the Y axis	Treatment	2.32	2	0.000024	1.00	0.372
	Error	53.58	141	0.000024		
	Total	55.9	143			
Along the Z axis	Treatment	4.42	2	0.000206	2.85	0.061
	Error	97.29	141	0.000072		
	Total	101.71	143			

Along the x-axis p-value is 0.463(>0.05), along the y-axis p-value is 0.372(>0.05) and along the z-axis p-value is 0.061(>0.05). All three p values are greater than the significance level (α=0.05).

Therefore, there is no evidence to reject the null hypothesis for three axes. The test indicates no evidence to support for any significant difference between mean error values generated by three different 3-D models obtained using 0^0,20^0, 30^0 camera angles.

Under the experimental condition, close-range photogrammetry accuracy cannot improve by changing the camera angle. Also, circular charts of error distribution (Figure 3-10) shows that errors do not follow any pattern and do not have any relationship with the camera angle.

Evaluating randomness of the error generated under each camera angle.

Wald–Wolfowitz runs test was conducted to evaluate the randomness of errors generated from three 3-D models created using 0, 20 30 degrees of the camera angle. Here the magnitude of the error and direction of the error evaluate separately. Table 3-7 shows the results of the runs test. Since all the probability values (P-values) are greater than the significance level (α=0.05), there is not enough evidence to reject the null hypothesis. It indicates there is no any pattern of the error distribution. Figure 3-10 shows the error distribution.

Table 3-7: Runs test results by the camera angle

		Residual	Direction
0 Degrees	Runs above and below	1.24319	-0.321334
	The observed number of runs	24	25
	The expected number of runs	22.9583	23.9583
	observations above	17	19
	observations below	31	29
	P-value	0.739	0.75
20 Degrees	Runs above and below	0.0161891	-0.368489
	The observed number of runs	22	28
	The expected number of runs	24.8333	24.9583

	observations above	26	23
	observations below	22	25
	P-value	0.405	0.374
30 Degrees	Runs above and below	1.54531	-0.0178024
	The observed number of runs	24	26
	The expected number of runs	24.9583	24.9583
	observations above	23	23
	observations below	25	25
	P-value	0.779	0.761

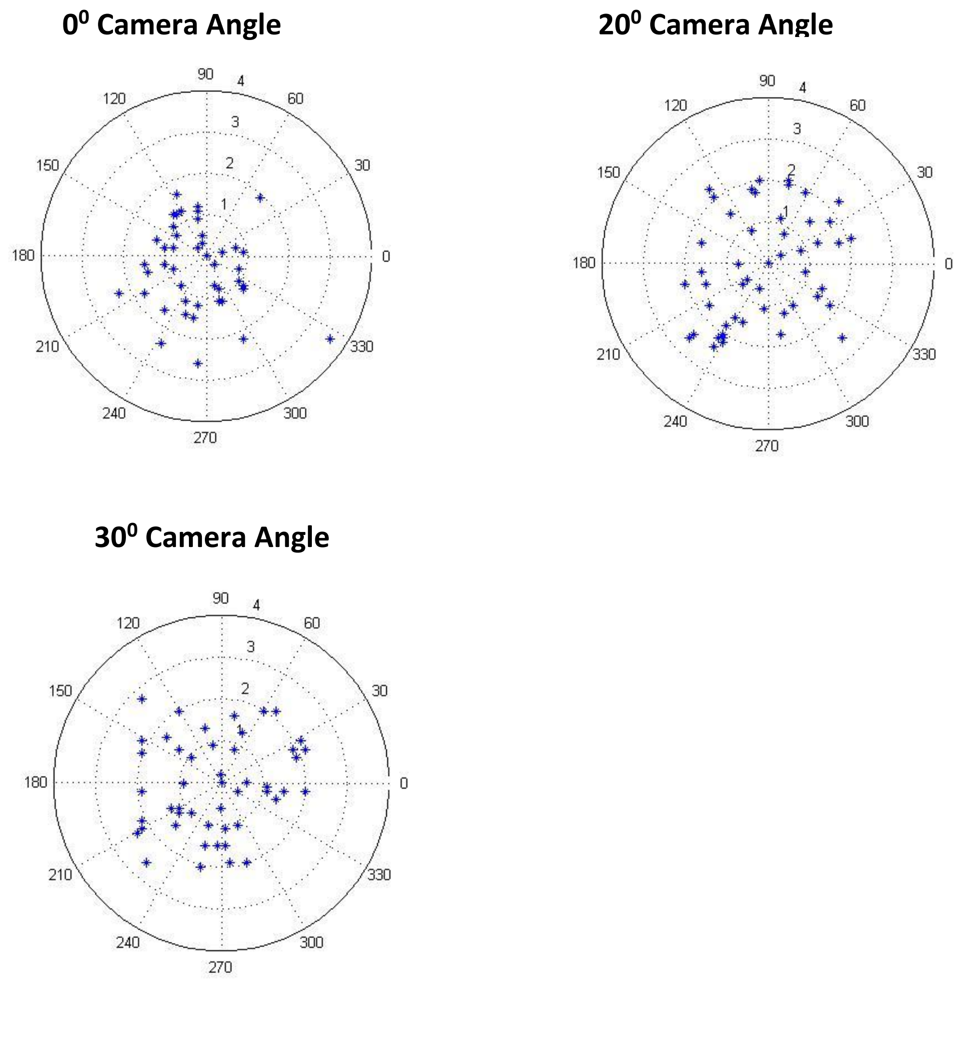

Figure 3-10: Error distribution under 0, 20, 30 degrees of camera angles

Table 3-8: Number of points in the point cloud by a different combination of camera angles and image overlap percentages

Camera angle	Overlap percentage	Number of Points
0	70	1159158
0	80	1487039
0	90	1717755
20	70	1163057
30	70	1168433

Point density map

The results conclude that under this experimental condition, increasing overlap percentage beyond 70% and changing the camera angle between 0 degrees to 30 degreed does not make a significant change in models. Figure 3-11, and Figure 3-12 show the number of points included in the 5cm X 5cm grid cell. The point density varies from 0-1400 points per 25cm^2 (Figure 3-11). The point density dramatically increases (70% overlap generates 724 points per 25cm^{2,} and 90% overlap generates 1074 points per 25cm^2) with the overlap percentage, but the camera angle does not show a significant impact (0 degrees camera angle generates 730 points per 25cm^{2,} and 30 degrees camera angle generates 1074 points per 25cm^2) to the point density (Table 3-8, Figure 3-12).

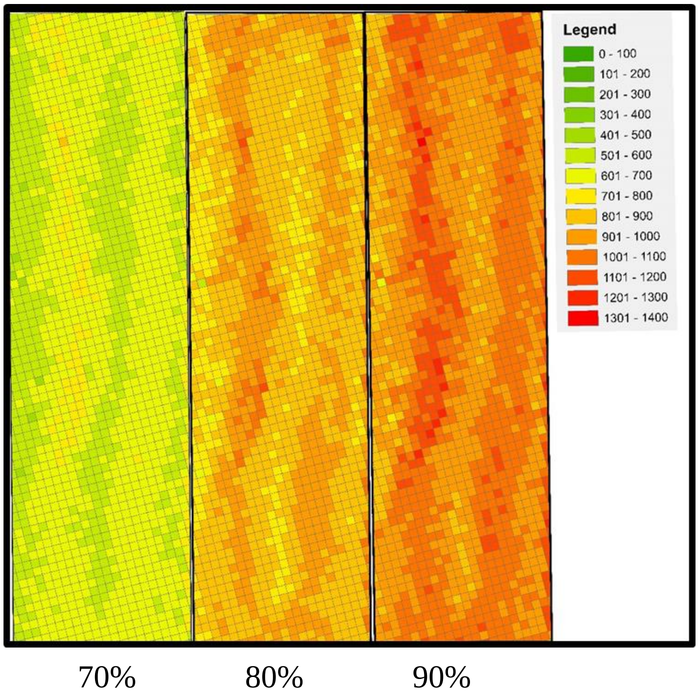

Figure 3-11: Resolution variation with the overlap percentage

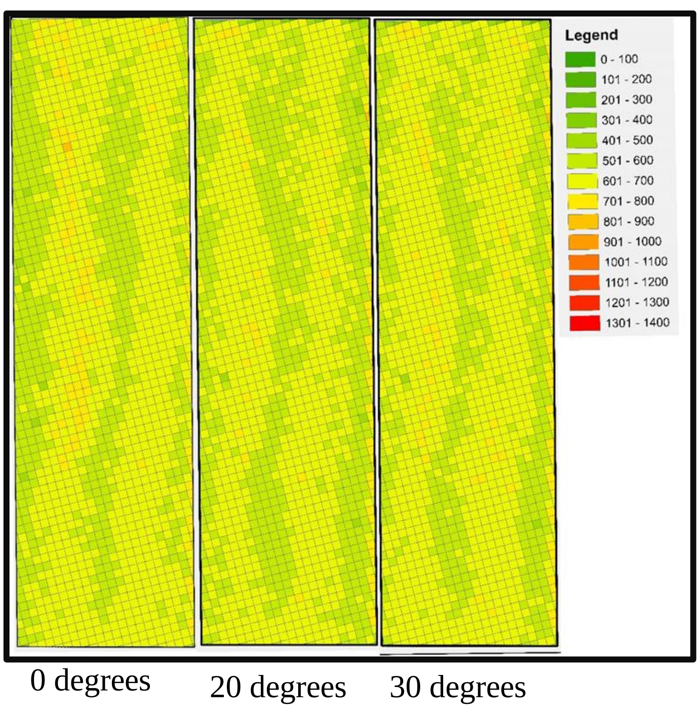

Figure 3-12: Resolution variation with the Camera angle

3.4 Conclusions

The results of this study showed that the proposed photogrammetry method had higher accuracy with 12 ground reference points (GRP) while a range of 8 to 20 GRPs per $4m^2$ of GRP density was deemed acceptable. Therefore, in a real-world situation, 2- 5 GRPs in an area of $1m^2$ is acceptable. The increment of 4 GRPs from 8 to 12 increases the total accuracy by 8.9% and an increment of 8 GRPs from 8 to 16 increases total accuracy by 4.4% while increment of 12 GRPs from 8 to 20 decreases the total accuracy by 5.3%. For large scale projects, 2 GRPs per $1m^2$ of GRP density will require less labor and time in field surveys.

Spatially distributed ground control points generate more accurate results compared to the biased ground control point distribution. It is essential to avoid using a distribution of ground control points located only in one side of the gully, as that type of ground control point distribution creates a rolling effect on the 3-D model and introduces additional errors. It was identified as the camera angle, and the overlap percentage does not affect the accuracy of the photogrammetry model. However, overlap percentage affect the spatial resolution of the model; a higher overlap percentage (90%) produces a more detailed (1074 points per $25cm^2$) 3-D model. However, with the 70% overlap percentage, the system was capable enough to produce an image that has a 1cm resolution. Therefore, a 70% overlap percentage is sufficient to model the EG erosion.

According to the results of the lab experiment, the proposed photogrammetry method and the camera setup can be used to monitor the morphological changes of the EGs in the agricultural fields. GRP density of 4 ground control points per 1 m^2 has the minimum vertical error of 2.65cm and a total error of 3.21cm. Therefore, 4 ground control points per 1 m^2 of GRP density is recommended to monitor the EGs.

The objectives of the lab experiment were identifying the optimal number of ground control points, identifying the impact of the camera angle, the impact of the image overlap percentage and identifying the best ground control point distribution. In this experiment, four variables (number of GRPs, the spatial distribution of GRPs, Camera overlap angle and image overlap percentage) were analyzed to find how those variables involved with the accuracy of the photogrammetry model. However, all tests are conducted by changing one variable at a time and keeping the other three variables as constants. The combined effect of those variables (interaction effect) may affect the accuracy of the photogrammetry model, and the interaction effect needs to be addressed in future studies.

4 Field Surveying of Ephemeral Gullies in a No-Till Field with Photogrammetry

4.1 Introduction

Topsoil is the most valuable part of the agricultural industry. Soil erosion causes soil degradation and reduces the yield of crops. Ephemeral gully (EG) erosion which is one form of the soil erosion in agriculture field has a significant contribution to the total soil loss compared to the other sources. In Kansas, the contribution of EG erosion can range from 30% to as much as 100% of the total soil loss (Daggupati et al., 2014; National Research Council, 1986). In New York state in the United States, EG erosion has a 17% contribution to total soil loss and 73% in Washington State (Bennett et al., 2000b). In the Loess Plateau of China, EG erosion ranged from 41% to 91% of soil loss(Zheng and Gao, 2000) and the contribution of EG erosion to the total soil loss from water erosion ranges from 10% to 94% worldwide (Valentin et al., 2005). As a result, it is important to specifically address the issue of EG erosion separately from other erosion sources. The physical process of EG development not well understood yet and there is a growing need to have more insights into the physical process of gully erosion.

Several factors such as the rainfall characteristics, soil properties, topographic features, land use, and management are responsible to EG formation and development (Daggupati et al., 2014; National Research Council, 1986). Higher rainfall intensities result in high surface runoff volume and more erosive power in surface runoff, which increases the potential for gully erosion. Soil erodibility factor is one the main factors that controls the sediment yield, and erodibility factor is mainly controlled by the soil properties. The direction of the runoff, the volume of flow accumulation and points of flow conversion are directed by the topographic land scale features. Crop type, root structure, vegetation density, soil cover, and tillage practices are determined by land use and management practices. The land use management practices change the soil properties runoff characteristics and topographic features of the land. Formation or development of EGs can be controlled by applying best management practices.

Soil erosion caused by water in the agricultural field is a dynamic and complicated process. Techniques ranging from simple methods of measuring the gully cross-sectional using a ruler to complex approaches such as photogrammetry techniques can be used to assess the EG erosion in the field. Stereoscopic photogrammetry, high accuracy GPS, laser scanning are commonly used techniques to measure EGs (Wells et al., 2016). Repeat topographic surveys are essential to identify the EG development process, the behavior of the EG and tracking the soil erosion(Gillan et al., 2017). Smith (1993) used Gulliometer to track the dynamic changes of EGs over two years period from 1983 to 1985 and was able to calculate total soil loss in the gully. However, the method was not capable enough to apply frequently to identify dynamic changes in the gully development process. Pineux et al. (2017) applied photogrammetry technique to produce DEM time series over two years to quantify diffuse erosion in an agricultural watershed and identified erosion/deposition pattern, tendency along the slope from erosion to deposition. The accuracy of the method was 0.05ft and was able to calculate annual soil loss in the watershed. Daba, Rieger, and Strauss (2003) assessed gully dynamics and volume changes over 40 years of the period using photogrammetry. The photogrammetry models were built using historical Arial photographs taken in 1966 and 1996. Brasington and Smart (2003) used close-range digital photogrammetry to evaluate sedimentation pattern and sediment rate over a simulated landscape. The comparison of sediment budget over the simulation and the total soil loss calculated using the photogrammetry method had small 6.2% difference. Campo-Bescos et al. (2013) used photogrammetry models to understand gully headcut growth process and calibrated gully headcut retreat models. All these studies used a series of surveys to generate time series of elevation profile of the gullies. However, the spatial resolution and temporal resolution were limited by the surveying techniques used in each study and still needs to improve the gully survey techniques to monitor the dynamics of EG development. Gillan et al. (2017) identified, close-range photogrammetry as a suitable method to track dynamic changes of the EGs, due to its lower-cost, higher accuracy, higher spatial, and temporal resolution.

Photogrammetry can be categorized into aerial photogrammetry and terrestrial (or close-range) photogrammetry. In aerial photogrammetry, the camera is mounted in airborne platforms like an aircraft or a drone and pointed vertically downward towards the ground. In close-range photogrammetry, the camera is mounted into the ground-based platform like a tripod, frame, or it is handheld. Compared to the aerial photogrammetry, close-range photogrammetry has high spatial resolution and able to identify gully changes up to 1cm. Chapter 3 described a developed method of close-range photogrammetry and its accuracy.

This chapter describes how the photogrammetry method can be used to monitor the EGs, and introduces the techniques to calculate width, depth, area, and headcut advancement of the three EGs using photogrammetry surveys. This chapter also describes the patterns of soil losses during different growing seasons and identifies the contributed factors.

4.2 Materials and Methods

Study area

Topographic index models can be used to successfully predict the location of EGs (Daggupati and Sheshukov, 2013). Initially, topographic index models were used to identify potential fields for collecting EG data, and land use/land cover, and digital elevation datasets in Riley and McPherson counties were used to select crop fields that contained EGs and were in no-till. With the assistance of NRCS office in Manhattan, county extension agents, and after communicating with individual farmers, one no-till field at Pillsbury crossing near School Creek in Riley County, Kansas was selected for field measurements. The field had several EGs that were visible during in-person visits. Three gullies were selected for detailed soil loss monitoring. All catchments of gullies were embedded within the field, which eliminated external inflows into the catchment with unknown runoff characteristics. A tipping bucket type rain gauge and a flow meter were installed in the field to measure rainfall rates continuously.

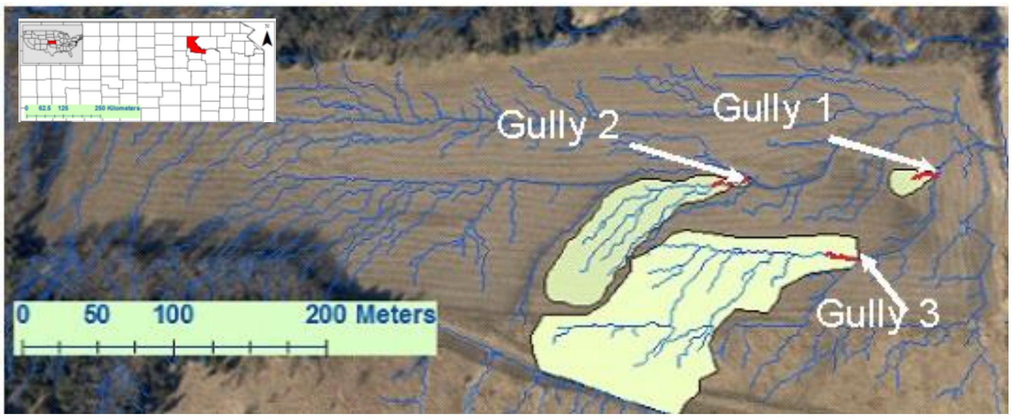

Figure 4-1: Location of the field, subjected ephemeral gullies and drainage area

Table 4-1: Characteristic of the field

Area	93,600 m^2
Average slope	1.5^0
Min elevation	330.13 m
Max elevation	346.19 m
Crop	Grain Sorghum/ Soybean
Management	No-till
Soil type	Silt-clay loam

Table 4-2: Length, average slope and drainage area of gullies

	Gully 1	Gully 2	Gully 3
Drainage area (m^2)	390	4270	12700
Length of the longest flow path (m)	33	140	242
Average slope of the longest flow path (Degrees)	0.5	0.5	0.7

Weather Data

An on-site weather station was established for rainfall data collection. The weather data were collected from July 2016 to May 2018. The weather station contained tipping bucket rain gauge with the characteristics presented in Table 4-3. The data was collected at one-minute interval and aggregated to 30-minute intervals.

Table 4-3: Features of the rain gauge and the data logger

Maximum rainfall rate	12.7 cm per hour
Calibration accuracy	±1.0% (20 mm/hour)
Resolution	0.2 mm
Operating temperature range	0° to +50°C
Storage temperature range	-20° to +70°C
Tipping bucket mechanism	Stainless steel shaft with brass bearings
Time stamp	Resolution 1.0 second
Time accuracy	± 1 minute per month at 25°C

Figure 4-2: Rain gauge and data logger

4.3 Field Survey

Close-range digital photogrammetry is known to provide adequate estimates of soil losses for EG evaluation (Wells et al., 2016; Castillo et al., 2012). Therefore, in this study, close-range digital photogrammetry was used to evaluate the three selected gullies. The summarized field survey process is illustrated in Figure 4-3.

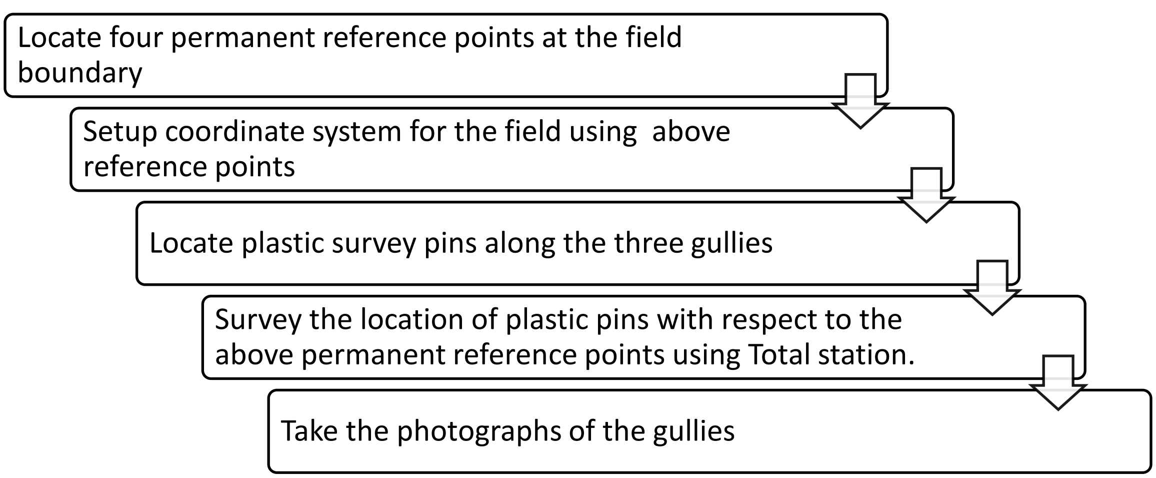

Figure 4-3: Field survey process

It is required to reference the photogrammetry model using geo-referenced locations. This process is called geo-referencing. To compare each Digital Elevation Model (DEM) obtained by periodical surveys, each of those DEMs is required to be projected to the same coordinate system. Since there was no any National Geodetic Survey (NGS) benchmarks near the field, it was difficult to use a widely available coordinate system to the field surveys. Therefore, the local coordinate system was created for the studied field.

Initially, four permanent reference points were built in the East, West and South boundaries of the field. Then the coordinate of the south reference point was taken as (1000, 1000, 1000) and the other three permanent reference points were surveyed with respect to the initial location. Later these three points were used to ensure the accuracy of the coordinate system, total station functionality, and stability of the permanent reference points. The reference points within the gully were surveyed with respect to those permanent reference points.

Figure 4-4: Reference point within the gully

The density of the georeference points affects the accuracy of the model (Agüera et al., 2017). According to the recommendation of the accuracy test described in Chapter 3, four reference points were used to cover one square meter of the area of the gully. All pins were randomly located along the gully banks with the four points per square meter density.

Before each photogrammetry survey, coordinates of all plastic pins correspond to the local coordinate system were surveyed using the total station. The accuracy of the total station is 1.5 mm at 50m distance(“Zoom40 Series | GeoMax”). Technical data of the total station are shown in **Table 4-4**

Table 4-4: Technical data GeoMax Zoom 400 total station

Angle measurement Accuracy	7”
Compensation	Angular compensation
Reach	3500m
Accuracy	Accurate + mode: 1.5 mm + 2.0 ppm, Accurate fast mode: 3.0 mm + 2.0 ppm, Tracking: 3.0 mm + 2.0 ppm
Standard measuring time	1.0 s
Laser spot size	At 30 m: 7 x 10 mm; At 50 m: 8 x 20 mm
Operating temperature	-20 °C to +50 °C

Sony a7r camera was used to take photographs. The camera has a full-frame CMOS sensor which has a 36.3-megapixel resolution. To take the photographs, the 50mm prime lens was attached to the camera. To hold the camera custom made Aluminum frame was used. The whole setup used to take photographs is shown in Figure 4-6.

Figure 4-5: Surveying ground control points using the station survey

Figure 4-6: Camera setup and ground coverage area

After setting up the camera lens and the frame to take photographs, the camera was located 2m above the ground in such a way that the sensor surface was maintained parallel to the earth surface. The area of image coverage was calculated by using the angle of the view of the lens and the distance between the camera and the object (Equation 2-3) as 1.5m x 0.96m surface area in a single exposure. To survey the entire gully, the operator walked along the gully and took photographs with more than 60% forward overlap and more than 60% side overlap. The overlaps provided sufficient photograph density to build accurate photogrammetry models (Dai, Fei Lu, 2012).

4.4 Create 3-D surface model

Photomodeler scanner software was used to create the 3-D surface of the gully, and the process is summarized in Figure 4-7. All of the steps were described in Chapter 3 under the topic 'Camera calibration and building the 3-D model'.

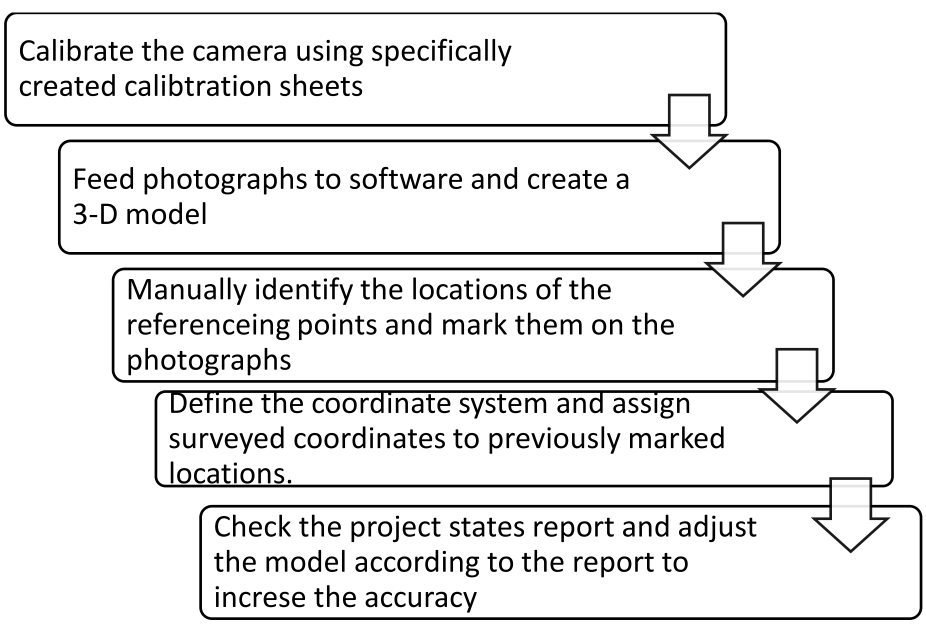

Figure 4-7: 3-D model building process

4.5 DEM Processing

To analyze the gully surface, created 3-D point cloud must be imported to the GIS environment and the GIS process is summarized in the following chart (Figure 4-8).

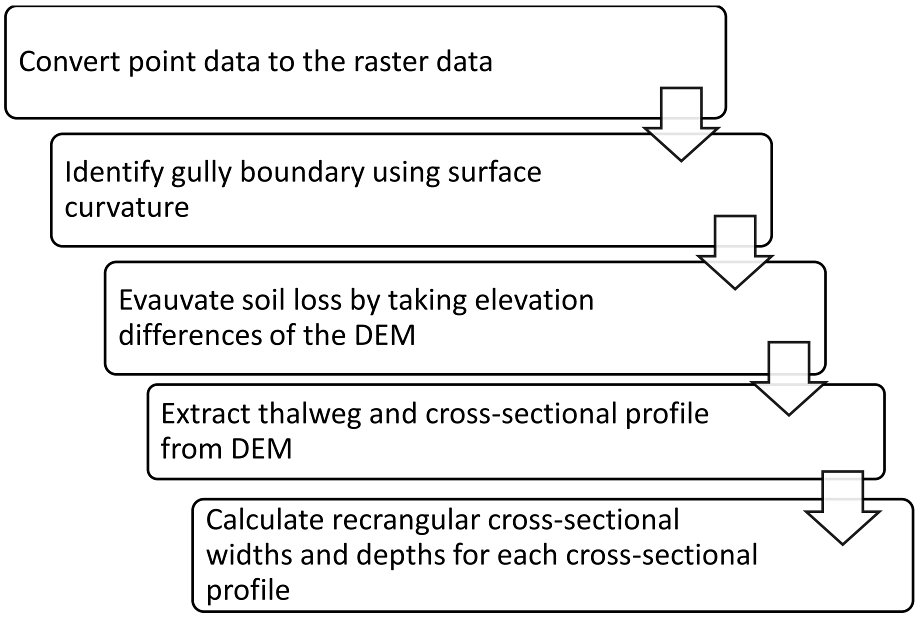

Figure 4-8: Summarized DEM processing steps

Convert point data to the raster data

Analysis of the 3-D point cloud was done using ESRI's ArcMap. First, the point cloud was imported to the ArcMap as point file and plot those points in the map using point to raster tool; those points were converted into the raster. Resolution of the raster was selected as 1cm and mean elevation of all points within the 1cm square was selected as the elevation of that raster cell. Since the conversion process uses the mean value of all points within the 1cm square, the points beneath the visible surface were neglected, and the undercut of the gully was removed (Figure 4-9). However, it is mandatory to remove all points that correspond to leaves and surface residue before following this step.

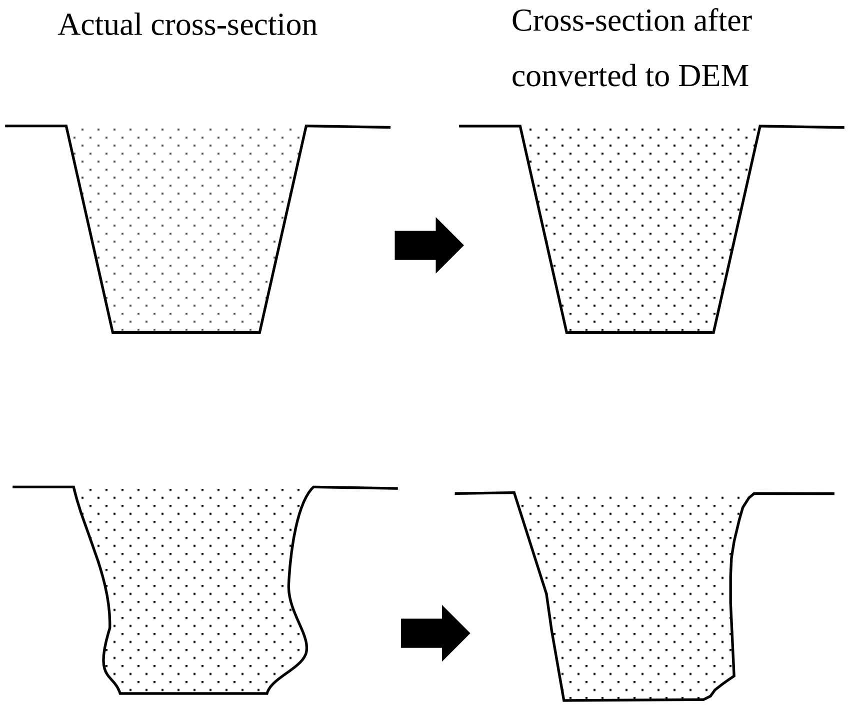

Figure 4-9: Point to raster conversion (process removes the undercut data)

Identify gully boundary

The created DEM includes gully area as well as parts of drainage areas. It is required to delineate the gully boundaries to assess elevation changes within the gully that relate to soil erosion and sediment accumulation. Gully boundary identification is challenging. In this project, profile curvature of the surface was used to identify the boundaries. The profile curvature can be defined as the second derivative of the surface parallel to the slope, and it indicates the maximum direction of the slope. For the downward convex surfaces profile curvature is negative and for the upward concave surfaces profile curvature is positive. For linear surfaces, profile curvature is zero; refer to Figure 4-10 and ArcGIS toolbox ("Curvature Function—Help | ArcGIS for Desktop").

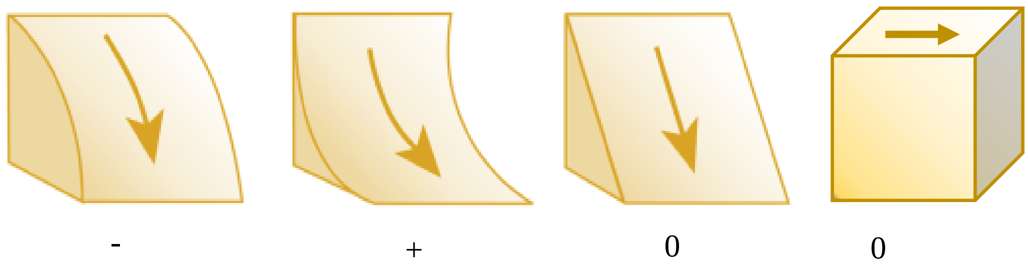

Figure 4-10: Sketch of different slopes and signs of the corresponding profile curvature

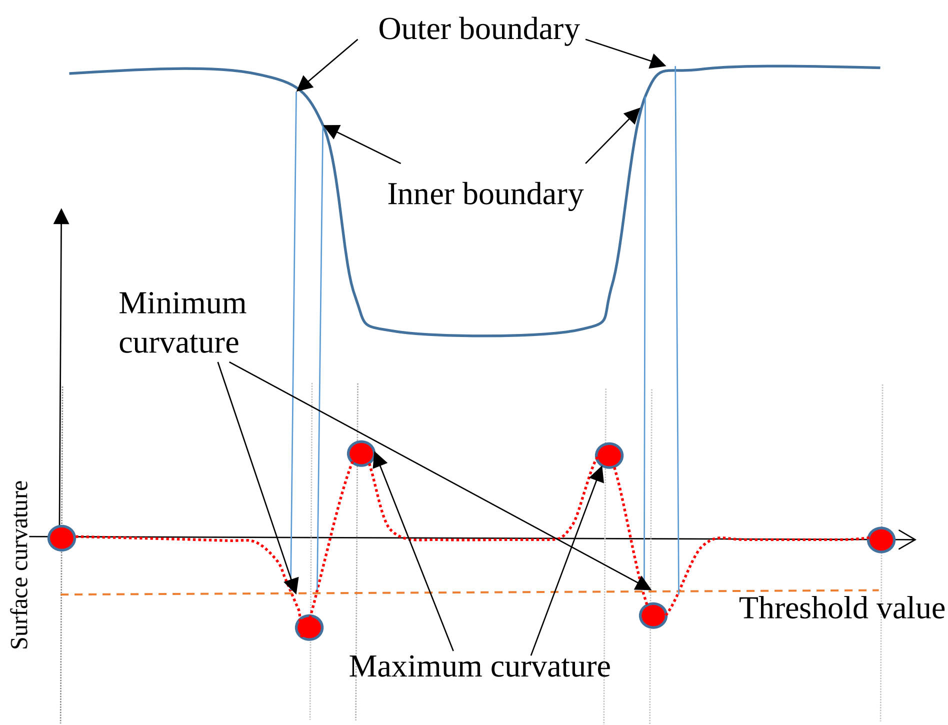

Figure 4-11: Profile curvature along the gully cross-section

The profile surface curvature graph along the gully cross-section is sketched in Figure 4-11. In actual DEM, the surface curvature curve is not as smooth as the above graph, but capable to identify the sudden morphological changes in the gully surface. The gully boundary delineation process can be described as follows:

- Obtain profile curvature raster using DEM.
- Mark cross-sections apart form 0.5m each other.
- Plot surface curvature graphs along each cross-section.
- By considering all the surface curvature graphs, determine a suitable threshold curvature value to identify the gully boundary.
- Separate the points which were lower than the threshold profile curvature value.
- Above step marks boundary around the gully and the width of the boundary line would be 5cm to 10 cm.
- The developed model required rectangular gully cross-section. To minimize the effect to gully cross-sectional area when it converts to the rectangular cross-section, the inner edge of the boundary line was considered as the gully boundary.
- If there were no any significant curvature fluctuations along the gully cross-sections, contour lines were also used to delineate the gully boundaries.

The process above generates the outline of the gully boundary with all tributaries. For modeling purposes, separate boundaries were created by removing all tributaries. The ArcMap model was developed to automate gully boundary identification. Figure 4-12 shows the main steps of gully boundary delineation process.

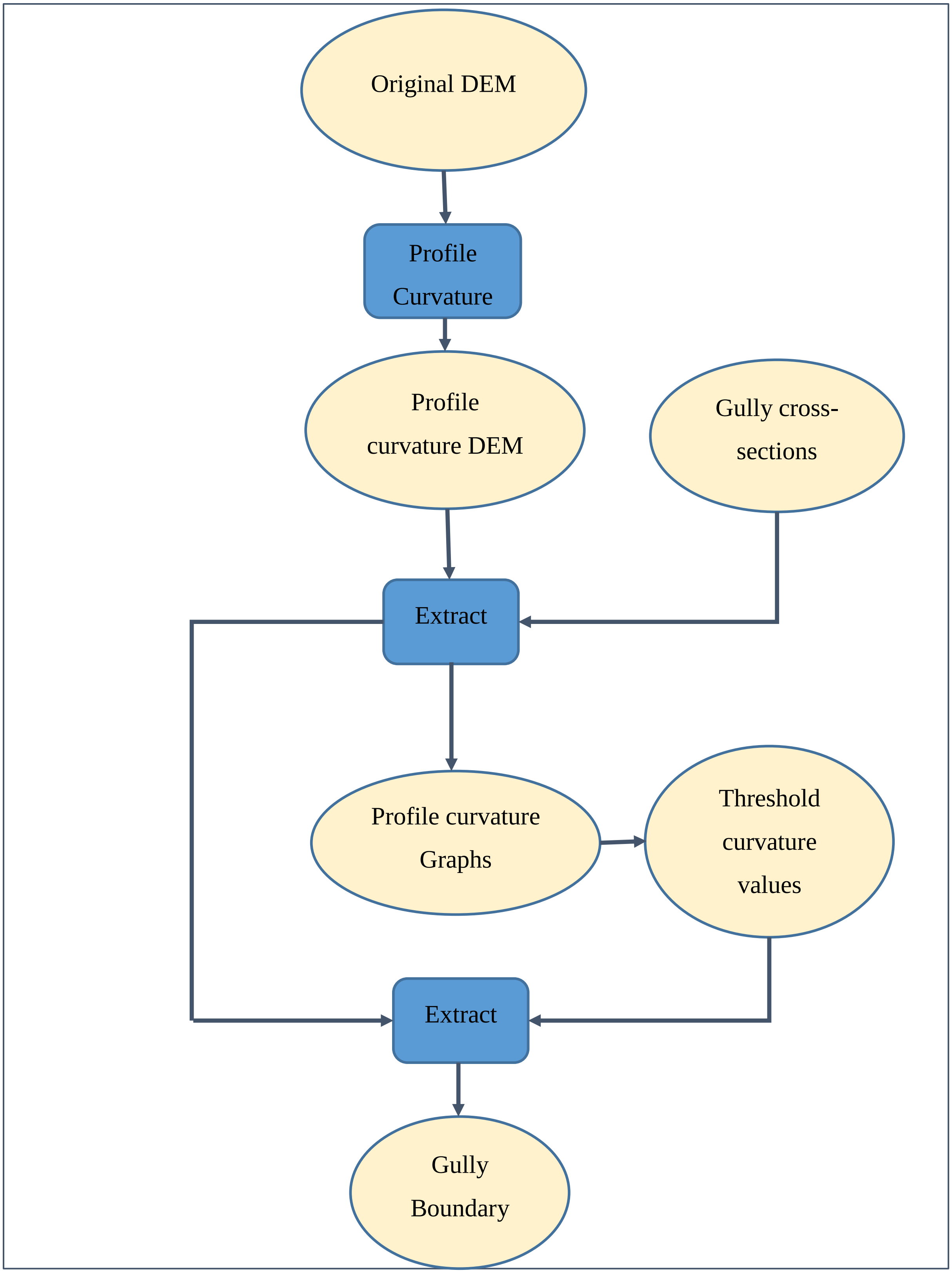

Figure 4-12: Gully boundary delineation process

Evaluate soil loss

Gully boundary may shift between two surveys. For evaluation of the changes in gully surface elevation, a common gully boundary was found with ArcGIS. Then the DEM corresponding to the beginning of the period and the DEM corresponding to end of the period were clipped using the common boundary. The difference in surface elevation between two surveys was obtained by subtracting two DEMs. In the resulted raster file, positive values indicated soil losses and negative values indicated soil deposition. Figure 4-13 shows the procedures used to calculate the change in soil elevation and the Python code of the ArcGIS model is presented in Appendix-I.

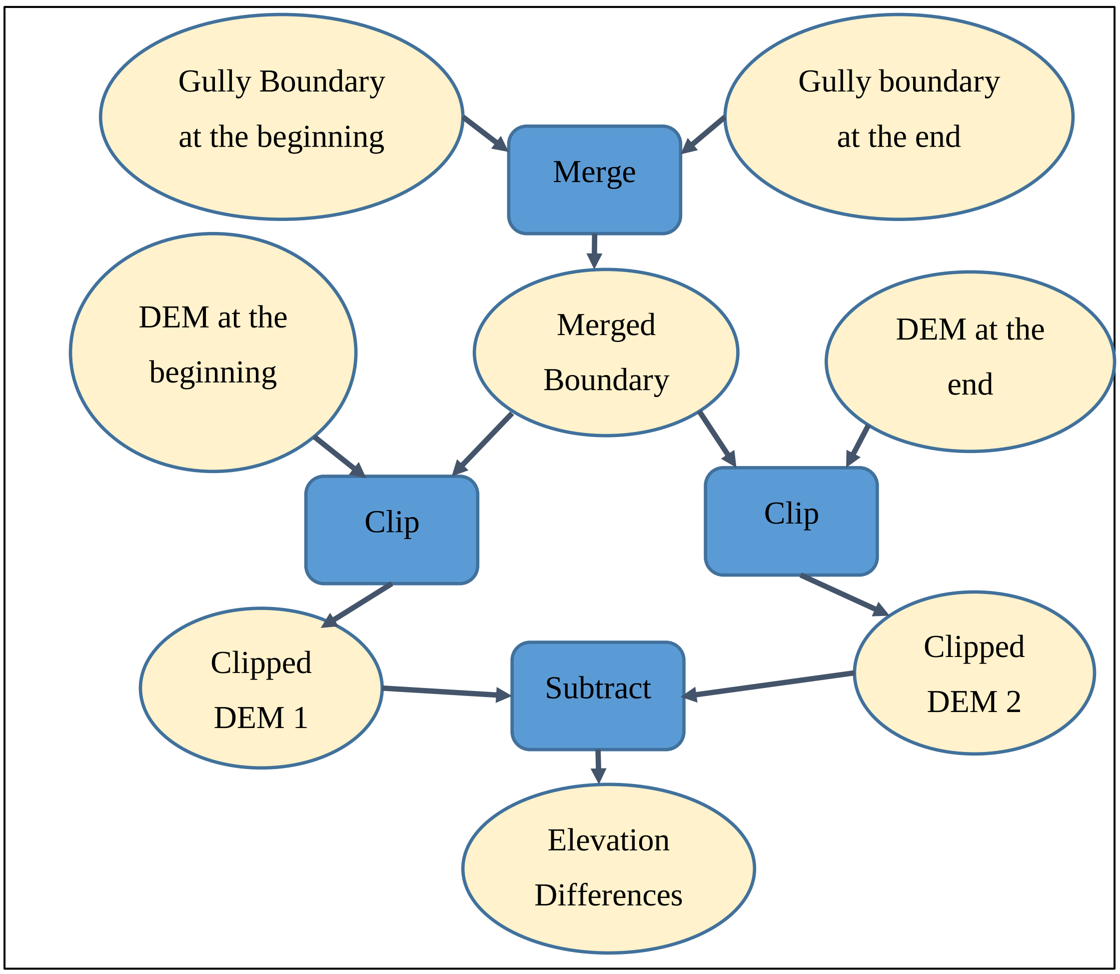

Figure 4-13: Soil loss calculation process

Extraction of thalweg and cross-sectional profile from the DEM

The profile of lowest elevation along the gully is considered as the thalweg. Thalweg changes from time to time. The ‘river bathymetry’ toolset was used to identify the thalweg and created cross-sections (McKean et al., 2009). The toolset was applied to all surveys and a common thalweg was selected. From the headcut to the bottom of the gully, cross-sections were selected in such a way that two consecutive cross-sections were 0.5 m apart and perpendicular to the common thalweg. For each cross-section, elevation along the cross-section was extracted and used to calculate the gully width and depth.

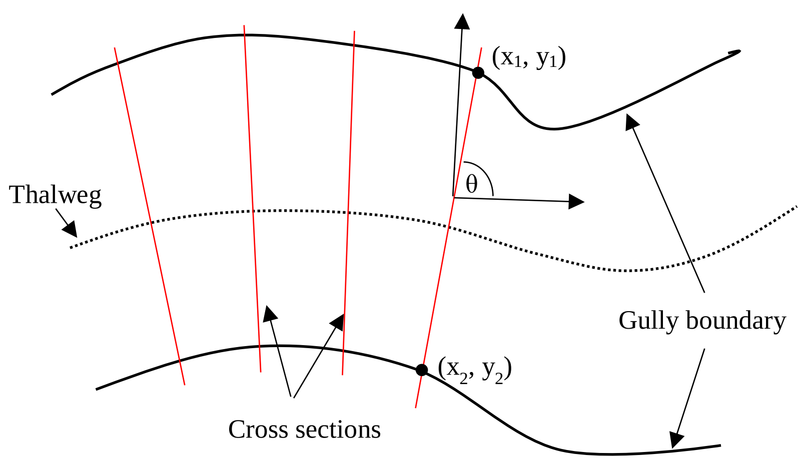

Figure 4-14: Gully boundary, thalweg and cross sections

Gully depth, width and area calculation

Elevation data along the gully cross-sections were used to determine the depth and width of the gully. Usually, gully banks are not at the same height. For this study, three different types of depths were calculated. Bankfull depth, minimum depth, and average depth. The elevation difference between thalweg and the highest bank was considered as the bankfull depth, elevation difference between thalweg and the lowest bank was considered as the minimum depth; the average of those two depths was considered as the average depth. Gully width was calculated for each type of depth. For the left boundary A (x_1, y_1) and right boundary B (x_2, y_2) the width of the gully is given by,

$$width = \sqrt{(x_1 - x_2)^2 + (y_1 - y_2)^2} \qquad (4\text{-}1)$$

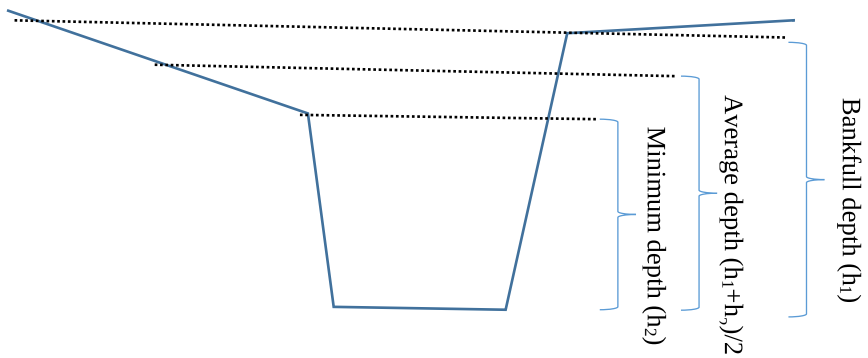

Figure 4-15: Gully depth

For each cross-sectional profile, the cross-sectional area is generally calculated as

$$Area = \int_{x_1}^{x_2} f(x)\, dx \qquad (4.2)$$

Where $f(x)$ is the function which represents the surface profile. However, for this study cross-sectional area was calculated by taking summation of the areas of rectangular stripes:

$$Total\ area = \sum_{i=1}^{n} a_i \qquad (4\text{-}3)$$

Where, a_i is the area of a rectangular stripe. The width (d) of each rectangle is in $1cm \leq d \leq \sqrt{2}cm$ and depends on the angle (θ) between the cross-sectional plane and the *x*-axis.

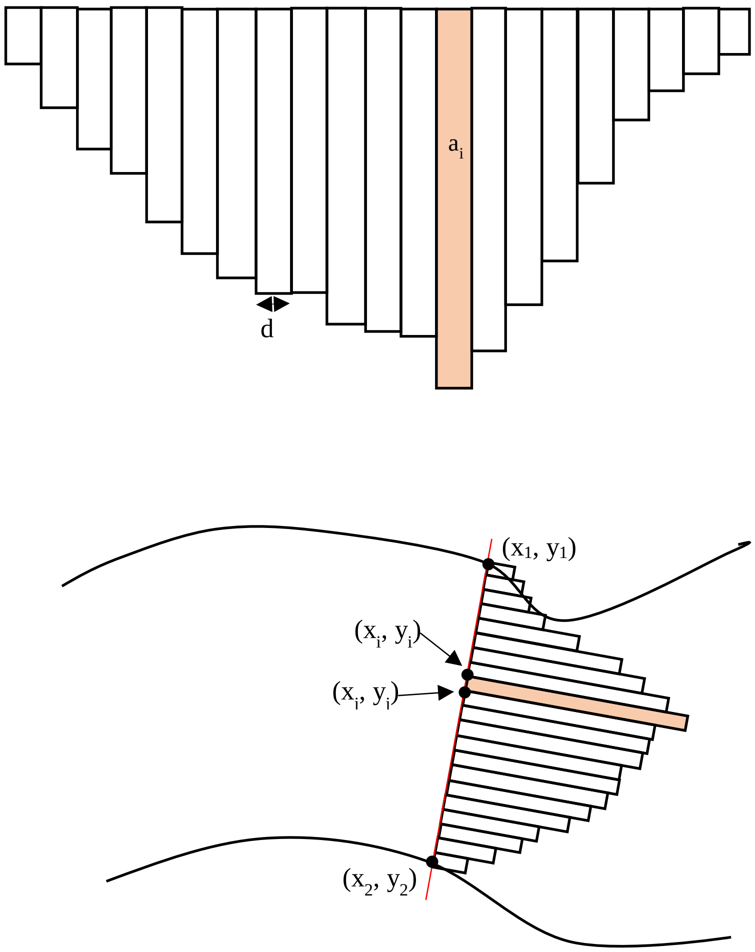

$$d = \sqrt{(x_i - x_j)^2 + (y_i - y_j)^2}$$

Figure 4-16: Gully cross-sectional area calculation

Calculation of the rectangular width and depth

Channel erosion models can be applied only to the rectangular channels. Two types of rectangular cross-sections were calculated.

I. By preserving the actual cross-sectional area and depth,

$$Rectangular\ width = \frac{Actual\ area}{Actual\ depth} \tag{4-4}$$

II. By preserving the actual cross-sectional area and width,

$$Rectangular\ depth\ = \frac{Actual\ area}{Actual\ width} \tag{4-5}$$

The Matlab code developed to calculate gully width, depth and cross-sectional area is presented in Appendix-J.

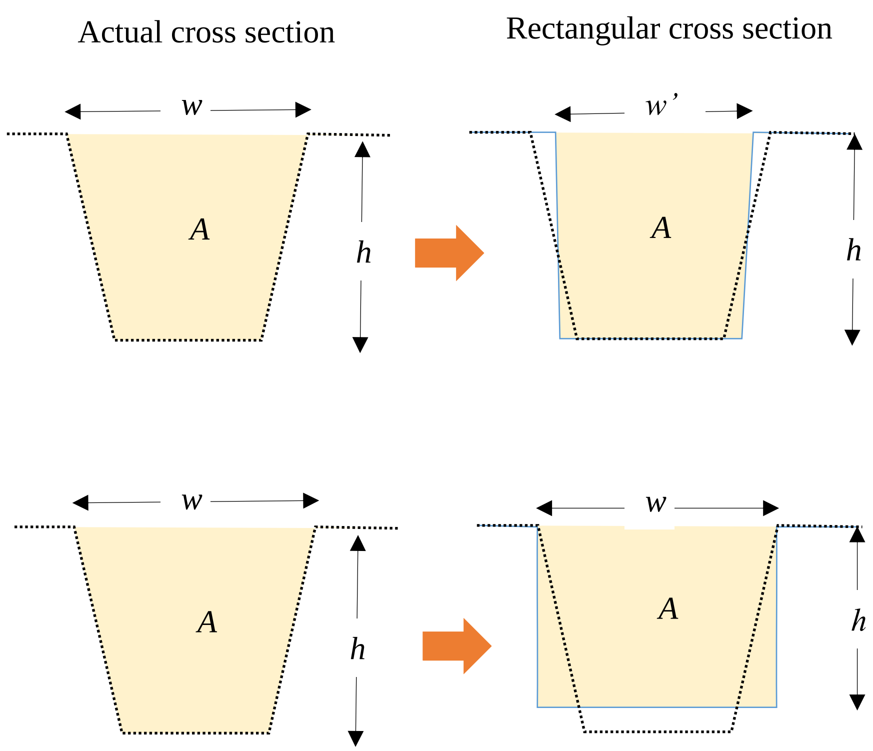

Figure 4-17: Rectangular width and depth

4.6 Results

Weather data

Changes in EG depend on the characteristics of rainfall events, soil conditions, land cover vegetation, and other factors (Foster et al., 1982). The on-site weather station was used to measure precipitation and air temperature from June 15, 2016, to March 20, 2018. The time series of precipitation and air temperature are presented in Figure 4-18. Survey days are marked by dotted black lines.

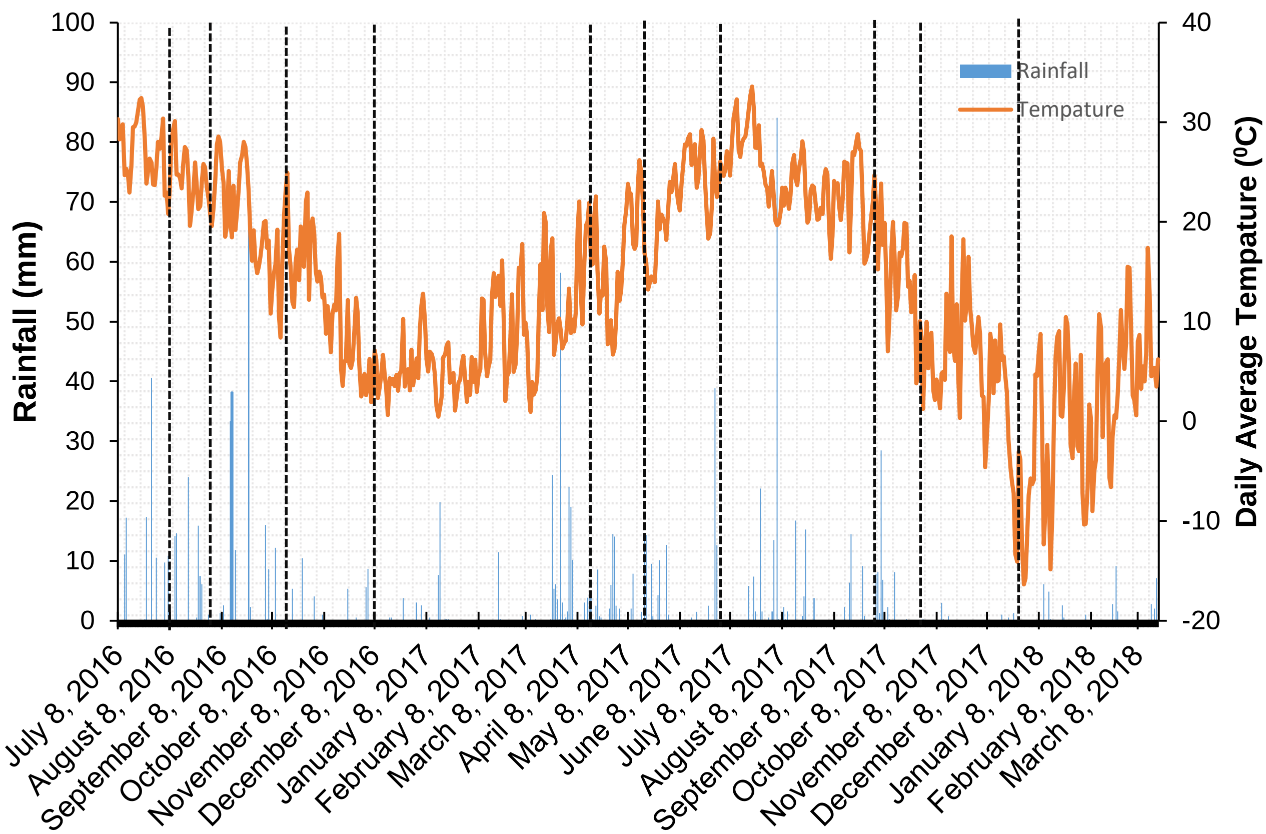

Figure 4-18: Average daily temperature and daily precipitation

During the study period (613 days), there were 151 wet days, and the total precipitation was 1153 mm. The highest rainfall event was recorded on August 5, 2017 as 84.08 mm. The detailed precipitation information is shown in Table 4-5.

Table 4-5: Number of Rainfall events, total precipitation, and maximum precipitation

	Survey Period	Survey Date	Number of Wet Days	Number of days	Maximum Daily Precipitation (mm)	Total Precipitation (mm)
1	07/15/2016-08/08/2016	8/8/2016	6	24	40.59	89.35
2	08/08/2016-09/02/2016	9/2/2016	8	25	24.01	83.72
3	09/02/2016-10/13/2016	10/13/2016	11	41	74.41	200.81
4	10/13/2016-12/08/2016	12/8/2016	8	56	10.41	40.87
5	12/08/2016-04/19/2017	4/19/2017	36	132	58.16	226.42
6	04/19/2017-05/13/2017	5/13/2017	11	24	14.5	60.69
7	05/13/2017-07/05/2017	7/5/2017	15	53	38.84	124.24
8	07/05/2017-10/02/2017	10/2/2017	23	89	84.08	215.81
9	10/02/2017-11/03/2017	11/3/2017	10	32	28.45	63.71
10	11/03/2017-12/16/2017	12/16/2017	3	43	3	4
11	12/16/2017-03/20/2018	03/20/2018	20	94	9.14	43.43

Each survey period contained at least one wet-day. Based on the number of wet days survey period from (12/08/2016-04/19/2017) showed the highest number of wet days and the highest total precipitation was 226 mm. In the first survey period, there were 6 wet days with a total of 89.35mm precipitation. During that period, grain sorghum was in the early stage of the growing and soil barely covered by the canopy. In the second survey period of 25 days, 8 days were wet days, and the field received 83.72mm of total precipitation with 24.01mm maximum daily precipitation. From September 2 to October 13, 2016 the field had the highest total precipitation (200.81 mm) for Grain sorghum growing season. However, this time the plants were at the matured stage and dense canopy cover protected soil from the direct impact of rain. In the fourth survey period, the field received 40.87 mm of precipitation in 8 wet days. In this period the crop was harvested. However, the harvesting process spread plant residue all over the field and soil was barely open to the direct precipitation. From December 2016 to April 2017 total precipitation was 226.42mm in 36 wet days. In this period the average daily temperature was close to 0 ^{0}C. There was no vegetation in the field; however, remaining residue of the Sorghum plants was in the field. From April 19 to May 13, 2018 there were 11 wet days, and total precipitation was 60.69 mm. Seventh survey period from May 13, 2017-July 05, 2017 the field received 124.24 mm of rainfall in 15 wet days. The soil was barely covered by the vegetation. At the end of this period, soybeans were planted; at that time there was no any significant soil cover. From June 5, 2017 to October 5, 2017 within 89 days, 215.81mm of rainfall occurred, and there were 23 wet days. The growing season of soybeans received less precipitation (215mm) in 2017 than the one for sorghum (360 mm) in 2016. In the eighth survey period another survey was conducted on August 23, 2017. However, the canopy cover limited the visibility of the EG surface, and the survey was neglected. In the ninth survey period, the precipitation was 63.71 mm; the plants were at the matured stage, and most of the leaves felt and laid down on the soil surface. End of this survey period, Soybean was harvested. From November 3 to December 16, the average daily temperature was at the subzero level, and precipitation was deficient. The last survey period occurred from December 2017 to March 2018, and the field was in dry condition; total precipitation was 43.43mm in 20 wet days.

Digital Elevation Models

For each gully, DEMs were created using point cloud obtained from corresponding photogrammetry surveys. The changes of EGs over the study period were obtained by taking elevation differences of DEMs created at the beginning and end of the study period. The ground resolution of each DEM was 1cm. DEMs were used to calculate headcut movement, channel width cross-sectional area, and thalweg. Raster map created for all gullies and all surveys are presented in Figure 4-19 (Gully 1), Appendix-C (Gully 2) and Appendix-D (Gully 3).

DEMs provide detailed information of gully development process over the observation period. DEM dated 07/15/2016 (top left corner) corresponds to the beginning of the study and the DEM dated 03/20/2018 corresponds to the end of the field study. From July 2016 to April 2017, Gully 1 showed substantial advancement and soil erosion. After April 2017 Gully 1 started to obliterate. However, for the entire period Gully 1 showed widening and headcut movement. Comparison of two DEMs gives width, depth, elevation, and headcut change in-between those survey periods; all of these changes are discussed later in this chapter.

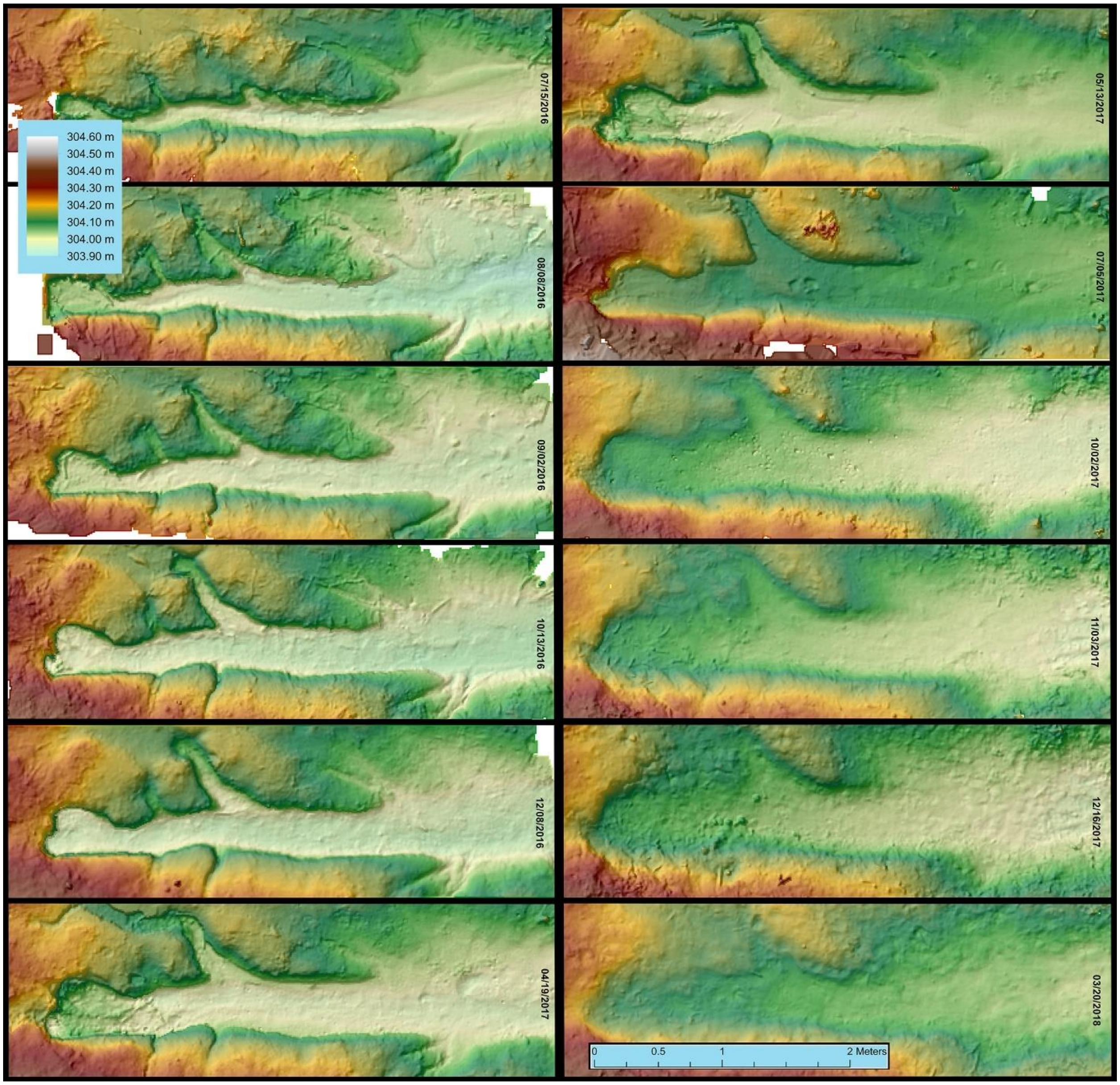

Figure 4-19: DEM of Gully 1

Surface area

The surface curvature-based method was used to identify gully boundaries. For each survey, two types of gully boundaries were defined. Main (called normal) gully boundary contains only the main channel of the gully, and extended gully boundary contains the main channel and all other tributaries. Using those boundaries gully surface area was defined for three gullies.

Percentage expansion with respect to the initial surface area was used, to compare the expansion of the gullies, and the percentage expansion of three gullies is shown in Figure 4-20.

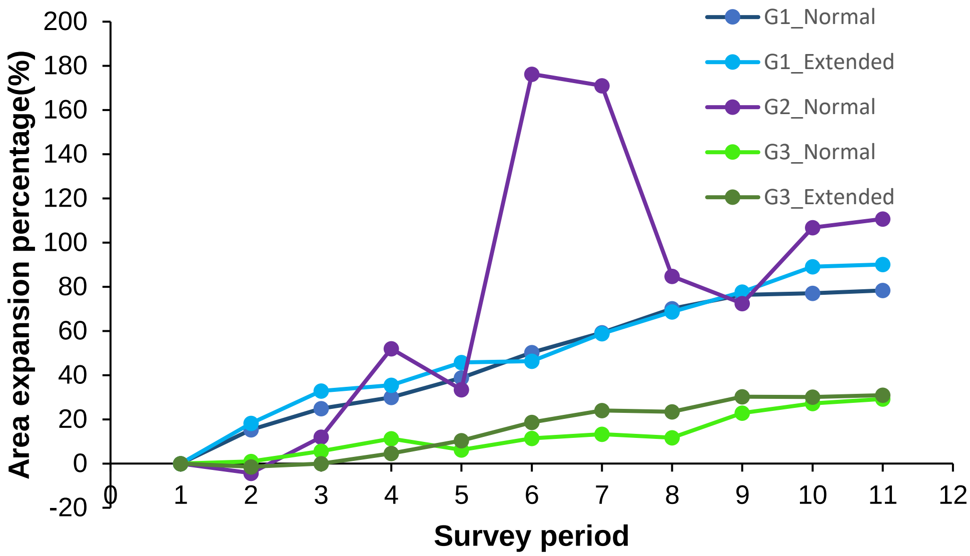

Figure 4-20: Gully surface area expansion percentage with respect to the initial gully surface area. Two types of gully boundaries were used; boundary of the main channel (normal), and boundary of main channel and tributaries (extended)

Three gullies have expanded over time (Figure 4-20). The three gullies have three different expansion rates; the Gully 3 shows the minimum expansion rate (28% in 20 months) compared to the other two gullies. Surface expansion of the second gully has more fluctuations. From December, 2016 to May, 2017 the surface area increased by 180%. From July, 2016 to March, 2018 normal surface area of the first gully increased by 78% and extended surface area expanded by 90%. Expansion of the Gully 2 was 110% and the normal surface area and extended surface area of the Gully 3 expanded by 20%, 30% respectively.

Headcut Movement

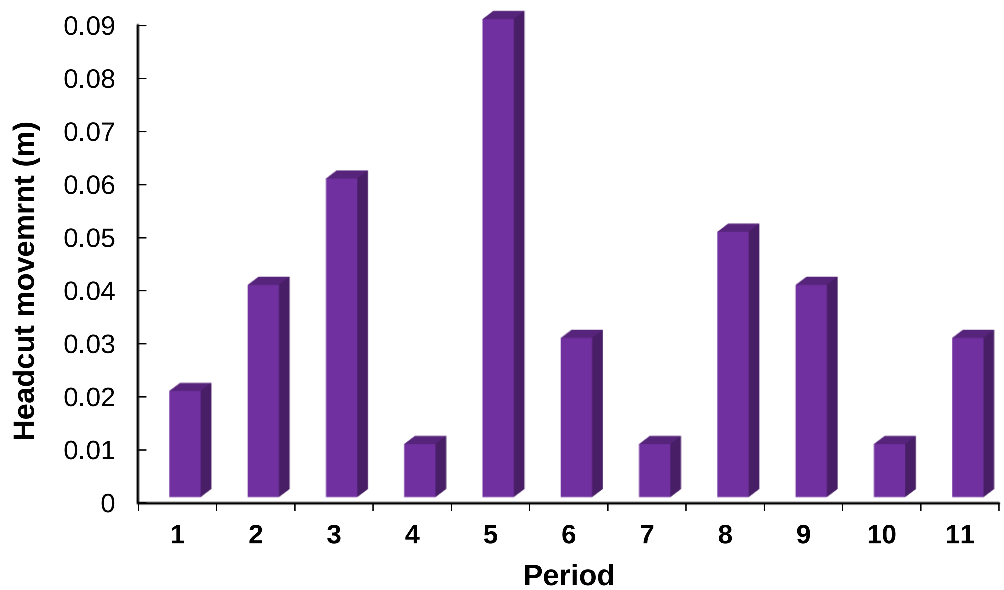

Figure 4-21: Gilly 1, headcut movement over time

There was no clear headcut movement for the second and third gullies. However, the first gully shows a clear headcut movement. From December, 2016 to April, 2017 headcut moves 9 cm, and it is the greatest value recorded in the observed period (Figure 4-21). In the early growing season of 2016 and 2017 significant headcut movements were occurred with a value close to 6cm. For all survey periods, the headcut moved by 39 cm.

Gully widening and deepening along the cross-section

The behavior of Gullies 2 and 3 are close to the behavior exhibited by smaller rills There was no clear head cut. The behavior of Gully 1 exhibited the characteristics that correspond to the behavior of the EG There was a clear headcut and gully was expanded by moving headcut towards the upstream. Figure 4-22 shows cross-sectional changes near the headcut area of the Gully 1. From July 2016 to March 2018 cross-sectional profiles show expansion of gully width. For all 20-

month study period, the width of the cross-section increased by 16cm (Figure 4-22). The depth of the gully fluctuated in both positive and negative directions. This variation mainly controlled by the intensity of the rainfall. Low intensive rainfall events accumulate sediment close to the head cut area, and highly intensive rainfall events flush down that sediment.

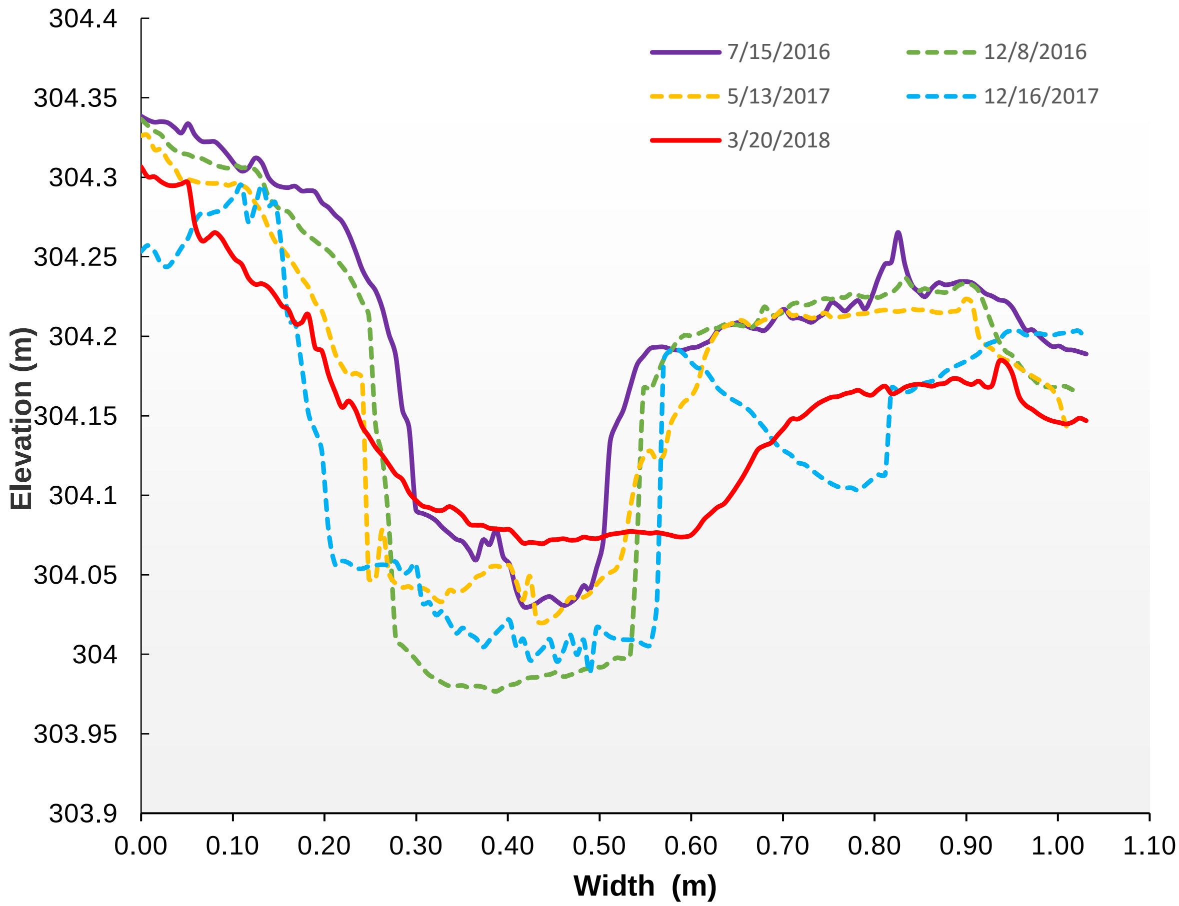

Figure 4-22: Cross section close to headcut in Gully 1

Thalweg

Figure 4-23 shows the elevation changes along the thalweg. The sediment deposits in the gully bed and elevation of the thalweg increases, when the runoff does not have enough power to carry out the sediment. From the end of the growing season to early Spring, elevation of the thalweg increased. For each survey period, gully surface area increased continuously.

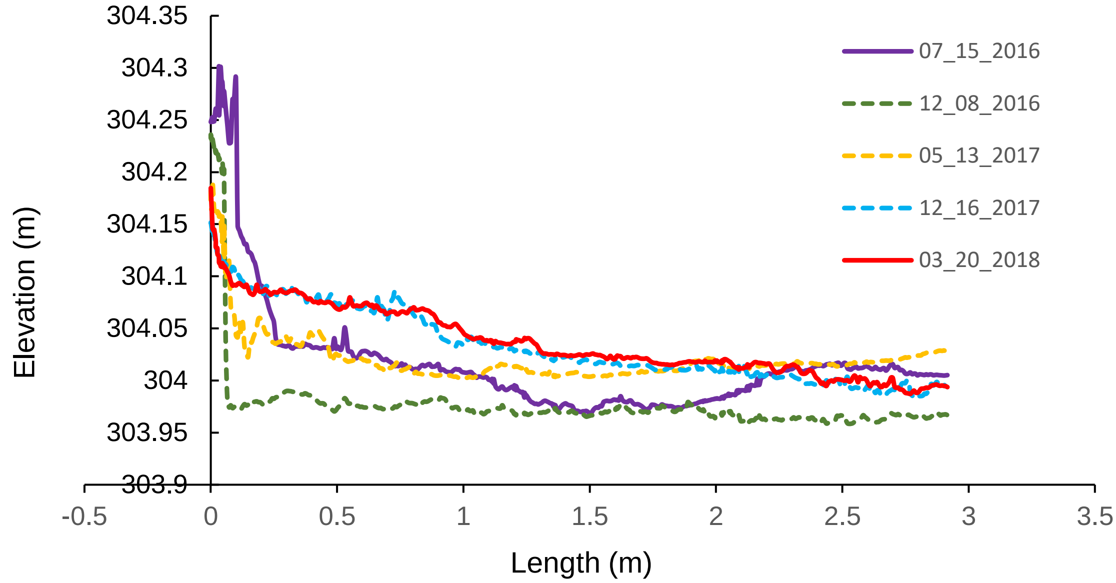

Figure 4-23: Gully 1 thalweg

Soil Erosion and Accumulation between Surveys

The elevation differences between two DEMs can be obtained by subtracting the latest DEM from the earliest DEM. The positive values indicate the elevation loss and negative values indicate the elevation gain. Multiplication of total elevation changes and the subjected area gives the total soil volume change of the subjected area. General DEM includes gully surface area as well as the outside area of the gully. Therefore, the surface curvature-based method was used to identify the gully boundary. However, the gully boundaries change with time. Therefore, the area bounded by the union of the two boundaries corresponds to two surveys was considered for calculating the soil loss between the two surveys. The elevation changes in between surveys are presented in Figure 4-24, Appendix-E and Appendix-F.

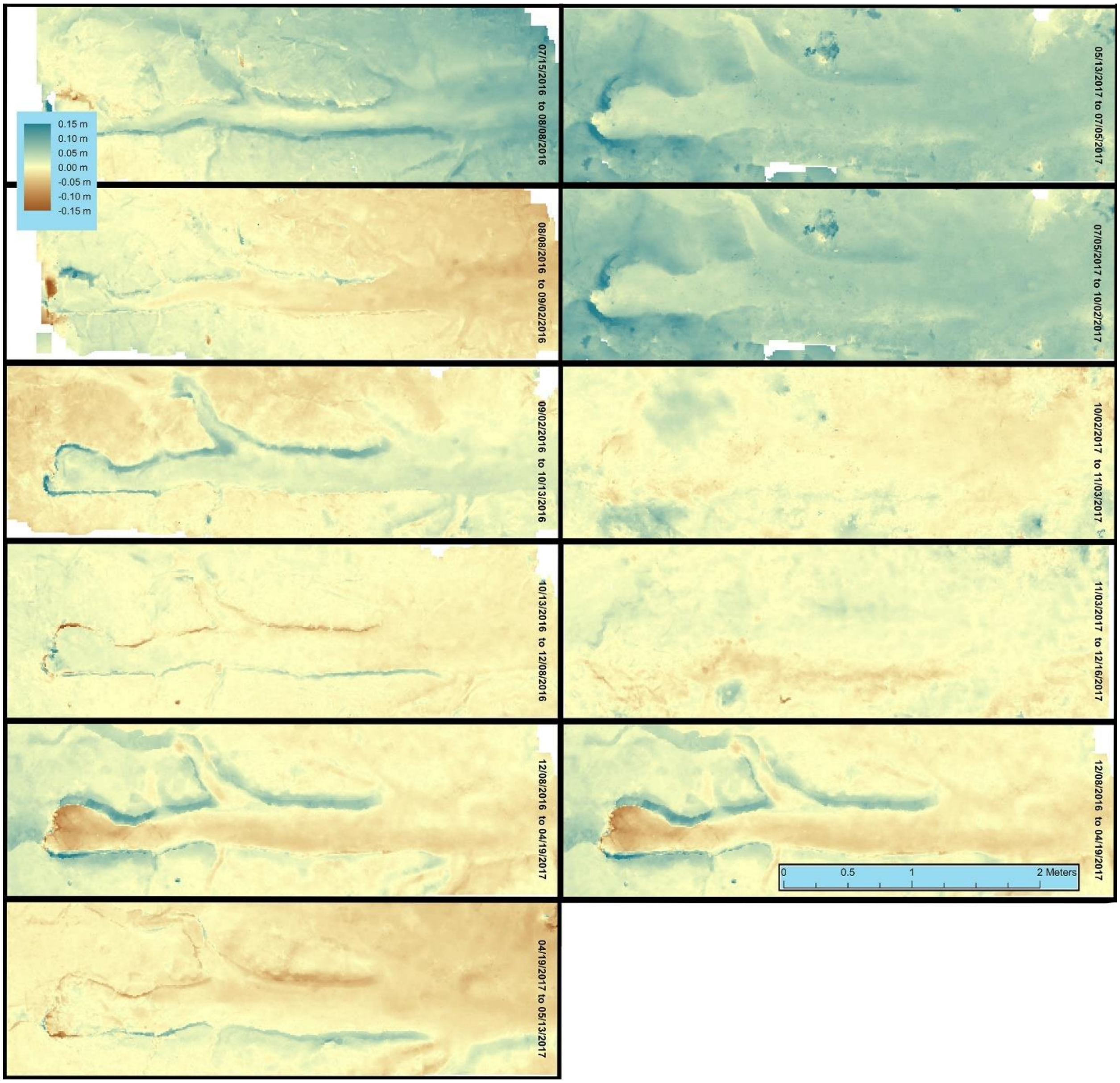

Figure 4-24: Soil loss/gain in-between surveys

The area of soil loss is represented by yellow to blue color range, and soil accumulations are represented in yellow to red range. Yellow represents the negligible elevation (-0.05 - +0.05 cm) changes.

Table 4-6: Soil loss of three gullies by the two types of gully boundaries: the main channel of the gully and the main channel including tributaries

Survey No	Survey Period	Soil Loss (m^3)				
		G1_Main Channel	G1_with tributaries	G2_Main Channel	G3_Main Channel	G3_with tributaries
1	07/15/2016-08/08/2016	0.087	0.105	0.008	-0.526	-0.542
2	08/08/2016-09/02/2016	-0.036	-0.043	-0.005	0.626	0.657
3	09/02/2016-10/13/2016	0.033	0.035	0.034	0.081	0.076
4	10/13/2016-12/08/2016	-0.010	-0.011	-0.008	0.041	0.045
5	12/08/2016-04/19/2017	-0.021	-0.018	0.045	0.030	0.024
6	04/19/2017-05/13/2017	0.046	0.052	0.016	-0.015	-0.021
7	05/13/2017-07/05/2017	-0.132	-0.146	0.019	-0.149	-0.137
8	07/05/2017-10/02/2017	0.166	0.195	-0.036	0.210	0.225
9	10/02/2017-11/03/2017	-0.014	-0.014	0.001	0.133	0.152
10	11/03/2017-12/16/2017	0.008	0.013	-0.005	0.416	0.456
11	12/16/2017-03/20/2018	-0.030	-0.040	-0.010	0.020	0.020

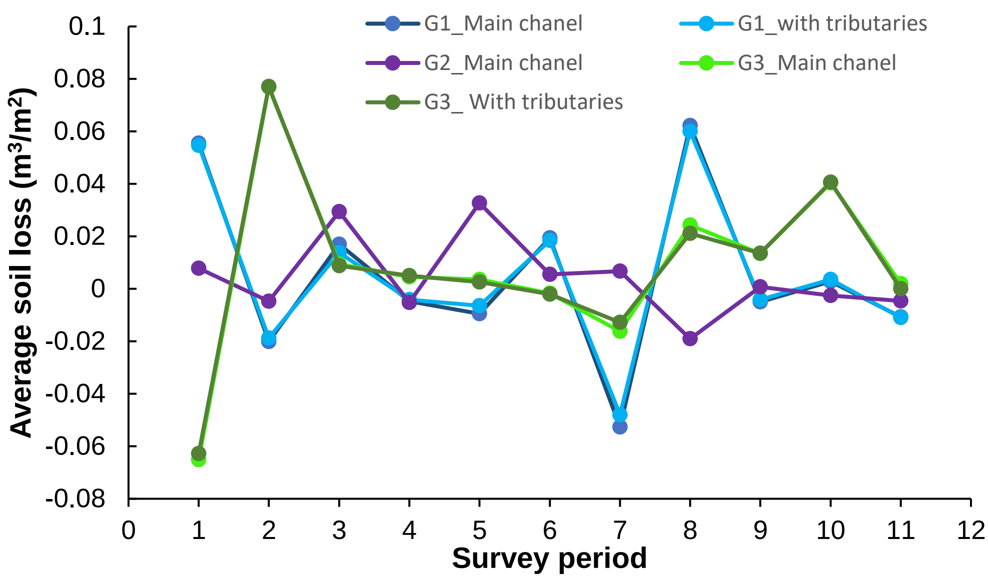

Figure 4-25: Average soil loss of three gullies Two types of gully boundaries were used; boundary of the main channel (normal), and boundary of main channel and tributaries (extended)

To compare soil loss of three gullies, soil loss values were averaged using the gully surface areas. Figure 4-25 shows averaged soil loss/acumination values and soil loss/acumination pattern of the three gullies. Actual soil loss/acumination values are shown in Table 4-6. The positive values indicate the soil loss and negative values indicate soil accumulation. In the first survey period, 0.087 m^3 of soil was removed from the main channel of Gully 1, and 0.008 m^3 of soil was removed from Gully 2. In this period the field received 89mm of rainfall within 6 wet days, and the soil was poorly covered with the vegetation and residue. However, in this period the Gully 3 experienced soil accumulation (0.526 m^3), especially in the gully outlet area. In the Gully 1, most considerable soil loss (0.166 m^3) occurred during the eighth survey period; the highest daily rainfall also occurred in the same survey period. In the Gully 1, soil losses occurred in the first, third, sixth, eighth, and tenth survey periods and soil accumulations were occurred in the second, fourth, fifth, seventh, ninth, and eleventh survey periods.

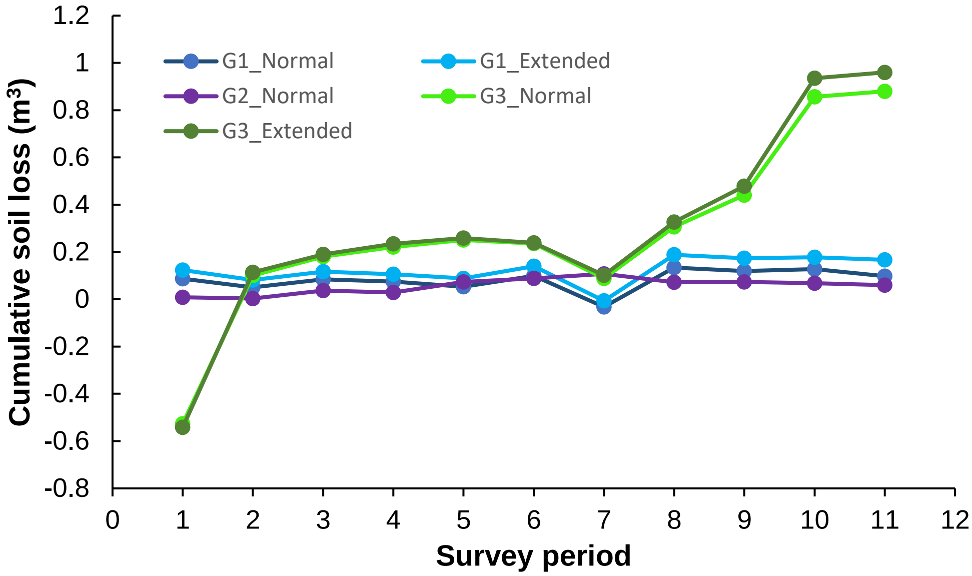

Figure 4-26: Cumulative soil loss for three gullies. Two types of gully boundaries were used; boundary of the main channel (normal), and boundary of main channel and tributaries (extended)

Figure 4-26 shows the cumulative soil loss for 20 months period of the three gullies. In 20 months, 0.098 m^3 of soil was removed from the main channel of the Gully 1 and 0.058 m^3, 0.876 m^3 from Gully 2 and Gully 3 respectively. From June, 2017 to December, 2017 cumulative soil loss of Gully 3 increased rapidly.

Seasonal soil loss

From July, 2016 to March, 2018 over the 20 months, three gullies were monitored using photogrammetry technique. This 20-month period contained two growing seasons and two non-growing seasons. The DEMs corresponds to these seasons were used to analyze the gully responses in each season. Figure 4-27, Appendix-G and Appendix-H show soil accumulation/erosion patterns of each season.

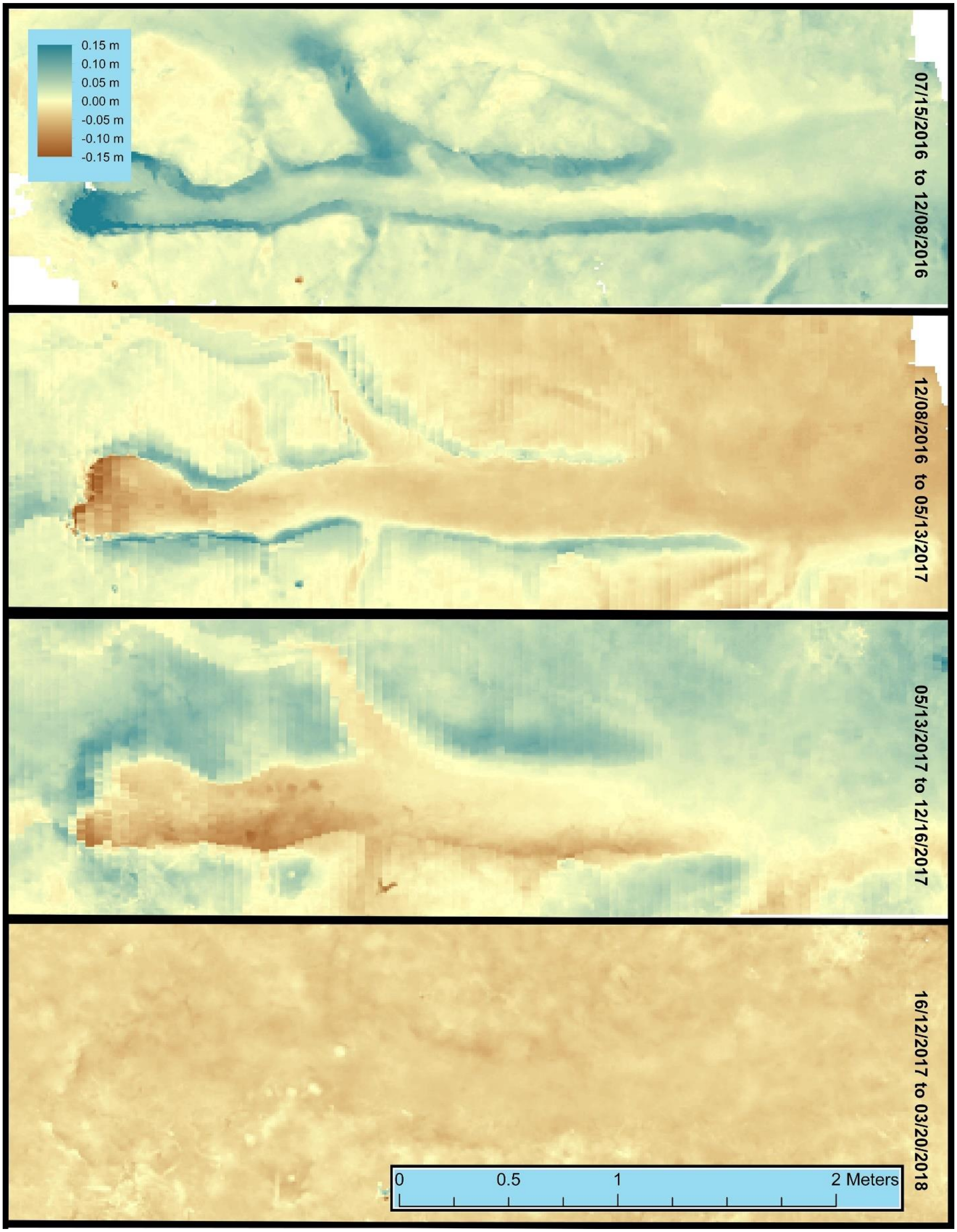

Figure 4-27**: Seasonal soil loss of Gully 1 from July, 2016 to March, 2018**

Figure 4-27 shows the seasonal soil loss pattern of the Gully 1. From the beginning of the 2016 growing season to the end of the 2016 growing season 0.094 m^3 of soil removed from the main channel of the Gully 1 and from December, 2016 to early May, 2017 (Dormant season 2016-2017), 0.194 m^3 of soil accumulated in the main channel of Gully 1. Similar soil loss and accumulation pattern observed in the 2017 growing season and 2017-2018 dormant season. In 2017 growing season 0.160 m^3 of soil removed from the main channel of the Gully 1 and in 2017-2018 dormant season 0.030 m^3 of soil removed. Table 4-7 shows the volume of seasonal soil loss of three gullies.

Table 4-7: Seasonal Soil loss of three gullies by the two types of gully boundaries: the main channel of the gully and main channel including tributaries

Season	Survey Period	Soil Loss (m^3)				
		G1_Main Chanel	G1_with tributaries	G2_Main Chanel	G3_Main Chanel	G3_with tributaries
2016-Growing	07/13/2016-12/08/2016	0.094	0.117	0.036	0.197	0.217
2016-2017 Dormant	12/08/2016-05/13/2017	-0.194	-0.216	-0.048	-0.205	-0.184
2017-Growing	05/013/2017-12/16/2017	0.160	0.189	-0.036	0.395	0.426
2017-2018 Dormant	12/16/2017-03/20/2018	-0.030	-0.040	-0.010	0.020	0.020

The seasonal expansion rate of the gully

Depth, width, cross-sectional area rapidly changes within the short period, and temporal resolution of photogrammetry was adequate to identify those changes. Three gully cross-sections; (close to the headcut area, middle of the gully length, close to the outlet) were considered to get the average width, depth and cross-sectional area of the gullies. Table 4-8 shows gully expansion rates in growing and dormant season.

Table 4-8: Gully expansion rate in growing and dormant seasons

		Growing	Dormant
Gully 1	Width	35.53%	14.34%
	Cross-sectional area	69.72%	-12.31%
	Mean Depth	16.55%	-17.22%
Gully 2	Width	13.60%	2.06%
	Cross-sectional area	20.57%	18.85%
	Mean Depth	16.72%	-6.79%
Gully 3	Width	6.33%	-47.98%
	Cross-sectional area	15.27%	-33.40%
	Mean Depth	31.25%	-52.99%

The three gullies show expansion over the growing period by increasing the width, depth, and the cross-sectional area. However, three gullies showed three different expansion rates. Gully 1 showed 69.72% expansion rate, Gully 2 showed 20.57% expansion rate, and Gully 3 showed 15.27% expansion rate. In the dormant season Gully 1 and Gully 3 experienced a shrinkage and Gully 2 experienced 18.85% of expansion. Shrinkage rate of the Gully 1 was 12.31%, and the shrinkage rate of Gully 3 was 33.40%. In the dormant season, sediment was deposited in the three gullies. The sediment deposition resulted in a negative depth increment rate in the dormant season.

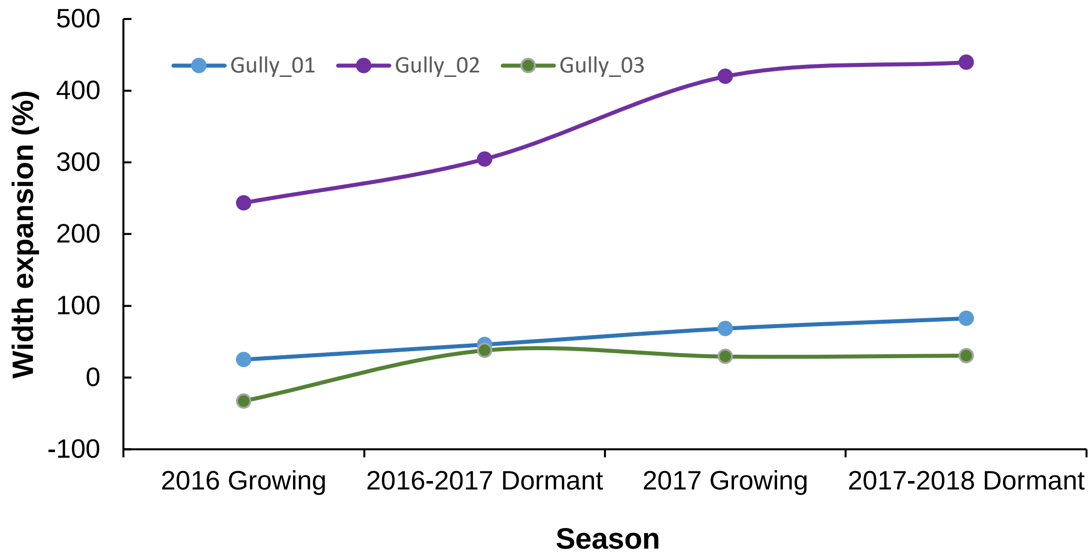

Figure 4-28: Average percentage of gully width expansion with respect to the initial width

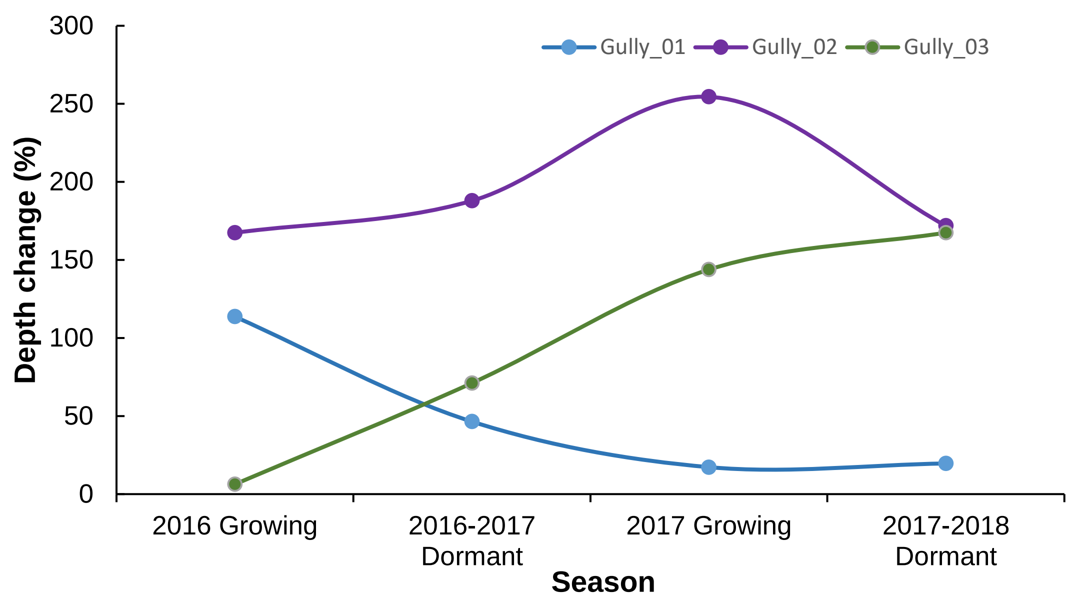

Figure 4-29: Average percentage of gully depth change with respect to the initial depth

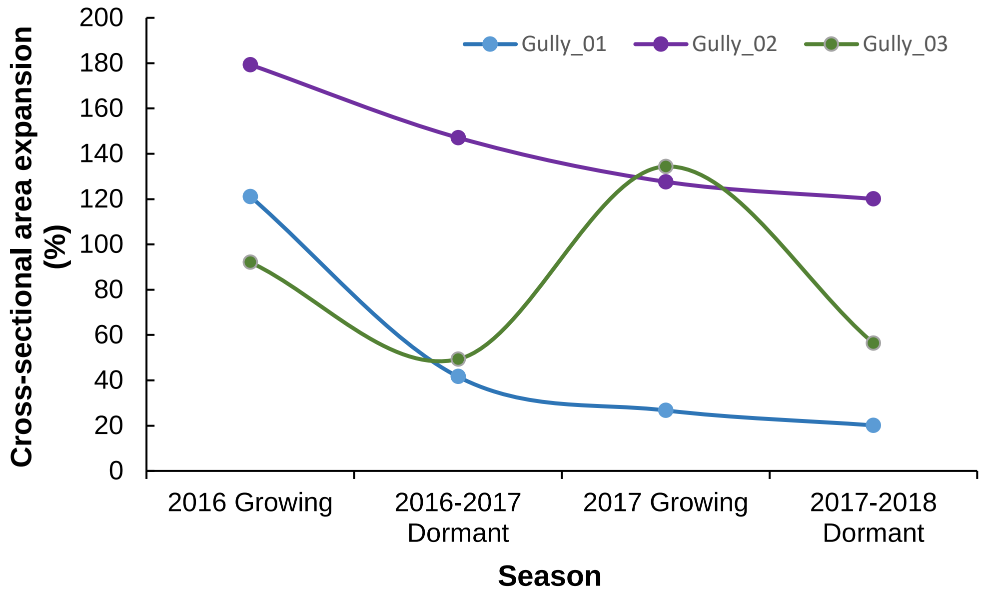

Figure 4-30: Average percentage of cross-sectional area change with respect to the initial average cross-sectional area

Gully 1 and Gully 2 show widening over time. However, Gully 2 has the highest width expansion percentage (more than 200%) throughout the four seasons compared to the other two gullies (Figure 4-28). The highest value was 439.5% in 2017-2018 dormant season. Gully 1 shows a slight width expansion percentage (less than 100%) throughout the survey period. The recorded highest expansion rate was 84% in 2017-2018 dormant season. In 2016 growing season, Gully 3 shows 32% width decrement, and after that, it shows a 30% of width expansion in 2016-2017 dormant season and remains without a noticeable change until the end of the survey (Figure 4-28).

Figure 4-29 shows the change in the average depth percentage of three gullies. Deepening rate of the Gully 1 decreases over time. However, Gully 2 and Gully 3 show positive deepening rate over time and had a maximum percentage change (254.5%) in 2017 growing season. Gully 3 also shows a positive deepening rate throughout the survey period. The change of depth percentage increases over time, and in 2017-2018 dormant season the change of depth was 167.47%.

Figure 4-30 shows the percentage of average cross-sectional area change with respect to the initial average cross-sectional area. For Gully 1 and Gully 2 the average cross-sectional area increased at a decreasing rate. Gully 3 shows large increment percentages (92%, 134%) in the growing season and low increment percentages in the dormant seasons (49%, 56%).

4.7 Discussion and conclusions

The proposed photogrammetry survey method was used to survey three gullies over two years. Within the twenty months study period, twelve surveys were conducted, and three different behaviors were identified in three gullies located within the same field under the same management practices (no-till), under the same weather condition and soil type.

The behavior of Gully 1 was similar to the behavior of EG. A periodic pattern of soil-eroding and depositing was identified in Gully 1; where soil erosion happened in the growing season and sediment was deposited in the dormant season. There was a clear headcut detected in Gully 1 which moved continuously uphill regardless of the season. The headcut migrated 39cm in two years. The process of the development of Gully 1 was driven by surface runoff within the main channel and four tributary channels. During more intense runoff events, the outlet of the Gully 1 was back flooded from the adjacent larger channel. To describe the channel development process of Gully 1, these factors were needed to consider. In 2016 growing season, soil erosion happened within the entire gully area. This indicates in this season the critical shear stress value was below the acting shear stress value (equation 2-1) and the sediment load was below the sediment transport capacity (Equation 2-2) In 2016-2017 dormant season soil erosion occurred at the gully banks, and soil deposition occurred at the gully bed indicating both critical shear stress and the sediment transport capacity controlled the total soil loss. In 2017 growing season, residue deposition in the gully bed caused to increase the critical shear stress values.

Gully 2 showed a mixed behavior of EG and a large rill. There was no clear headcut, and there was no soil eroding and depositing pattern related to the growing and dormant seasons. Compared to the other two gullies, Gully 2 had a dense canopy cover. Based on the eroded and deposited points, critical shear stress can be identified as the main factor that controlled the sediment yield (Equation 2-1) in the 2016 growing/dormant season and both critical shear stress and sediment transport capacity affected to the 2017 growing season and dormant season (Equation 2-1 and Equation 2-2).

The behavior of Gully 3 was similar to rill behavior. The process of the Gully 3 development was driven by runoff in the main channel, one large tributary channel. Surface flow in the gully traveled 20m of gully length. To describe the channel development process, these factors need to be considered. Gully 3 also showed a periodic pattern of soil eroding and sediment depositing. In 2018 dormant season, there was non-significant soil erosion (0.02 m^3) instead of soil deposition as expected in a periodic pattern. Amount of soil erosion might change if the surveying continued until the beginning of May, 2018. Similar to rill, there was no clear headcut development in gully 3. Based on the eroded and deposited points; critical shear stress was the main factor that controlled the sediment yield in all seasons except the 2017 growing season. Both critical shear stress and sediment transport capacity affected the 2017 growing season.

All the gullies showed a positive expansion rate. However, the expansion rate varied with time. Therefore, the comparison of two consecutive surveys showed positive or negative growth rates with respect to the previous survey. The DEM provides 3-D information of the gullies, and actual gully changes can be identified by comparing two DEMs corresponds to two different surveys. Based on the DEM analysis, on average, the gullies in the studied field lost 4-6 mm soil layer from the gully surface in every growing season.

Headcut, channel bed, and side walls are the main sediment sources in EG erosion. However, only one gully showed a headcut advancement among the three gullies observed in this study.

Close-range photogrammetry does not cover a larger surrounding area of the gully. With the limited surrounding area, it is unable to decide the natural slope of the soil surface. Therefore, widely known, channel boundary determination procedures cannot be used to determine the gully boundaries. This study proposed a surface curvature-based method to identify the gully boundaries to overcome the issue. This method worked well with the gully banks that had dramatical slope changes. However, the proposed method did not work well for gully banks with gradual slopes.

Close-range photogrammetry can be used to explore gully characteristic at a microscopic level. However, in the growing season, most of the area of the gullies are covered by the crop canopy. Therefore, photogrammetry surveys in later of the growing season are challenging. Because of the obstruction of the canopy cover, the photogrammetry surveys were unable to conduct in July, August, and September in 2017, while four surveys were conducted during the 2017 growing season.

From the field surveying, it was concluded that the proposed photogrammetry survey method is adequate to identify the gully expansion rate, exact locations of the expansion, the volume of soil loss/deposition and headcut movement rate. The photogrammetry survey has a higher accuracy level compared to the other gully survey methods, and the detailed data provided by the photogrammetry method can be used to develop and validate EG erosion models.

5 Summary and Main Conclusions

Ensuring food and water security is the biggest challenge the world is facing today. Soil erosion leads to decrease in food production and water quality degradation. Ephemeral gully (EG) erosion is one of the major sources of soil degradation and reservoir sedimentation. However, mechanisms related to EG formation, location, geomorphological properties related to storm characteristics, and the amount of soil loss are not understood well enough. Therefore, more field measurements, lab experiments, and computer modeling studies are needed to gain a better insight into the physical processes that are responsible for the development of EG erosion.

The purpose of this study was to evaluate the accuracy of the photogrammetry method to use for the field measurements of EGs and monitoring and assessing the development of EGs. A laboratory experiment was conducted to evaluate the accuracy of the close-range photogrammetry survey. In this experiment, an optimal number of ground reference points (GRP) and the best spatial distribution of ground control points were identified. The minimum error occurred at 4 GRPs per $1m^2$ GRP density. The minimum error was 1.1 cm along X-axis, 1.06 cm along the Y-axis and 2.65 cm along the Z-axis. However, 8-20 per $4m^2$ (2- 5 GRPs per $1m^2$) GRP density is acceptable. From 8 to 12 increment of 4 GRPs, total accuracy increases by 8.9% and from 8 to 16 increment of 8 GRPs, total accuracy increases by 4.4%. From 8 to 20 increment of 12 GRPs total accuracy decreases by 5.3%. It is recommended to use 2 GRPs per $1m^2$ density to large scale projects to save labor and time.

The impact of camera angle and image overlap percentage were analyzed; any camera angle between 0 degrees to 30 degrees and more than 70% image overlap percentage was identified as the best image capturing settings. Image overlap percentage positively related to the number of points in the point cloud and image; higher overlap percentages generated denser point clouds. A dispersed distribution of ground control points added the minimum error to the photogrammetry model.

The photogrammetry accuracy study assumed there is no interaction effect of the camera angle and the image overlap percentage. Also, it was assumed that the total station is accurate and does not create any error in the laboratory environment. In the field conditions, it is hard to maintain the constant camera angle and constant image overlap percentage. However, the accuracy study concluded that 0 to 30-degree camera angle and more than 70% image overlap percentage would generate accurate results. Therefore, the image capturing step has a tolerance.

The proposed photogrammetry method including camera and camera setup is suitable and accurate enough to monitor the morphological changes of the EGs in the agricultural fields and can be easily adapted to large scale projects.

The field experiment was conducted to monitor and assess the development of EGs. The proposed photogrammetry method was used and was able to obtain detailed information of gully development. After setting up the coordinate system and the ground control points in the field, the proposed survey method can be applied frequently to get the desired temporal resolution. The canopy cover limits the photogrammetry survey in the growing season.

Close-range photogrammetry does not cover a large surrounding area of the gully. With the limited surrounding area, it is unable to decide the natural slope of the soil surface. Therefore, the surface curvature-based method was proposed to identify gully boundaries. The proposed method worked well with the gully banks with dramatical slope changes. However, unable to identify clear gully boundaries when gully banks have gradual slopes. The gully boundary delineation method requires further improvements to apply for the gradual slopes.

From the field study, the gully expansion rate, pattern, locations of the expansion/shrinkage, soil erosion/deposition pattern and soil erosion/deposition rate were identified and properly documented. Those data can be used to calibrate soil erosion models. Critical shear stress and the sediment transport capacity are the main factors that control the sediment yield on EGs. The dominant erosion controlling factor can be determined by identifying the location (gully bed, side wall) of the gully where the soil erosion or deposition occurred. Erosion of the gully bed and side walls indicate that the acting shear stress is greater than the critical shear stress and sediment load is under the sediment transport capacity; Erosion of the side walls and deposition on the gully bed indicate that the acting shear stress is greater than the critical shear stress and sediment load is over the sediment transport capacity; Deposition on the gully bed without eroding side walls indicates the acting shear stress does not exceed the critical shear stress and sediment load is over the sediment transport capacity. The dominant erosion controlling factor can be used to determine the best management practices to reduce the sediment yield.

Foster and Lane model is a physically based EG development model. It assumes a rectangular shape of the gully cross section that erodes downward until its bottom reaches a non-erodible layer. After reaching the non-erodible layer, gully widens by side wall sloughing. The conducted field experiment showed the actual gully development process deviates from the Foster and Lane's assumption and a new physical based EG development model is needed to develop in order to simulate the actual EG development process. Soil erosion is a function of runoff, and the runoff is determined by the rainfall amount, rainfall intensity, soil type, ground coverage, drainage area, and soil moisture condition. Therefore, it is difficult to make a direct relationship between the gully expansion rate and the rainfall amount. Future studies with runoff measurements and soil conditions are needed to develop a better understanding of physical processors of EGs.

References

Agüera, V. F., Carvajal, R. F., Martínez, C. P. (2017). Assessment of photogrammetric mapping accuracy based on variation ground control points number using unmanned aerial vehicle. *Measurement: Journal of the International Measurement Confederation*, *98*, 221–227. https://doi.org/10.1016/j.measurement.2016.12.002

Bennett, S. ., Casali, J., Robinson, K. ., Kadavy, K. . (2000a). Characteristics of actively eroding ephemeral gullies in an experimental channel. *American Society of Agricultural and Biological Engineers*, *43*(3), 641–649.

Bennett, S. J., Casali, J., Robinson, K. M., Kadavy, K. C. (2000b). Characteristics of actively eroding ephemeral gullies in an experimental channel. *Transactions of the ASAE*, *43*(3), 641.

Bernard, J., Lemunyon, J., Merkel, B., Theurer, F., Widman, N., Bingner, R., … Wilson, G. (2010). *Ephemeral Gully Erosion - A National Resource Concern. U.S. Department of Agriculture. NSL Technical Research Report No. 69*. Retrieved from https://www.ars.usda.gov/ARSUserFiles/60600500/NSL Research Reports/Bernard, Lemunyon, Merkell, Theurer, Widman, BIngner, Dabney, Langendoen, Wells, Wilson, NSL Research No. 69.pdf

Brasington, J., Smart, R. M. A. (2003). Close range digital photogrammetric analysis of experimental drainage basin evolution. *Earth Surface Processes and Landforms*, *28*(3), 231–247. https://doi.org/10.1002/esp.480

Brian D. Collins, Kristin M. Brown, and H. C. F. (2008). *Evaluation of Terrestrial LIDAR for Monitoring Geomorphic Change at Archeological Sites in Grand Canyon National Park , Arizona Open – File Report 2008 – 1384*. *U.S. Geological Survey*. Retrieved from https://pubs.usgs.gov/of/2008/1384/of2008-1384.pdf

Campo-Bescos, M. A., Flores-Cervantes, J. H., Bras, R. L., Casali, J., Giraldez, J. V. (2013). Evaluation of a gully headcut retreat model using multitemporal aerial photographs and digital elevation models. *Journal of Geophysical Research: Earth Surface*, *118*(4), 2159–2173. https://doi.org/10.1002/jgrf.20147

Casalí, J., Loizu, J., Campo, M. A., De Santisteban, L. M., Álvarez-Mozos, J. (2006). Accuracy of methods for field assessment of rill and ephemeral gully erosion. *Catena*, *67*(2), 128–138. https://doi.org/10.1016/j.catena.2006.03.005

Castillo, C., Pérez, R., James, M. R., Quinton, J. N., Taguas, E. V., Gómez, J. A. (2012). Comparing the Accuracy of Several Field Methods for Measuring Gully Erosion. *Soil Science Society of America Journal*, *76*(4), 1319. https://doi.org/10.2136/sssaj2011.0390

Collins, B. D., Brown, K. M., Fairley, H. C. (n.d.). *Evaluation of Terrestrial LIDAR for Monitoring Geomorphic Change at Archeological Sites in Grand Canyon National Park, Arizona Open-File Report 2008-1384*.

Cultural Heritage Imaging | Photogrammetry. (2018). Retrieved September 25, 2018, from http://culturalheritageimaging.org/Technologies/Photogrammetry/index.html

Daba, S., Rieger, W., Strauss, P. (2003). Assessment of gully erosion in eastern Ethiopia using photogrammetric techniques. *Catena*, *50*(2–4), 273–291. https://doi.org/10.1016/S0341-8162(02)00135-2

Daggupati, P., Sheshukov, A. Y. (2013). Predicting Ephemeral Gully Location and Length Using Topographic Index Models. *Transactions of the ASABE, 56*(2003), 1427–1440. https://doi.org/10.13031/trans.56.10087

Daggupati, P., Sheshukov, A. Y., Douglas-Mankin, K. R. (2014). Evaluating ephemeral gullies with a process-based topographic index model. *Catena*, *113*, 177–186.

https://doi.org/10.1016/j.catena.2013.10.005

Dai, Fei Lu, M. (2012). Three-Dimensional Modeling of Site Elements by Analytically Processing Image Data Contained in Site Photos. *Journal of Construction Engineering and Management*, *139*(7), 881–894. https://doi.org/10.1061/(ASCE)CO.1943-7862.0000655

Dai, F., Feng, Y., Hough, R. (2014). Photogrammetric error sources and impacts on modeling and surveying in construction engineering applications, 1–14.

Davis, S. S., Foster, G. R., Huggins, L. F. (1983). Deposition of non-uniform sediment on concave slopes. *Transactions of the ASAE*, *7*(4), 1057–1063.

Duerer, A. (1977). History of Photogrammetry Early Developments 1. Retrieved from https://spatial.curtin.edu.au/local/docs/HistoryOfPhotogrammetry.pdf

Eos Systems Inc. (2013). *PhotoModeler Online Tutorials*. Retrieved from https://www.photomodeler.com/tutorial-vids/online-tutorials.htm

ESRI. (2016). Curvature function—Help | ArcGIS for Desktop. https://doi.org/10.1002/eji.200425864

Evans, M., Lindsay, J. (2010). High resolution quantification of gully erosion in upland peatlands at the landscape scale. *Earth Surface Processes and Landforms*, *35*(8), 876–886. https://doi.org/10.1002/esp.1918

Fonstad, M. A., Dietrich, J. T., Courville, B. C., Jensen, J. L., Carbonneau, P. E. (2013). Topographic structure from motion: A new development in photogrammetric measurement. *Earth Surface Processes and Landforms*, *38*(4), 421–430. https://doi.org/10.1002/esp.3366

Foster, G. . (1982a). Channel erosion within farm fields. *Preprint*, 7–82.

Foster, G. ., Lombardi, F., Moldenhauer, W. . (1982). Evaluation of rainfall-runoff erosivity factors for individual storms. *Transactions of the ASAE*, *25*(1), 124–129. Retrieved from http://agris.fao.org/agris-search/search.do?recordID=US19830852214

Foster, G. R. (1982b). Modeling the erosion process. *Hydrologic Modeling of Small Watersheds*. Retrieved from https://ci.nii.ac.jp/naid/10015695215/en/

Foster, G. R., Lane, L. (1983). Erosion by concentrated flow in farm fields. In *Proceedings of the DB Simons symposium on erosion and sedimentation* (pp. 9–65).

Foster, G. R., Meyer, L. D. (1972). closed-form soil erosion equation for upland areas. *Sedimentation*, 12–1.

Gao, P. (2013). *Rill and Gully Development Processes*. *Treatise on Geomorphology* (Vol. 7). Elsevier Ltd. https://doi.org/10.1016/B978-0-12-374739-6.00156-1

Gessesse, G. D., Fuchs, H., Mansberger, R., Klik, A., Rieke-Zapp, D. H. (2010). Assessment of erosion, deposition and rill development on irregular soil surfaces using close range digital photogrammetry. *Photogrammetric Record*, *25*(131), 299–318. https://doi.org/10.1111/j.1477-9730.2010.00588.x

Gillan, J. K., Karl, J. W., Elaksher, A., Duniway, M. C. (2017). Fine-resolution repeat topographic surveying of dryland landscapes using UAS-based structure-from-motion photogrammetry: Assessing accuracy and precision against traditional ground-based erosion measurements. *Remote Sensing*, *9*(5), 1–24. https://doi.org/10.3390/rs9050437

Gómez-Gutiérrez, Á., Schnabel, S., Berenguer-Sempere, F., Lavado-Contador, F., Rubio-Delgado, J. (2014). Using 3D photo-reconstruction methods to estimate gully headcut erosion. *Catena*, *120*, 91–101. https://doi.org/10.1016/j.catena.2014.04.004

González-Jorge, H. (2011). Verification artifact for photogrammetric measurement systems. *Optical Engineering*, *50*(7), 073603. https://doi.org/10.1117/1.3598868

Govers, G., Everaert, W., Poesen, J., Rauws, G., De Ploey, J., Lautridou, J. P. (1990). A long flume study of the dynamic factors affecting the resistance of a loamy soil to concentrated flow erosion. *Earth Surface Processes and Landforms*.

https://doi.org/10.1002/esp.3290150403

Karimov, V. R. (2017). *Mathematical modeling of ephemeral gully erosion*. KANSAS STATE UNIVERSITY.

Karimov, V. R., Sheshukov, A. Y. (2017). Effects of intra-storm soil moisture and runoff characteristics on ephemeral gully development: Evidence from a no-till field study. *Water (Switzerland)*, *9*(10), 8–10. https://doi.org/10.3390/w9100742

Keesstra, S. D., Bouma, J., Wallinga, J., Tittonell, P., Smith, P., Cerdà, A., … Fresco, L. O. (2016). The significance of soils and soil science towards realization of the United Nations sustainable development goals. *Soil*, *2*(2), 111–128. https://doi.org/10.5194/soil-2-111-2016

KWO, K. W. office. (2008). *Sedimentation in Our Reservoirs: Causes and Solutions*. Retrieved from http://www.ksre.ksu.edu.

Ludwig, B., Boiffin, J., Chadˀuf, J., Auzet, A.-V. (1995). Hydrological structure and erosion damage caused by concentrated flow in cultivated catchments. *CATENA*, *25*(1), 227–252. https://doi.org/https://doi.org/10.1016/0341-8162(95)00012-H

Luhmann, T., Robson, S., Kyle, S. A., Harley, I. A. (2006). *Close range photogrammetry: principles, techniques and applications*. Whittles.

Marzolff, I., Poesen, J. (2009). The potential of 3D gully monitoring with GIS using high-resolution aerial photography and a digital photogrammetry system. *Geomorphology*, *111*(1–2), 48–60. https://doi.org/10.1016/j.geomorph.2008.05.047

McKean, J., Nagel, D., Tonina, D., Bailey, P., Wright, C. W., Bohn, C., Nayegandhi, A. (2009). Remote Sensing of Channels and Riparian Zones with a Narrow-Beam Aquatic-Terrestrial LIDAR. *Remote Sensing*, *1*(4), 1065–1096. https://doi.org/10.3390/rs1041065

Mikhail, E. M., Bethel, J. S. (James S., McGlone, J. C., of Photogrammetry, A. S., Sensing, R., Society, I. & G. I. (2004). *Manual of photogrammetry* (5th ed). Bethesda, Md. : American

Society of Photogrammetry and Remote Sensing.

Nachtergaele, J., Poesen, J. (1999). Assessment of soil losses by ephemeral gully erosion using high-altitude (stereo) aerial photographs. *Earth Surface Processes and Landforms*, *24*(8), 693–706. https://doi.org/10.1002/(SICI)1096-9837(199908)24:8<693::AID-ESP992>3.0.CO;2-7

National Research Council. (1986). *Soil Conservation: An Assessment of the National Resources Inventory* (2nd ed., Vol. 2). NATIONAL ACADEMY PRESS. https://doi.org/10.17226/648

Neugirg, F., Kaiser, A., Huber, A., Heckmann, T., Schindewolf, M., Schmidt, J., … Haas, F. (2016). Using terrestrial LiDAR data to analyse morphodynamics on steep unvegetated slopes driven by different geomorphic processes. *Catena*, *142*, 269–280. https://doi.org/10.1016/j.catena.2016.03.021

Nevalainen, P., Middleton, M., Sutinen, R., Heikkonen, J., Pahikkala, T. (2016). Detecting terrain stoniness from airborne laser scanning data. *Remote Sensing*, *8*(9), 1–21. https://doi.org/10.3390/rs8090720

NRCS, U. (1997). America’s Private Land: A Geography of Hope. *United States Department of Agriculture--Natural Resources Conservation Service, Washington, DC*, 39.

Perroy, R. L., Bookhagen, B., Asner, G. P., Chadwick, O. A. (2010). Comparison of gully erosion estimates using airborne and ground-based LiDAR on Santa Cruz Island, California. *Geomorphology*, *118*(3–4), 288–300. https://doi.org/10.1016/j.geomorph.2010.01.009

PhotoModeler Technologies. (2008). Factors Affecting Accuracy in Photogrammetry. Retrieved May 22, 2018, from https://info.photomodeler.com/blog/kb/factors_affecting_accuracy_in_photogramm/

Pimentel, D. (2006). SOIL EROSION : A FOOD AND ENVIRONMENTAL THREAT. *Environment, Development and Sustainability*, *8*, 119–137. https://doi.org/10.1007/s10668-

005-1262-8

Pineux, N., Lisein, J., Swerts, G., Bielders, C. . ., Lejeune, P., Colinet, G., Degré, A. (2017). Geomorphology Can DEM time series produced by UAV be used to quantify diffuse erosion in an agricultural watershed ? *Geomorphology*, *280*, 122–136. https://doi.org/10.1016/j.geomorph.2016.12.003

Quiñones-Rozo, C. A., Hashash, Y. M. A., Liu, L. Y. (2008). Digital image reasoning for tracking excavation activities. *Automation in Construction*, *17*(5), 608–622. https://doi.org/10.1016/j.autcon.2007.10.008

Rose, J., Smith, J., Chandle, J. S. (2009). High spatial resolution data acquisition for the geosciences: kite aerial photography. *Earth Surface Processes and Landforms*, *34*(1), 155–161. https://doi.org/10.1002/esp

Rutherford, A. (2011). *ANOVA and ANCOVA : a GLM approach*. Hoboken, N.J: Wiley.

Schindler, K. (2015). Mathematical foundations of photogrammetry. *Handbook of Geomathematics: Second Edition*, 3087–3103. https://doi.org/10.1007/978-3-642-54551-1_63

Schmid, T., Schack-Kirchner, H., Hildebrand, E. (2004). A case study of terrestrial laser scanning in erosion research: calculation of roughness and volume balance at a logged forest site. *International Archives of Photogrammetry, Remote Sensing and Spatial Information Sciences*, *XXXVI-8*(W2), 114–118.

Sims, J. T., Cunningham, S. D., Sumner, M. E. (1997). Assessing Soil Quality for Environmental Purposes: Roles and Challenges for Soil Scientists. *Journal of Environmental Quality*, *26*, 20–25. https://doi.org/10.2134/jeq1997.00472425002600010004x

Smith, L. (1993). Investigation of Ephemeral Gullies in Loessial Soils in Mississippi. *Technical Report. Vicksburg, Miss.U.S. Army Corps of Engineers, Waterways Experiment Station,* *GL-93-11*(August).

Spomer, R. G., Mahurin, R. L. (1984). Time-lapse remote sensing for rapid measurement of changing landforms. *Journal of Soil and Water Conservation*, *39*(6), 397–401.

Suzanne. (2013). 4 Ways To Bring Gamification of Education To Your Classroom - Top Hat Blog. https://doi.org/10.13031/2013.23968

The impact of population momentum on future population growth. (2017). *United Nations* (Vol. 171). Retrieved from https://esa.un.org/unpd/wpp/Publications/Files/PopFacts_2017-4_Population-Momentum.pdf

Thomas, A., Welch, R. (1988). Measurement of ephemeral gully erosion. *Transactions of the American Society of Agricultural Engineers*, *31*(6), 1723–1728. https://doi.org/10.13031/2013.30927

Valentin, C., Poesen, J., Li, Y. (2005). Gully erosion: Impacts, factors and control. *Catena*, *63*(2–3), 132–153. https://doi.org/10.1016/j.catena.2005.06.001

Vinci, A., Brigante, R., Todisco, F., Mannocchi, F., Radicioni, F. (2015). Measuring rill erosion by laser scanning. *Catena*, *124*, 97–108. https://doi.org/10.1016/j.catena.2014.09.003

Wells, R. R., Momm, H. G., Bennett, S. J., Gesch, K. R., Dabney, S. M., Cruse, R., Wilson, G. V. (2016). A Measurement Method for Rill and Ephemeral Gully Erosion Assessments. *Soil Science Society of America Journal*, *80*(1), 203–214. https://doi.org/10.2136/sssaj2015.09.0320

Zheng, F. L., Gao, X. T. (2000). oil erosion process and simulation on loess slope. *Xi'an: Shaanxi People's Publishing House*, *1*, 96–119.

Zoom40 Series | GeoMax. (n.d.). Retrieved May 22, 2017, from https://geomax-positioning.com/products/total-stations/zoom40-series

Appendix A -Photomodeler Project Report

Status Report Tree

Project Name: Gully 04.pmr

Problems and Suggestions (1)

Project Problems (1)

Problem: The lowest angle separation between points is lower than 5 degrees and will not be computed accurately.

Suggestion: Points with low angle separation will not solve with good accuracy. If possible, add a photo with greater angle separation.

Problems related to most recent processing (0)

Information from the most recent processing

Last Processing Attempt: Fri Apr 21 13:23:54 2017

Version: PhotoModeler Scanner 2016.2.1.2024 (64-bit)

Status: successful

Processing Options

Orientation: on

Only unoriented photos oriented.

Number of photos oriented: 108

Global Optimization: off

Calibration: off

Constraints: off

Total Error

Number of Processing Iterations: N/A

Number of Processing Stages: N/A

First Error: N/A

Last Error: N/A

Precisions / Standard Deviations

Quality

Photographs

Total Number: 109

Bad Photos: 1

Weak Photos: 0

OK Photos: 108

Number Oriented: 108

Number with inverse camera flags set: 0

Cameras

Camera1: Sony Alpha a7r

Calibration: yes

Number of photos using the camera: 109

Average Photo Point Coverage: 86%

Photo Coverage

Referenced points outside of the camera's calibrated coverage region:

Photo1 points outside region: none

Photo2 points outside region: none

Photo3 points outside region: #1248

Photo4 points outside region: #1248

Photo5 points outside region: none

Photo6 points outside region: none

Photo7 points outside region: none

Photo8 points outside region: none

Photo9 points outside region: none

Photo10 points outside region: none

Photo11 points outside region: #1679, #1876

Photo12 points outside region: #1679, #1785, #1876, #6301

Photo13 points outside region: none

Photo14 points outside region: none

Photo15 points outside region: none

Photo16 points outside region: none

Photo17 points outside region: none

Photo18 points outside region: none

Photo19 points outside region: none

Photo20 points outside region: none

Photo21 points outside region: none

Photo22 points outside region: none

Photo23 points outside region: none

Photo24 points outside region: none

Photo25 points outside region: none

Photo26 points outside region: #7966, #8041, #8087, #11720, #11772, #11820, #11866

Photo27 points outside region: none

Photo28 points outside region: none

Photo29 points outside region: #12320, #25368, #25446, #25592, #25708, #25807, #25810, #25811, #25835

Photo30 points outside region: #11753, #11775, #11950, #12023

Photo31 points outside region: none

Photo32 points outside region: none

Photo33 points outside region: #19453, #19533, #14608, #19783, #3412

Photo34 points outside region: none

Photo35 points outside region: none

Photo36 points outside region: none

Photo37 points outside region: none

Photo38 points outside region: none

Photo39 points outside region: none

Photo40 points outside region: none

Photo41 points outside region: none

Photo42 points outside region: none

Photo43 points outside region: none

Photo44 points outside region: none

Photo45 points outside region: none

Photo46 points outside region: none

Photo47 points outside region: none

Photo48 points outside region: none

Photo49 points outside region: none

Photo50 points outside region: none

Photo51 points outside region: none

Photo52 points outside region: none

Photo53 points outside region: none

Photo54 points outside region: none

Photo55 points outside region: none

Photo56 points outside region: none

Photo57 points outside region: none

Photo58 points outside region: none

Photo59 points outside region: none

Photo60 points outside region: none

Photo61 points outside region: none

Photo62 points outside region: none

Photo63 points outside region: none

Photo64 points outside region: none

Photo65 points outside region: none

Photo66 points outside region: none

Photo67 points outside region: none

Photo68 points outside region: none

Photo69 points outside region: none

Photo70 points outside region: none

Photo71 points outside region: none

Photo72 points outside region: none

Photo73 points outside region: #18360, #49615, #49760

Photo74 points outside region: none

Photo75 points outside region: none

Photo76 points outside region: none

Photo77 points outside region: none

Photo78 points outside region: #51340

Photo79 points outside region: none

Photo80 points outside region: none

Photo81 points outside region: none

Photo82 points outside region: none

Photo83 points outside region: none

Photo84 points outside region: none

Photo85 points outside region: none

Photo86 points outside region: none

Photo87 points outside region: none

Photo88 points outside region: none

Photo89 points outside region: none

Photo90 points outside region: none

Photo91 points outside region: none

Photo92 points outside region: none

Photo93 points outside region: none

Photo94 points outside region: none

Photo95 points outside region: none

Photo96 points outside region: none

Photo97 points outside region: none

Photo98 points outside region: none

Photo99 points outside region: none

Photo100 points outside region: none

Photo101 points outside region: none

Photo102 points outside region: #48572, #48598, #39090, #40241, #55995, #56045, #42339, #44514, #58664

Photo103 points outside region: #47146, #58353, #58404, #58822, #59507

Photo104 points outside region: none

Photo105 points outside region: none

Photo106 points outside region: none

Photo107 points outside region: none

Photo108 points outside region: #30916

Photo109 points outside region: none

Point Marking Residuals

Overall RMS: 0.987 pixels

Maximum: 4.112 pixels
Point 321 on Photo 22
Minimum: 0.000 pixels
Point 58759 on Photo 102
Maximum RMS: 2.942 pixels
Point 321
Minimum RMS: 0.000 pixels
Point 58759

Point Precisions
Overall RMS Vector Length: 0.218 m
Maximum Vector Length: 0.218 m
Point 60535
Minimum Vector Length: 0.218 m
Point 5
Maximum X: 0.118 m
Maximum Y: 0.1 m
Maximum Z: 0.154 m
Minimum X: 0.118 m
Minimum Y: 0.1 m
Minimum Z: 0.154 m

Point Angles
Maximum: 63.07 degrees
Point 43908
Minimum: 3.006 degrees
Point 34089
Average: 16.07 degrees

Check measurements
Checkpoint Delta
Max: 0.0178 m (Multipoint transform-P5, Pt 321)
Max X, Y, Z
X: 0.0155 m (Multipoint transform-P5, Pt 321)

Y: 0.0138 m (Multipoint transform-P6, Pt 1)

Z: 0.00487 m (Multipoint transform-P6, Pt 1)

Min: 0.00219 m (Multipoint transform-K7, Pt 129)

Min X, Y, Z

X: 0.000178 m (Multipoint transform-P4, Pt 161)

Y: 8.98e-005 m (Multipoint transform-P4, Pt 161)

Z: 0.000414 m (Multipoint transform-K5, Pt 97)

Average: 0.0102 m (from 13 items)

Appendix B - Point Cloud

ID X Y Z

1, 1356.580651, 1592.099402, 304.758282,

5, 1356.581148, 1592.102229, 304.763172,

9, 1355.543971, 1591.687334, 304.870227,

17, 1354.472663, 1591.252073, 304.892852,

25, 1353.490060, 1590.717067, 304.914446,

41, 1352.914978, 1590.675530, 304.935318,

49, 1355.761606, 1593.052277, 304.803029,

65, 1355.016552, 1592.727107, 304.838930,

97, 1353.715399, 1592.186026, 304.938407,

105, 1352.601336, 1591.931539, 304.926675,

113, 1351.098786, 1592.230916, 305.103400,

1, 1353.094045, 1590.500134, 304.921227,

2, 1353.098454, 1590.582644, 304.914027,

4, 1353.042717, 1590.502346, 304.931733,

5, 1352.942354, 1590.651282, 304.919071,

7, 1353.031407, 1590.472093, 304.931399,

8, 1352.948020, 1590.385862, 304.941169,

9, 1352.516754, 1590.965377, 304.820389,

10, 1352.438998, 1591.320887, 304.812163,

11, 1353.005826, 1590.476038, 304.933104,

12, 1352.526281, 1591.024242, 304.807460,

13, 1353.142439, 1590.645080, 304.891082,

14, 1353.057346, 1590.450951, 304.928032,

16, 1352.466510, 1591.283141, 304.802878,

17, 1353.351481, 1590.142585, 304.976557,

18, 1352.720492, 1590.730083, 304.903514,

19, 1352.791957, 1590.481069, 304.942263,

20, 1352.916652, 1590.474286, 304.934742,

21, 1353.016738, 1590.850598, 304.877513,

22,	1353.015956,	1590.415835,	304.939850,
23,	1352.779191,	1590.604212,	304.923453,
24,	1352.945195,	1590.616684,	304.921668,
26,	1353.104000,	1590.566397,	304.915270,
27,	1352.929019,	1590.455460,	304.935857,
28,	1352.905207,	1590.495329,	304.932187,
29,	1352.979705,	1590.573291,	304.931009,
30,	1353.096441,	1590.756669,	304.895951,
32,	1352.937507,	1590.446218,	304.939656,
33,	1352.727486,	1590.781901,	304.882009,
34,	1353.018232,	1590.452950,	304.935436,
35,	1352.990160,	1590.417084,	304.937575,
36,	1352.450652,	1591.099211,	304.814449,
37,	1352.457190,	1591.103270,	304.804944,
38,	1352.611004,	1590.831445,	304.886486,
39,	1353.056535,	1590.877011,	304.872763,
40,	1352.729113,	1590.735937,	304.902541,
41,	1353.097661,	1590.440655,	304.922420,
42,	1352.854324,	1590.575768,	304.926588,
43,	1353.120035,	1590.493942,	304.915002,
44,	1352.594299,	1590.888028,	304.880590,
45,	1352.990685,	1590.491874,	304.932740,
46,	1352.770785,	1590.624111,	304.923050,
47,	1353.046099,	1590.327059,	304.940013,
48,	1352.863320,	1590.543033,	304.928572,
51,	1353.116047,	1590.791499,	304.888284,
52,	1352.852293,	1590.606862,	304.926789,
53,	1353.006205,	1590.439586,	304.938532,
55,	1352.906170,	1590.322849,	304.953631,
56,	1352.747481,	1590.744884,	304.887273,
57,	1352.516968,	1591.330351,	304.796820,

Appendix C - Raster Images for Each Surveys-Gully 2

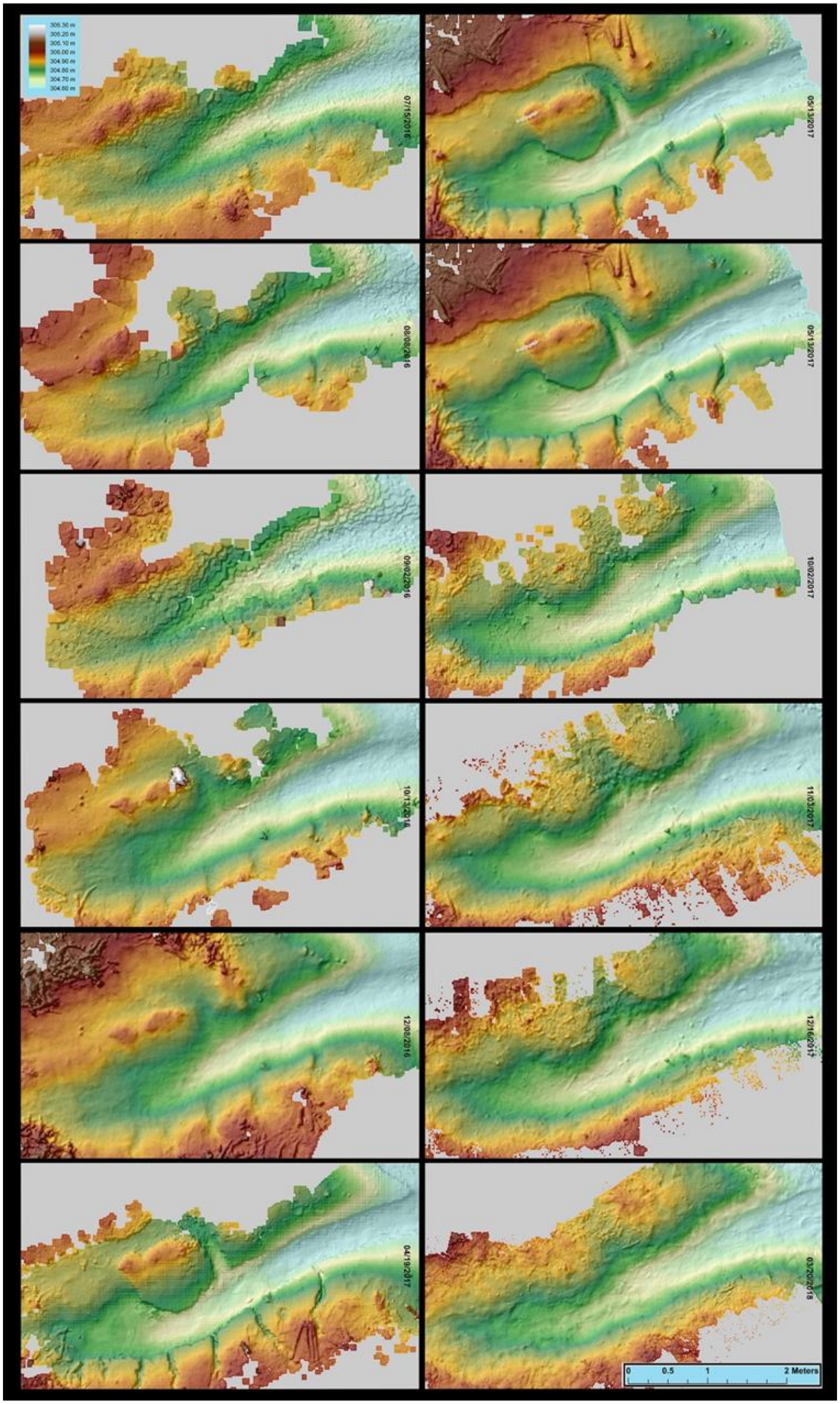

Appendix D - Raster Images for Each Surveys-Gully 3

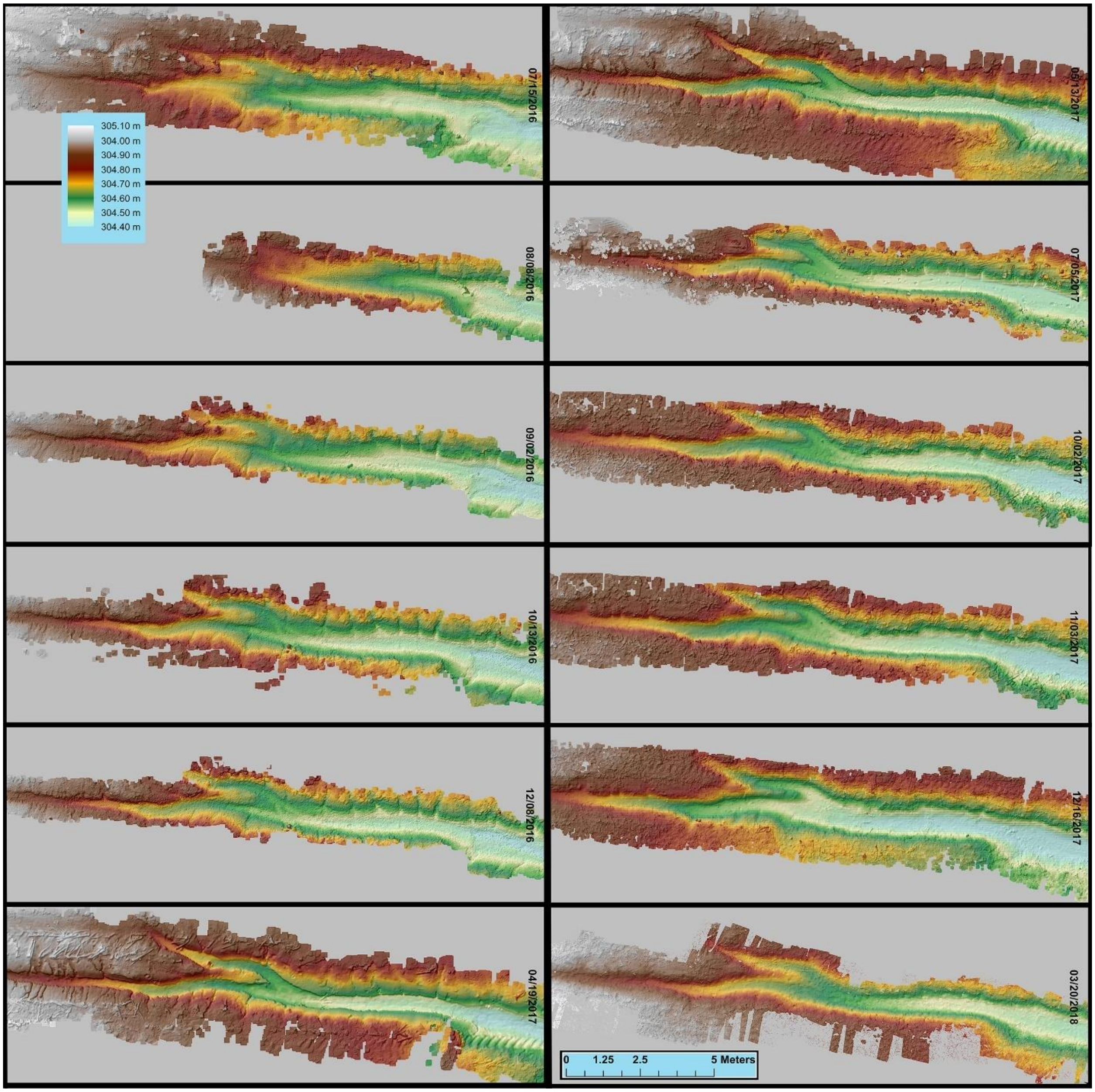

Appendix E – Soil Loss/Gain In-Between Surveys-Gully 2

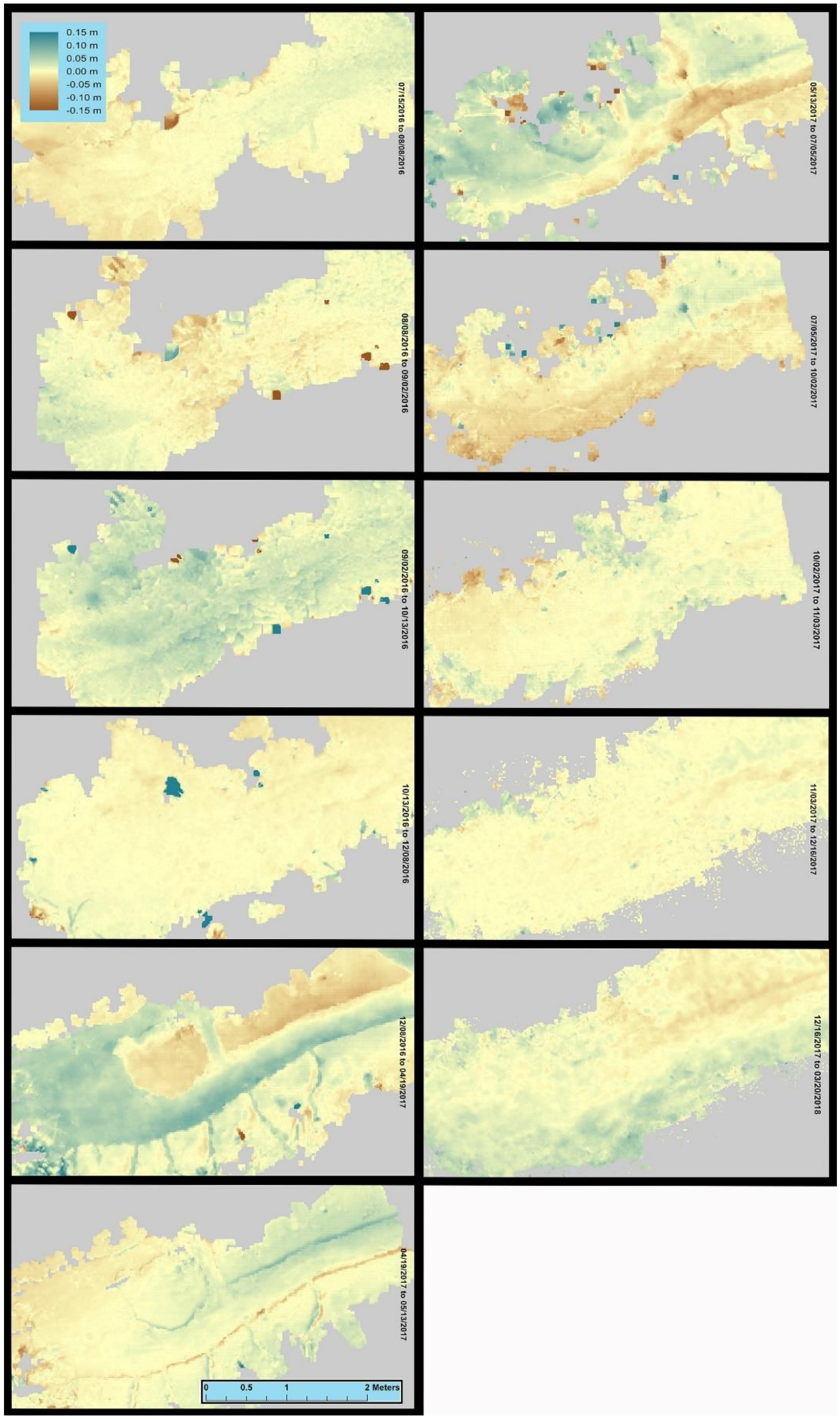

Appendix F – Soil Loss/Gain In-Between Surveys-Gully 3

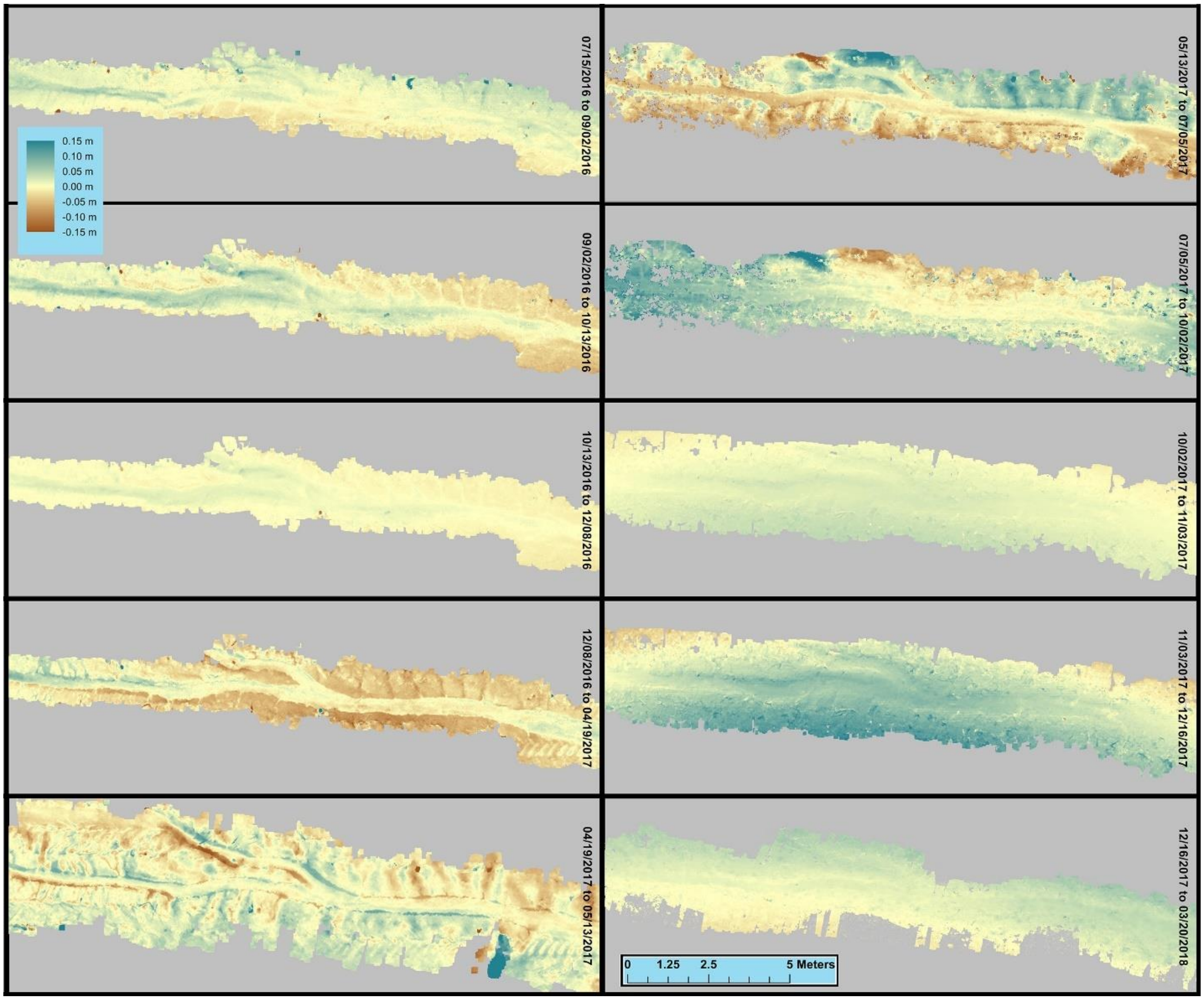

Appendix G – Seasonal Soil Loss/Gain-Gully 2

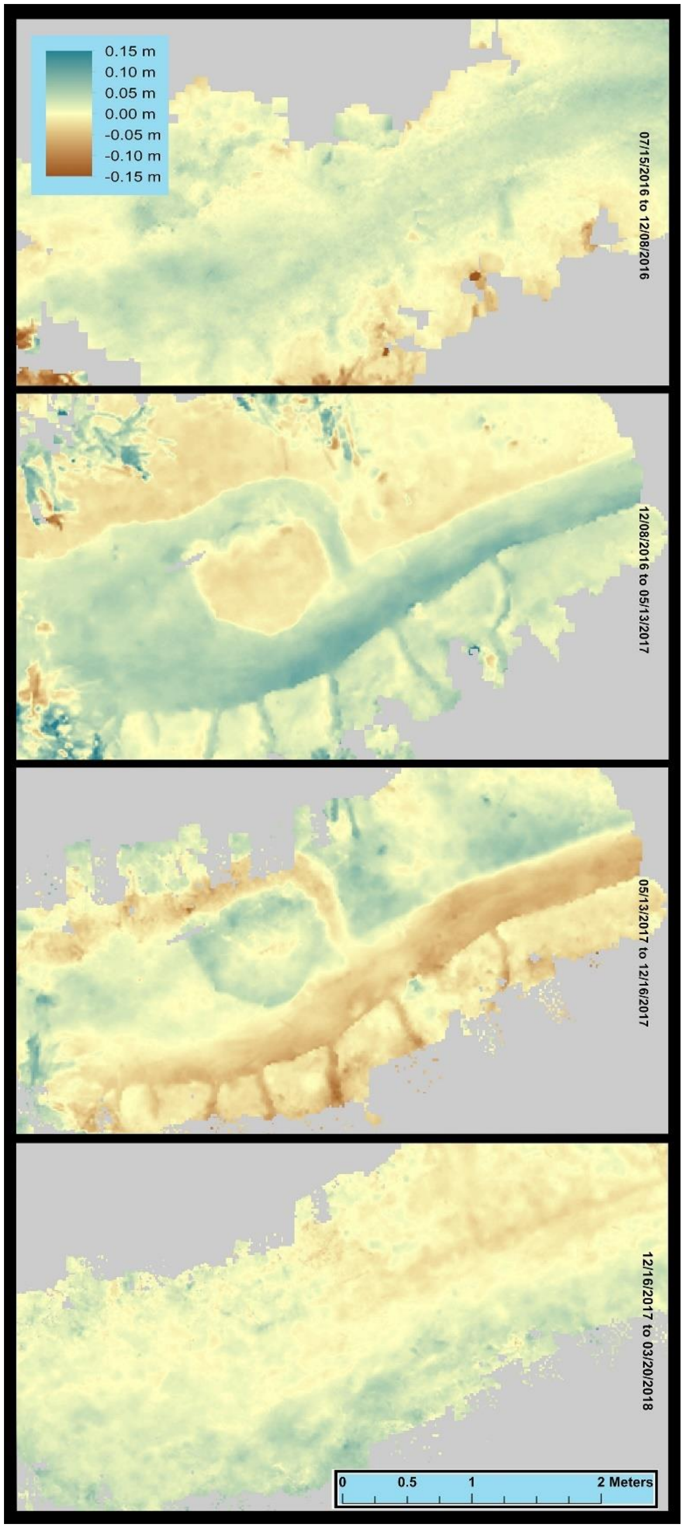

Appendix H - Seasonal Soil Loss/Gain-Gully 3

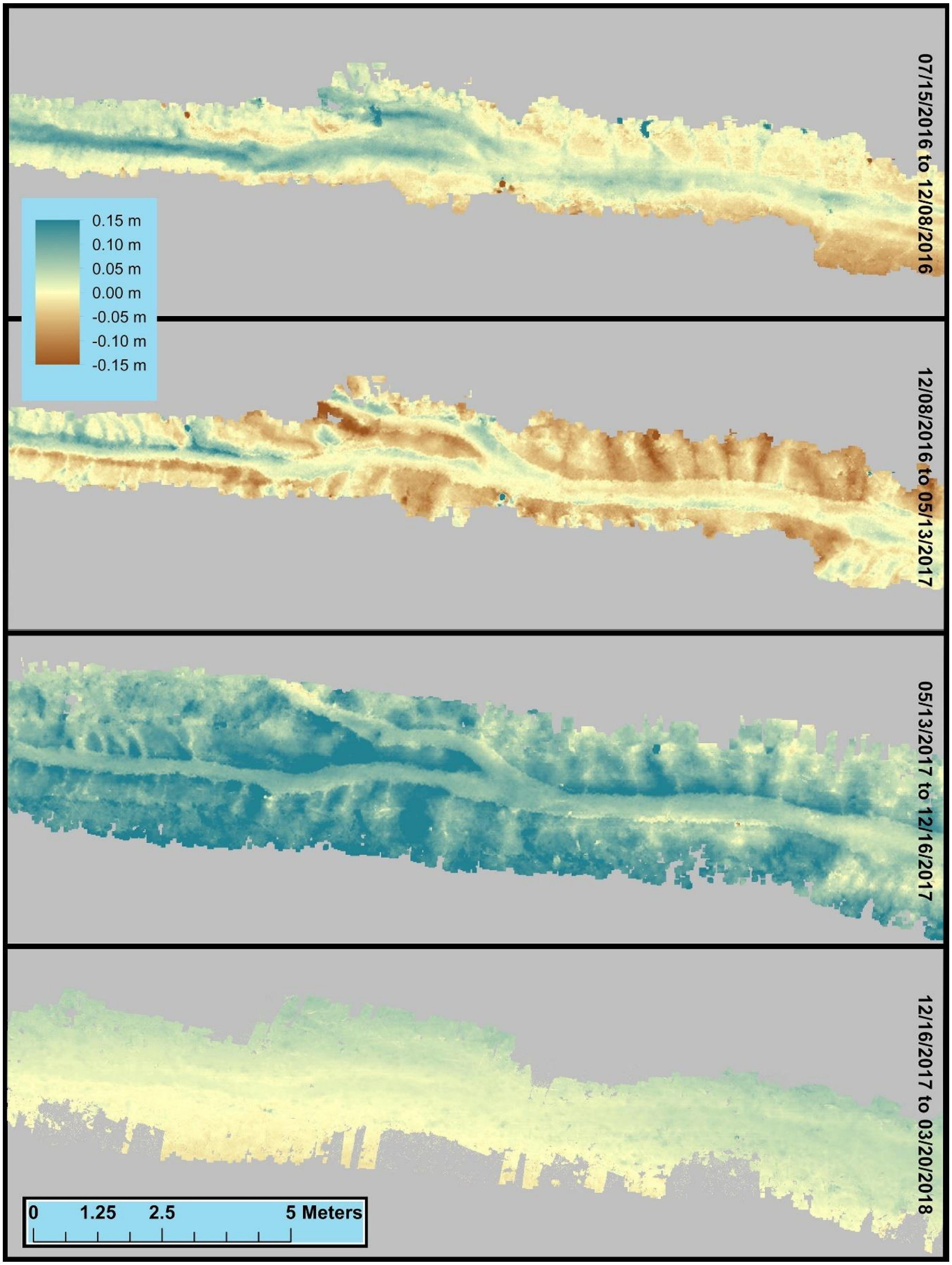

Appendix I – Python Code for Soil Loss Calculation

```
# -*- coding: utf-8 -*-
# ---------------------------------------------------------------------------
# Soil Loss.py
# Created on: 2019-04-04 23:32:21.00000
#   (generated by ArcGIS/ModelBuilder)
# Description:
# ---------------------------------------------------------------------------

# Import arcpy module
import arcpy

# Check out any necessary licenses
arcpy.CheckOutExtension("spatial")



# Local variables:
v05_13_2017_tif = "D:\\Chinthaka\\Project_Pillsbury Crossing\\GUlly
01_Results\\Gully1SoilLoss _Normal\\2017_05_13-2017_07_05\\05_13_2017.tif"
v07_05_2017_tif = "D:\\Chinthaka\\Project_Pillsbury Crossing\\GUlly
01_Results\\Gully1SoilLoss _Normal\\2017_05_13-2017_07_05\\07_05_2017.tif"
v07_05_2017_Boundary_shp = "D:\\Chinthaka\\Project_Pillsbury Crossing\\GUlly
01_Results\\Gully1SoilLoss _Normal\\2017_05_13-
2017_07_05\\07_05_2017_Boundary.shp"
v05_13_2017_Boundary_shp = "D:\\Chinthaka\\Project_Pillsbury Crossing\\GUlly
01_Results\\Gully1SoilLoss _Normal\\2017_05_13-
2017_07_05\\05_13_2017_Boundary.shp"
Intersect__2_ =
"C:\\Users\\cbandara\\Documents\\ArcGIS\\Default2.gdb\\Intersect"
a_tif = "D:\\Chinthaka\\Project_Pillsbury Crossing\\GUlly 01_Results\\New
Folder\\a.tif"
SoilLoss = "D:\\Chinthaka\\Project_Pillsbury Crossing\\GUlly 01_Results\\New
Folder\\soilloss"
Stat = "D:\\Chinthaka\\Project_Pillsbury Crossing\\GUlly
01_Results\\Gully1SoilLoss _Normal\\2017_05_13-2017_07_05\\Stat"
b_tif = "D:\\Chinthaka\\Project_Pillsbury Crossing\\GUlly 01_Results\\New
Folder\\b.tif"
```

```
# Process: Intersect
arcpy.Intersect_analysis("'D:\\Chinthaka\\Project_Pillsbury Crossing\\GUlly
01_Results\\Gully1SoilLoss _Normal\\2017_05_13-
2017_07_05\\07_05_2017_Boundary.shp' #;'D:\\Chinthaka\\Project_Pillsbury
Crossing\\GUlly 01_Results\\Gully1SoilLoss _Normal\\2017_05_13-
2017_07_05\\05_13_2017_Boundary.shp' #", Intersect__2_, "ALL", "", "INPUT")

# Process: Extract by Mask
arcpy.gp.ExtractByMask_sa(v05_13_2017_tif, Intersect__2_, a_tif)

# Process: Extract by Mask (2)
arcpy.gp.ExtractByMask_sa(v07_05_2017_tif, Intersect__2_, b_tif)

# Process: Raster Calculator
arcpy.gp.RasterCalculator_sa("\"%a.tif%\" - \"%b.tif%\"", SoilLoss)

# Process: Zonal Statistics as Table
arcpy.gp.ZonalStatisticsAsTable_sa(Intersect__2_, "OBJECTID", SoilLoss, Stat,
"DATA", "ALL")
```

Appendix J – Matlab Code Used to Calculate Gully Width, Depth, and Cross-sectional Area

```
d = dir([pwd, '\*.csv']);
AllData=[];
Day=[];
NumberOfXS=[];
for numoffiles =1: size(d)
%Initialize variables and open .csv file that has cross sectional elevation
data  1st column=cross-section id, 2nd column=X coordinate, 6th column=Y
coordinate,3rd column= Z coordinate
Path=strcat(pwd,'\',d(numoffiles,1).name);
A = importdata(Path,',',0);
Arranged=[A(:,1) A(:,2) A(:,6) A(:,3)]
B = sortrows(Arranged,[4 2 1]);
NumberOfXS=max(B(:,4));
Boundary=zeros(2*NumberOfXS,5);
FlowLine=[];
XSWidth=zeros(NumberOfXS,2);
LDepth=[];
RDepth=[];
Mean_Depth=[];
WParimiter=[];
Day{numoffiles}=[d(numoffiles,1).name(1:end-4)];
for n=1:NumberOfXS
XS = B(B(:,4)==n&B(:,3)>0, :,:); %select specific cross section and store in
a matrix
minZ=min(XS(:,3));%find the lowest point along the cross section
MINROW=find(XS(:,3)==minZ);
Thalweg=XS(MINROW(1,1),:);
LBank=XS(1,:); %seperate Left bank
RBank=XS(length(XS),:);%seperate Right bank
HigherBankEle=max(LBank(1,3),RBank(1,3));
%Gully width calculation
XSWidth(n,:)=[n sqrt((LBank(1,1)-RBank(1,1))^2+(LBank(1,2)-
RBank(1,2))^2+(LBank(1,3)-RBank(1,3))^2)];
Cal=zeros(length(XS),1);
```

```
Cal(1,1)=[0];
Area=zeros(length(XS),1);
Area(1,1)=0;
% Wetted Parimiter calculation
    for i=2:length(XS)

     Cal(i,1)=Cal(i-1,1)+sqrt((XS(i,1)-XS(i-1,1))^2+(XS(i,2)-XS(i-
1,2))^2+(XS(i,3)-XS(i-1,3))^2);
%Cross-sectional area calculatin
     Area(i,1)=Area(i-1,1)+ sqrt((XS(i,1)-XS(i-1,1))^2+(XS(i,2)-XS(i-
1,2))^2)* (HigherBankEle(1,1)-XS(i,3));
    end

TArea(n,1)=Area(length(XS),1);
WParimiter(n,1)=Cal(length(XS),1);
Area(length(XS),1)];
Boundary(2*n-1,:)=[LBank 0];
Boundary(2*n,:)=[RBank 1];
FlowLine(n,:)=XS(MINROW(1,1),:);
LDepth(n,:)=LBank(1,3)-XS(MINROW(1,1),3);
RDepth(n,:)=RBank(1,3)-XS(MINROW(1,1),3);
Mean_Depth(n,:)=(LBank(1,3)+RBank(1,3))/2-XS(MINROW(1,1),3);
%filling all data into 3d array 1=width,2=area,3=depth by l bank, 4,depth by
R bank, 5=median depth, 6=width by median depth,7=depth by width
AllData(numoffiles,n,1)=XSWidth(n,2);
AllData(numoffiles,n,2)=Area(length(XS),1);
AllData(numoffiles,n,3)=LDepth(n,1);
AllData(numoffiles,n,4)=RDepth(n,1);
AllData(numoffiles,n,5)=Mean_Depth(n,1);
AllData(numoffiles,n,6)=Area(length(XS),1)/Mean_Depth(n,1);
AllData(numoffiles,n,7)=Area(length(XS),1)/XSWidth(n,2);

end
end

for k=1:NumberOfXS
t=table(Day',[AllData(:,k,1)],AllData(:,k,2),[AllData(:,k,3)],[AllData(:,k,4)
],[AllData(:,k,5)],[AllData(:,k,6)],[AllData(:,k,7)]);
```

```
t.Properties.VariableNames={'Date' 'Width' 'Area' 'L_Depth' 'R_Depth'
'Median_Depth' 'Width_by_Depth'  'Depth_by_Width'};
writetable(t,strcat(pwd,'\CrossSection_',num2str(k),'.csv'),'Delimiter',',')
;
type CrossSection_1.csv;
fileID1 = fopen(strcat(pwd,'\CrossSection_',num2str(k),'.txt'),'w');
fprintf(fileID1,'%1$s %2$s %3$s %4$s %5$s %6$s %7$s
%8$s\r\n','Date','Width','Area','L_Depth','R_Depth','Median_Depth','Width by
Depth', 'Depth by Width');
for m=1:numoffiles
end
fclose(fileID1);
end
```